I. PREDICTING EQUILIBRIUM STABLE ISOTOPE FRACTIONATIONS OF IRON,

CHLORINE, AND CHROMIUM

II. OXYGEN-ISOTOPE INVESTIGATION OF MESOZOIC AND CENOZOIC

GRANITOIDS OF THE NORTHEASTERN GREAT BASIN, NEVADA AND UTAH

Thesis by

Edwin Arthur Schauble

In Partial Fulfillment of the Requirements

for the Degree of

Doctor of Philosophy

California Institute of Technology

Pasadena, California

2002

(Defended May 23, 2002)

Acknowledgments

I want to thank Hugh Taylor for serving as my research advisor, and for consistently supporting work on such a diverse range of projects. And George Rossman, for keeping the door open and being interested in new, sometimes half-baked ideas. Thanks to Caltech and the NSF (through grants grant nos. EAR-9725811 to EAS and HPT, and EAR-9804871 to GRR) for providing the resources to make this research possible. I want to thank Liz Johnson, for inspiring much of this thesis and for making everything else better, I owe you as much gratitude as anyone.

John Eiler, Crayton Yapp, Ariel Anbar, and Robert Housley gave the encouragement and timely advice needed to turn the initial theoretical excursions on iron-isotope and oxygen-isotope fractionations into something more. Thanks also to Tahir Cagin and Bill Goddard for providing my first indroduction to computational chemistry, to Joe Kirschvink for opening up the world of iron-isotope geochemistry (and for field trips to Baja, Morocco, and South Africa), and to Lee Riciputi for hinting at the need for a closer theoretical look at many stable isotope systems. Clark Johnson, Brian Beard, Tom Johnson, Tom Bullen, Alan Matthews, and others deserve much credit for making the measurements that put this work to use. Jim O'Donnell and Susan Leising helped me make the most of Caltech's libraries. This research has also benefited from free software written by Julian Gale, Xavier Gonze, Brett Bode and the Gordon research group at Iowa State University.

I am grateful to Jim Wright for providing samples from the Great Basin, and for freely sharing his published and unpublished Nd-, Sr-, and Pb-isotope results, and to Nami Kitchen for performing some oxygen-isotope analyses on mineral separates.

Abstract

Theoretical studies of the stable isotope geochemistry of iron, chlorine, and chromium are presented, with the goal of providing a framework to aid interpretations of new measurements and to identify promising areas for future study. In addition, new oxygen-isotope measurements of Mesozoic and Cenozoic granitoids from the northeastern Great Basin are used to constrain the temporal evolution of magmatic sources in the region.

The stable isotope compositions of elements heavier than sulfur (atomic no. 16) are generating great geochemical interest, now that new mass-spectrometry techniques make it possible to measure their isotopic abundances with high precision. Theoretical calculations for three of these elements (iron, chlorine, and chromium) are made using published infrared, Raman, and inelastic neutron scattering measurements of vibrational frequencies, in combination with empirical and *ab initio* force-field estimates of unknown frequencies. The calculations suggest that a number of natural processes can drive significant stable isotope fractionations of heavy elements, including oxidation/reduction during the precipitation or dissolution of dissolved metals (inorganically or organically), and bond-partner exchange during hydrothermal alteration, or degradation of Cl-bearing organic compounds. At equilibrium and 25°C, $^{56}Fe/^{54}Fe$ will be ~5‰ higher in $[Fe(H_2O)_6]^{3+}$ than in coexisting $[Fe(H_2O)_6]^{2+}$, $^{53}Cr/^{52}Cr$ will be ~6-7‰ higher in $[CrO_4]^{2-}$ than in coexisting $[Cr(H_2O)_6]^{3+}$ or Cr_2O_3, and aqueous Cl^- will be ~2-3‰ lighter than coexisting alteration minerals like mica and amphibole.

Oxygen isotope measurements of whole-rock samples from granitoid plutons in the northeastern Great Basin suggest that two or three different types of source rocks

were melted in varying proportions during the three stages of magmatism in this region in the Late Jurassic, Late Cretaceous, and mid-Cenozoic. Radiogenic-isotope measurements were previously made on the same samples. Late Cretaceous (90-70 Ma) granites have high $\delta^{18}O$ (+9.3 to + 12.1) and $^{87}Sr/^{86}Sr_i$ (0.711 to 0.734), and low εNd (-13 to -23) indicating that their source was dominated by evolved crustal sediments and basement. However, late Jurassic plutons in this region span a larger range of $\delta^{18}O$ values (+7.2 to +13.2), despite having Sr and Nd isotopic compositions that are much less suggestive of an ancient crustal component ($^{87}Sr/^{86}Sr_i$ = 0.705 to 0.711, εNd = -2.5 to -6.5) than the Late Cretaceous plutons, suggesting moderate to extensive mixing or assimilation of high-$\delta^{18}O$ sedimentary rocks into a more mafic parent melt. The 40-25 Ma Cenozoic plutons ($\delta^{18}O$ = +7.0 to +9.7, $^{87}Sr/^{86}Sr_i$ = 0.707 to 0.717, εNd = -13.2 to -26.3) probably have a source dominated by continental basement. The Cenozoic plutons can be subdivided into a higher $\delta^{18}O$ (+8.6 to +9.7) southern group and a lower $\delta^{18}O$ (+7.0 to +8.2) northern group across a Crustal Age Boundary (CAB) at roughly 40° 40' N; this CAB coincides with a radiogenic isotope boundary defined with the same samples, as well as with the approximate southern limit of exposure of Archean basement. The low $\delta^{18}O$ values and depleted lead isotope compositions of the Lower Array (northern) samples indicate that Archean age basement is present beneath a large area of the most northeasterly part of the Great Basin. A further, speculative conclusion is that $\delta^{18}O$ of the (meta)sedimentary source region may have dropped by 2-3‰ as a result of fluid-rock interaction sometime between the Jurassic and Late Cretaceous magmatic episodes.

Table of Contents

List of Figures

Chapter 2

Chapter 3

Chapter 4

Chapter 5

List of Tables

Chapter 2

Chapter 3

Chapter 1. Introduction

This thesis encompasses four stable isotope studies, each concentrating on a different element. It divides naturally into two parts, the first (including Chapters 2–4) includes comprehensive theoretical studies of the stable isotope geochemistry of iron, chlorine, and chromium. These studies are the first to look at geochemically relevant aqueous iron and chromium species, chromium- and chlorine-bearing crystals, and Chapter 3 also greatly expands the number of theoretically studied chlorine-bearing molecules and gas-phase species. The second part (Chapter 5) applies oxygen-isotope measurements to the problem of unraveling changing magmatic sources in the Great Basin over time. Each chapter is derived from a separate manuscript, and can more or less stand alone.

1.1. Introduction to part 1

Chapters 2-4 present theoretical studies of equilibrium stable isotope fractionations for the elements iron, chlorine, and chromium. The goal of these chapters is to create a basic theoretical framework to figure out how transition element and halogen-element stable isotope measurements might improve our understanding of processes like alteration of oceanic crust, the formation of reactive gases from marine aerosols, biological processing of metals, and the remediation of groundwater pollution. This work is motivated chiefly by the recent discovery of transition element (Cr, Fe, Cu, Zn, Mo, etc.) isotope abundance variations in natural terrestrial samples. These discoveries were made possible by the introduction of multi-collector, inductively coupled mass-spectrometer technology (MC-ICP-MS), and the application of double-

spike thermal ionization mass-spectrometry (double-spike TIMS), which have greatly

improved the speed, precision, and accuracy of stable isotope measurements for elements

that cannot be analyzed conveniently in the gas phase. However, we do not know much

about how natural processes cause isotopic fractionation for these elements. In fact, a

basic theoretical understanding of the factors controlling isotopic fractionation has been

lacking for elements that have been studied for much longer, including lithium, silicon,

and chlorine. This work has benefited from advice given by George Rossman, who is a

co-author on the manuscripts that form the bulk of these three chapters. Chapter 2 (iron-

isotopes) has previously been published (SCHAUBLE et al., 2001).

1.1.1. Theory of Equilibrium Stable Isotope Fractionation

Equilibrium stable isotope fractionation is a quantum-mechanical effect, mainly

caused by differences in the vibrational zero-point energies (ZPE) of isotopically

substituted materials. The effect is quantified using the ratio of partition functions for

isotopically light and heavy forms of the substance of interest. For a (nonlinear)

polyatomic molecule, a simplified form of this ratio was expressed by UREY (1947) in the

following form:

$$\frac{Q_2}{Q_1} = \frac{\sigma_1}{\sigma_2} \prod_{i=1}^{3N-6} \frac{U_{2i}}{U_{1i}} \left(\frac{\exp(-U_{2i}/2)}{1 - \exp(-U_{2i})} \right) \left(\frac{1 - \exp(-U_{1i})}{\exp(-U_{1i}/2)} \right)$$

where subscripts 1 and 2 indicate isotopically light and heavy forms of a molecule, σ_1

and σ_2 are symmetry numbers for the two isotopic forms, and N is the number of atoms

in the molecule (a nonlinear molecule has 3N-6 vibrational modes, a linear molecule has

one additional mode, in that case the product will have 3N–5 terms). The quantity U_{ni}

equals $(h\nu_{ni}/kT)$, where ν_{ni} is the vibrational frequency of mode *i*, *h* is Planck's constant, *k*

is Boltzmann's constant, and T is the temperature (in Kelvin). If we know the partition

function ratios for two substances (A and B), we can calculate the stable isotope

fractionation between them using a variation of Criss' (1991) formulation:

$$\ln \alpha_{A-B} = \frac{1}{a} \ln \left[\frac{\sigma_2 Q_2}{\sigma_1 Q_1} \right]_A - \frac{1}{b} \ln \left[\frac{\sigma_2 Q_2}{\sigma_1 Q_1} \right]_B$$

where $\alpha_{A-B} = R_A/R_B$, the ratio of heavy to light isotopes (i.e., $^{37}Cl/^{35}Cl$) in molecule A

divided by the ratio of heavy to light isotopes in molecule B, and a and b are the number

of atoms of the isotopically substituted element in molecules B and A, respectively. By

comparing the two equations it is clear that all symmetry numbers cancel out, and so do

not affect equilibrium isotope fractionation. A convenient way to tabulate fractionations

is in terms of beta-factors:

$$\ln \beta_{[A]} = \frac{1}{a} \ln \left[\frac{\sigma_2 Q_2}{\sigma_1 Q_1} \right]_A$$

With this equation, isotopic fractionation between any two substances can be calculated as

the difference between their respective beta-factors (Richet et al., 1977). If both sides of

the equation are multiplied by 1000, then the beta factors, in per mil units, are easily

converted to the δ-notation commonly used to express measured stable isotope

fractionations (see section 1.3). This is because $1000 \cdot \ln(\beta[X]) - 1000 \cdot \ln(\beta[Y]) \approx \delta_X - \delta_Y$

at equilibrium.

The Urey (1947) formula for calculated partition function ratios makes a number

of assumptions. 1. Molecular rotation and translation are assumed to behave classically,

thus having no effect of isotope fractionation. This assumption breaks down at very low

temperatures (depending on the moments of inertia of the molecule), where rotational

quanta become important. 2. Molecular vibrations are assumed to be harmonic. Anharmonicity probably does have a second order effect on isotope fractionations between molecules, as well as dissolved species and solids, but data are rarely available to calculate these effects on species with more than 2–3 atoms. 3. Isotope substitution is assumed to have no effect on the electronic structure of molecules (i.e., the Born-Oppenheimer approximation). For molecules containing more than one atom of the substituted element, the formulas for α and β further assume a random distribution of singly and multiply substituted isotopic species. This assumption is clearly inadequate for some elements (particularly hydrogen), in which the heavy isotopes tend to group together in the same molecule (RICHET et al., 1977). It is expected to work well for heavy elements, however, where the relative range of isotopic masses is smaller. We have tested this assumption on a few chlorine-bearing molecules, and found that associated errors (< 0.1‰) are small relative to other sources of uncertainty. To be safe, we have modified the equations slightly, so that molecular partition function ratios are calculated assuming that only one atom of the rare isotope is substituted. Mineral and crystal partition function ratios are calculated assuming complete substitution, however. 4. All of the vibrational frequencies for both isotopic forms of the molecules of interest are known. In fact, this is rarely the case, and the major technical hurdle addressed in this thesis is finding ways to estimate unknown frequencies.

1.1.2. Chemical Controls on Stable Isotope Fractionation

Light-element stable isotope fractionations are often qualitatively explicable in terms of chemical systematics such as relative bond strengths, changing oxidation states, and bond-partner exchange. We have found through theoretical calculations that heavier

elements (at least up to iron) show similar systematic behavior. BIGELEISEN and MEYER (1947) showed that at sufficiently high temperatures beta-factors can be approximated by a function proportional to $1/T^2$, while Criss (1991) has shown that they become linear in $1/T$ at lower temperatures. The transition between these two regimes depends on the vibrational frequencies of the molecule of interest. O'NEIL (1986) suggests that $1/T^2$ proportionality will hold when $T > 0.2(h\nu_{ni}/k)$, while linearity in $1/T$ will be approached when $T < 0.05(h\nu_{ni}/k)$. With the exception of hydrogen, and atoms directly bonded to hydrogen, most polyatomic molecules have vibrational frequencies low enough to put them in the $1/T^2$ regime at temperatures above 25°C. The marked temperature sensitivity of equilibrium stable isotope fractionation forms the basis of most stable isotope geothermometers, and this property is important in the present work because it suggests that transition element isotope fractionations will be largest at low temperatures — in agreement with observations.

BIGELEISEN and MAYER (1947) further showed that (in the $1/T^2$ regime) the tendency of a molecule to concentrate heavy isotopes of an atom is proportional to the stiffness of that atom's bonds in the molecule (i.e., the sum of the force-constants acting on the atom). HOUSLEY and HESS (1966) showed that minerals will show the same force-constant dependence. More recently O'NEIL (1986) has elaborated on the geochemical significance of this systematic behavior, which suggests that substances with strong, highly covalent bonds, high oxidation-state sites (for the element of interest) and small, highly charged bond partners will tend to concentrate the heavy isotopes of an element. In all three elements studied we have found a strong correlation between calculated beta-factors and the oxidation state of that element, the bond-partner oxidation state, and/or

the presence of strong, covalent bonds (as indicated by *d*-orbital splitting in iron and chromium). In addition, we found tentative evidence that coordination number has a significant effect, at least for iron, which is in agreement with previously observed coordination number effects on the fractionation of boron and carbon isotopes.

These systematics suggest that heavy-element stable isotope measurements are best suited to study natural reduction/oxidation and bond-partner-exchange processes occurring at relatively low temperatures. One example of such a process is the remediation of groundwater pollution, including $[CrO_4]^{2-}$ and various chlorine-bearing organic substances like trichloroethylene (C_2HCl_3). Chromate $[CrO_4]^{2-}$, containing Cr^{6+}, is rendered harmless via reduction to insoluble Cr^{3+}-bearing species, while aqueous chlorine-bearing organics are usually destroyed via reactions in which the chlorine goes into solution (and is bonded weakly to H_2O). Both of these processes involve large calculated fractionations, and this may be the dominant cause of chromium-isotope fractionation at the earth's surface. There is every reason to believe that other elements (including molybdenum and the platinum-group elements) may be similarly fractionated during reduction/oxidation reactions during weathering and transport into the oceans, and ultimately during fixation into various sinks. For many transition elements, exchange of oxygen (or hydroxyl or water) bond-partners for sulfur or biological ligands is also likely to be important. Already, BARLING et al. (2001) has observed that dissolved molybdenum in the oceans is fractionated with respect to oxidized sediments but very similar to reduced sediments, and used the compositions of the oceanic sediments (and representative continental samples) to constrain the relative fluxes of molybdenum to oxidizing and reducing sinks.

1.2. Introduction to part 2.

The second part of the thesis (chapter 5) is an oxygen-isotope study of granites and related plutonic rocks that crystallized between 170 and 25 million years ago in the northeastern Great Basin, which includes parts of northwestern Utah and northeastern Nevada. The goal of this work is to identify the source rocks that melted to form the granites, and to understand why different source rocks seem to have melted at different times. In this work, oxygen isotopes are used primarily as a tracer, showing the relative contributions from rocks formed at the earth's surface (particularly sediments and altered volcanic rocks) and rocks derived from the earth's mantle. Jim Wright collaborated on this work, having previously measured the radiogenic isotope (Sr, Nd, and Pb) compositions of these samples, and is a coauthor on the manuscript that Chapter 5 is based on.

1.3. δ-notation

Isotope ratios are reported in δ-notation,

$$\delta = \left(\frac{R_{sample} - R_{standard}}{R_{Standard}}\right) \times 1000$$

where R_{sample} is the isotope ratio in a sample and $R_{stabdard}$ is the isotope ratio in a standard. Mean Ocean Water (SMOW) and seawater dissolved chloride are accepted standards for reporting $^{18}O/^{16}O$ and $^{37}Cl/^{35}Cl$, respectively. Iron and chromium do not have universally accepted standards yet, each laboratory reports measurements relative to a different standard material. Some labs (i.e., ZHU et al., 2000) report stable isotope compositions for transition metals in ε-notation, which is exactly analogous to δ-notation, except that the factor of 1000 is increased to 10,000.

1.4. Bibliography

Barling J., Arnold G. L., and Anbar A. D. (2001) Natural mass-dependent variations in the isotopic composition of molybdenum. *EPSL* **193**(3-4), 447-457.

Bigeleisen J. and Mayer M. G. (1947) Calculation of equilibrium constants for isotopic exchange reactions. *J. Chem. Phys.* **15**, 261-267.

Criss R. E. (1991) Temperature dependence of isotopic fractionation factors. In *Stable isostope geochemistry: a tribute to Samuel Epstein, Geochemical Society, Special Publication No. 3* (ed. H. P. J. Taylor, J. R. O'Neil, and J. R. Kaplan).

Housley R. M. and Hess F. (1966) Analysis of Debye-Waller-factor and Mössbauer-thermal-shift measurements. 1. General theory. *Physical Review* **146**(2), 517-526.

O'Neil J. R. (1986) Theoretical and experimental aspects of isotopic fractionation. In *Stable isotopes in high temperature geological processes, Reviews in Mineralogy*, Vol. 16 (ed. J. W. Valley, H. P. Taylor, Jr., and J. R. O'Neil), pp. 1-40. Mineralogical Society of America.

Richet P., Bottinga Y., and Javoy M. (1977) A review of hydrogen, carbon, nitrogen, oxygen, sulphur, and chlorine stable isotope fractionation among gaseous molecules. *Ann. Rev. Earth Planet. Sci.* **5**, 65-110.

Schauble E. A., Rossman G. R., and Taylor H. P., Jr. (2001) Theoretical estimates of equilibrium Fe-isotope fractionations from vibrational spectroscopy. *Geochimica et Cosmochimica Acta* **65**, 2487-2497.

Urey H. C. (1947) The thermodynamic properties of isotopic substances. *J. Chem. Soc.*, 562-581.

Zhu X.-K., O'Nions R. K., Guo Y., and Reynolds B. C. (2000) Secular variation of iron isotopes in North Atlantic Deep Water. *Science* **287**, 2000-2002.

Chapter 2. Theoretical estimates of equilibrium Fe–isotope fractionations from vibrational spectroscopy

The magnitude and direction of equilibrium iron-isotope (^{54}Fe - ^{56}Fe) fractionations among simple iron-bearing complexes and α-Fe metal are calculated using a combination of force-field modeling and existing infrared, Raman, and inelastic neutron scattering measurements of vibrational frequencies. Fractionations of up to several per mil are predicted between complexes in which iron is bonded to different ligands (i.e., 4 per mil for $[Fe(H_2O)_6]^{3+}$ vs. $[FeCl_4]^-$ at 25°C). Similar fractionations are predicted between the different oxidation states of iron. The heavy iron isotopes will be concentrated in complexes with high-frequency metal-ligand stretching vibrations, which means that ^{56}Fe/^{54}Fe will be higher in complexes with strongly bonding ligands such as CN$^-$ and H_2O relative to complexes with weakly bonding ligands like Cl$^-$ and Br$^-$. ^{56}Fe/^{54}Fe will also usually be higher in Fe(III) compounds than in Fe(II)-bearing species; the Fe(II) and Fe(III) hexacyano complexes are exceptions to this rule of thumb. Heavy iron isotopes will be concentrated in sites of 4-fold coordination relative to 6-fold coordination. Model results for a ferrous hexacyanide complex, $[Fe(CN)_6]^{4-}$, are in agreement with predictions based on Mössbauer spectra POLYAKOV (1997), suggesting that both approaches give reasonable estimates of iron-isotope partitioning behavior.

2.1. Introduction

The purpose of this study is to estimate equilibrium iron-isotope fractionations, in order to complement and better comprehend the expanding body of measurements of iron-isotope abundance variations in natural samples. Because so little previous work has

been done in predicting equilibrium partitioning of transition metal isotopes, a wide spectrum of simple chemical species is investigated, including several geochemically important species. A firm understanding of equilibrium isotopic fractionations is the essential first step to understanding the geochemical and biogeochemical processes affecting any stable isotope system.

Recent developments in instrumentation and new measurement techniques have led to renewed interest in possible geochemical variability of transition metal isotope abundances (ANBAR et al., 2000; BEARD and JOHNSON, 1999; BEARD et al., 1999; ZHU et al., 2000). Iron, with four stable isotopes (mass #'s 54, 56, 57, and 58), is particularly interesting because of its rich geochemical variability and important role in biochemistry.

There are several reasons to expect measurable inorganic iron-isotope fractionations in nature, particularly in low temperature environments. Iron commonly occurs in nature as divalent and trivalent (i.e., Fe(II) and Fe(III)) compounds, which have distinct geochemistries and bonding strengths. Iron has a variety of geochemically important bonding partners and ligands, forming ubiquitous sulfide, oxide, and silicate minerals as well as complexes with water and biological molecules. Oxidation-reduction, precipitation, and complexation of iron all occur at relatively low temperatures and in the presence of aqueous solutions. Chemical equilibration can occur relatively quickly in aqueous solutions, and equilibrium isotopic fractionations are greatest at low temperature and between chemically different species. These observations suggest that measurable geochemical fractionation of the iron isotopes arising from equilibrium processes may occur in addition to possible non-equilibrium biological effects.

POLYAKOV (1997), and POLYAKOV and MINEEV (2000) made the first attempts to predict equilibrium iron-isotope fractionations, using ^{57}Fe-Mössbauer spectra. One important goal of the present study is to test the accuracy of these Mössbauer-based predictions by comparing them to our results, which use an independent type of data (vibrational spectra) and a distinctly different model. Cross-checking the Mössbauer- and vibrational-spectra-based calculations is also an important preliminary step in evaluating the potential of vibrational modeling to accurately predict equilibrium isotope fractionations in metal-isotope systems that cannot be studied by Mössbauer spectroscopy.

Equilibrium stable isotope fractionations for the light elements H, B, C, N, O, S, and Cl can be accurately modeled in terms of the small energy differences arising from the sensitivity of the vibrational frequencies of substances to the masses of their constituent atoms (RICHET et al., 1977; UREY, 1947). The substitution of a heavy isotope into a substance reduces its vibrational frequencies, leading to a small decrease in vibrational energy; the energy decrease varies from one substance to another. This variability means that there is a nonzero energy associated with isotopic exchange between different substances, which leads to unequal partitioning of isotopes when two or more substances containing an element are at equilibrium. Isotope partitioning can be expressed in terms of a beta-factor (i.e., β_{56-54} for ^{56}Fe-^{54}Fe exchange), defined as the ratio at equilibrium of the isotope ratio of the substance of interest to the isotope ratio of dissociated atoms. Beta is equivalent to $(s/s')f$ as defined by BIGELEISEN and MAYER (1947). We will follow the example of earlier work (KIEFFER, 1982; POLYAKOV, 1997) by reporting reduced partition function ratios (i.e., $1000 \cdot \ln\beta$). The difference between the

calculated reduced partition function ratios of two substances is approximately equal to the predicted equilibrium isotopic fractionation between them; one unit of $1000 \cdot \ln\beta \approx 1$ per mil or 10 ε-units. It is expected that $1000 \cdot \ln\beta_{57-54}$ for a substance will be ~1.5 times as large as $1000 \cdot \ln\beta_{56-54}$. A 1 per mil difference in $^{56}Fe/^{54}Fe$ is therefore roughly equivalent to a 15 ε difference in $^{57}Fe/^{54}Fe$.

2.2. Methods

Reduced partition function ratios are calculated using the approach of UREY (1947) and BIGELEISEN and MAYER (1947, eqn. 10). In the calculations, no corrections for vibrational anharmonicity are made. There is generally not enough spectroscopic information available to quantitatively estimate anharmonic parameters, but it is nonetheless probable that the errors associated with this assumption are small compared to other likely sources of error (BIGELEISEN and MAYER, 1947). Measured vibrational frequencies for each molecule and complex studied have been compiled from the literature. In many cases the spectral measurements were made on weakly bonded salts or molecular crystals. In general, lattice effects and vibrations (for salts), or solvent interactions (for solutions) are ignored, and calculations are made using only the skeletal frequencies associated with each complex. Whenever enough published data are available, vibrational frequencies from different salts or solutions are compared to quantify errors resulting from this simplified treatment.

For all of the complexes and substances studied, spectroscopic measurements have been made only on samples containing the naturally occurring mix of the stable iron isotopes, which is dominated by ^{56}Fe (92 atom %). It is therefore necessary to adopt a scheme for estimating the vibrational frequencies of isotopically pure compounds. In the

14

present work, this is accomplished by the following procedure. Observed vibrational

frequencies are assumed to be equivalent to the spectrum of a pure ^{56}Fe-bearing

compound. The ratios of the vibrational frequencies in ^{54}Fe-substituted and ^{56}Fe-

substituted compounds are calculated, and the vibrational spectrum of the ^{54}Fe-

substituted compound is obtained by multiplying the calculated frequency ratios by the

observed vibrational frequencies. An analogous procedure is used to calculate vibrational

frequencies for ^{57}Fe-substituted $[Fe^{II}(CN)_6]^{4-}$ and α-Fe metal, so that $1000 \cdot \beta_{57-54}$ can be

calculated for comparison with the results of POLYAKOV (1997).

In some substances (such as metallic iron), calculating the vibrational frequencies of

the ^{54}Fe-substituted compound is straightforward. In tetrahedral (FeX$_4$) and octahedral

(FeX$_6$) complexes, however, the motion of the central iron atom is unevenly apportioned

among two triply degenerate vibrational modes (v_3 and v_4), and the sensitivity of the

vibrational frequencies of these modes to isotopic substitution cannot be calculated from

geometric constraints alone. For these and larger complexes, it is necessary to use a

force-field model to calculate the vibrational frequencies of ^{54}Fe-substituted complexes.

The Modified Urey-Bradley Force Field (NAKAMOTO, 1997; SIMANOUTI (SHIMANOUCHI),

1949), hereafter abbreviated MUBFF, was chosen for this purpose because it has a small

number of parameters (three for tetrahedral and octahedral complexes) and does a good

job of predicting the effects of isotopic substitution on vibrational frequencies in

tetrahedral and octahedral complexes (Table 2.1). Observed vibrational frequencies and

calculated isotopic frequency shifts used in calculating reduced partition function ratios

are listed in Tables 2.2 and 2.3. A more detailed description of the methods applied to

each of the studied compounds may be found in Appendix 1. The accuracy of this general

method of estimating equilibrium stable isotope fractionations has already been demonstrated for lighter elements (e.g., RICHET et al. 1977).

2.3. Results

2.3.1. Calculated Fractionations

Calculated reduced partition function ratios for ^{56}Fe - ^{54}Fe exchange at temperatures from 0°C to 300°C are shown in Table 2.4 and plotted in Fig. 2.1. Reduced partition function ratios calculated for ^{57}Fe - ^{54}Fe exchange in α-Fe metal and $[Fe^{II}(CN)_6]^{4-}$ are plotted in Fig. 2.2 for comparison with the predictions of POLYAKOV (1997). As expected, reduced partition function ratios increase with decreasing temperature, and are approximately proportional to $1/T^2$ for all temperatures considered. For ^{56}Fe - ^{54}Fe exchange, values of $1000 \cdot \ln(\beta_{56-54})$ at 298 K range from about 17.6 per mil for $[Fe^{II}(CN)_6]^{4-}$ to 3.8 per mil for $[Fe^{III}Cl_6]^{3-}$; analogous $1000 \cdot \ln(\beta_{57-54})$ values are almost exactly 1.5 times as large.

Equilibrium ^{57}Fe - ^{54}Fe fractionations calculated from Raman and infrared vibrational spectra and force-field modeling compare very well with the Mössbauer spectroscopy-based predictions of POLYAKOV (1997). Polyakov reports two reduced partition function ratios for compounds containing a $[Fe^{II}(CN)_6]^{4-}$ substructure, which bracket the reduced partition function ratio calculated in the present study. Values of $1000 \cdot \ln(\beta_{57-54})$ for $K_4Fe(CN)_6 \cdot 3H_2O$ and $K_4Fe(CN)_6$ reported by POLYAKOV (1997) are about 10% larger and 0.5% smaller, respectively, than our calculations predict. Since the vibrational spectra used in our model are from $K_4Fe(CN)_6 \cdot 3H_2O$, the upper curve of Polyakov is the most direct comparison. The Mössbauer and IR/Raman spectroscopy data

for potassium ferrocyanide are independent, so the qualitative agreement between both

approaches to estimating partition function ratios is evidence that the results are sound.

The 10% mismatch, equivalent to about 2.6 per mil at 298 K, is consistent with the

magnitude of errors arising from the calculation of the vibrational frequencies of

$[^{54}Fe^{II}(CN)_6]^{4-}$ (see Appendix 1). The reduced partition function ratios for metallic iron

are coincident within 0.3 per mil at 298 K. This particular comparison is not as useful,

however, as the Mössbauer results in HOUSLEY and HESS (1967), used as input into

Polyakov's calculations, were calculated from inelastic neutron scattering data (BERGSMA

et al., 1967) for lattice vibrations in α-Fe.

2.3.2. Accuracy Estimates

Indirect estimates of the accuracy of the calculated reduced partition function ratios

for the other species are obtained by examining the fidelity of the MUBFF in predicting

isotopic shifts in vibrational species, and by comparing partition function ratios

calculated for a given species using different spectral data.

In Table 2.1, it is clear that the MUBFF does a fairly good job of estimating isotopic

shifts in tetrahedral and octahedral complexes and molecules. Observed and calculated

ratios of vibrational frequencies in isotopically substituted and unsubstituted tetrahedral

molecules and complexes typically agree within ~0.0005. For octahedral complexes the

measured spectra of isotopically substituted complexes are typically not as precise, so it

is hard to judge the accuracy of the force field at an equivalent level. Data for SF_6

(BRUNET and PEREZ, 1969) do suggest that the model can be accurate to about 0.0005 for

simple octahedral complexes. Aquo complexes, with isotopic shifts calculated using the

point mass approximation, are probably not modeled as accurately. Errors of ~0.0005 in

$^{56}v/^{54}v$ propagate into errors equivalent to about 0.4 per mil for $[Fe^{III}Cl_4]^-$, 0.2 per mil for $[Fe^{III}Br_4]^-$ and $[Fe^{II}Cl_4]^{2-}$, and 0.1 per mil for $[Fe^{III}Cl_6]^{3-}$ at 298 K. Larger uncertainties of ~0.001 in $^{56}v_3/^{54}v_3$ for $[Fe^{III}(H_2O)_6]^{3+}$ and $[Fe^{II}(H_2O)_6]^{2+}$ propagate to errors of approximately 0.8 per mil and 0.6 per mil in their respective reduced partition function ratios at 298 K.

The second method for estimating the accuracy of the calculated partition function ratios compares calculations made using different spectral input data. Spectroscopy of many of the complexes of interest was carried out on salts with molecular ions rather than on species in solution. The problem is particularly acute for IR-active modes because water is a strong infrared absorber, making measurement of vibrational bands of solute species either difficult or impossible. Vibrational frequencies of salts where the complexes form substructures in the lattice are often easier to measure, but there is the possibility that the frequencies are distorted by interactions with other constituents of the salt. Spectroscopists typically minimize this problem by studying salts with weakly bonding counter-ions such as Cs^+, Rb^+, and $[ClO_4]^-$, and such data are useful when measurements of solute species are unavailable or incomplete.

The well-studied $[Fe^{III}Cl_4]^-$ complex is a good test case for examining the effects of lattice perturbations on calculated isotopic partition function ratios. Vibrational frequencies of the $[Fe^{III}Cl_4]^-$ complex have been measured in a weakly bonded (Et$_4$N)FeCl$_4$ salt, in nitromethane solution (AVERY et al., 1968), and in acidic aqueous solutions with and without high Li$^+$ concentrations (MURATA and IRISH, 1988). The frequencies of the v_3 (asymmetric stretch) mode observed in these four chemical environments vary from 378 cm^{-1} in the salt to 395 cm^{-1} in high-Li$^+$ solution, a range of

about 5%. These variations may also arise partly from uncertainties in measurement. Perturbations to the calculated partition function ratios caused by lattice effects and differing solution environments are estimated by using each set of reported frequencies to create a force-field model, then using the frequencies and predicted isotopic shifts to calculate isotopic partition function ratios. Values of $1000 \cdot \ln(\beta_{56-54})$ calculated for $[Fe^{III}Cl_4]^-$ in this way vary from 7.1 to 7.7 per mil at 298 K. Fig. 2.1 and Table 2.4 are calculated using the Li^+-free aqueous solution spectrum of Murata and Irish ($v_3 = 384$ cm^{-1}), because it is the best analogue for likely laboratory and geochemical conditions. The Li^+-free aqueous solution spectrum leads to a calculated value of $1000 \cdot \ln(\beta_{56-54}) =$ 7.2 at 298 K.

Similar variations in measured vibrational frequencies in different salts and/or solution are apparent for other well-studied complexes, such as $[Fe^{III}Br_4]^-$, $[Fe^{III}Cl_6]^{3-}$, $[Fe^{III}(H_2O)_6]^{3+}$, $[Fe^{II}(CN)_6]^{4-}$, and $[Fe^{III}(CN)_6]^{3-}$. In the case of $[Fe^{III}Br_4]^-$, vibrational frequencies measured in a series of salts with the general formula $AFeBr_4$ (A = Li, Na, K, Rb, Cs, Et$_4$N) (AVERY et al., 1968; THIELE et al., 1992) lead to values of $1000 \cdot \ln(\beta_{56-54})$ ranging from 5.7 to 6.7 at 298 K. As expected, the salts with the most weakly bonding cations, K^+, Rb^+, Cs^+, and $(Et_4N)^+$ give a more restricted range of values, from 6.0 to 6.5.

The uncertainty associated with comparing vibrational frequencies measured in salts and aqueous species can be combined with uncertainties arising from likely errors in MUBFF modeling to give a rough estimate of the accuracy of calculated reduced partition function ratios. The combined error is calculated by taking the square root of the sum of the squares of the two types of propagated errors. At 298 K, $1000 \cdot \ln(\beta_{56-54})$ calculated for $[Fe^{III}Cl_4]^-$, $[Fe^{III}Br_4]^-$, $[Fe^{III}Cl_6]^{3-}$, and $[Fe^{III}(H_2O)_6]^{3+}$ have estimated

uncertainties of ±0.6, ±0.5, ±0.2, and at least ±0.9, respectively. Only one set of infrared measurements for $[Fe^{III}(H_2O)_6]^{3+}$ is available (BEST et al., 1980), and the uncertainty estimate does not include possible errors arising from the infrared data. Mixed aquo-chloro complexes are modeled based on incomplete information, and are not as well constrained as the other complexes. Agreement within ~0.5 per mil in the two calculations of $1000 \cdot \ln(\beta_{56-54})$ for $[Fe^{III}Cl_2(H_2O)_4]^+$ tentatively suggests that the accuracy of calculations for aquo-chloro complexes is similar to that for aquo complexes. In general, errors are largest for complexes that tend to concentrate the heavy isotopes. Thus, $[Fe^{II}Cl_4]^{2-}$ and $[Fe^{II}(H_2O)_6]^{2+}$ may have uncertainties that are similar to or somewhat smaller than their ferric analogues.

For hexacyano complexes, and particularly for $[Fe^{II}(CN)_6]^{4-}$, the major possible source of error is a disagreement between one force-field model (HIPPS et al., 1984) and other force-fields, as well as the perturbation method we have developed. Calculated with the HIPPS et al. (1984) force field, $1000 \cdot \ln(\beta_{56-54})$ for $[Fe^{II}(CN)_6]^{4-}$ is 12.9 at 298 K, 4.4 per mil lower than the NAKAGAWA and SHIMANOUCHI (1962) force field suggests, and 4.7 per mil lower than our perturbation-model calculation (Appendix 1). By contrast, two published force fields for $[^{54}Fe^{II}(CN)_6]^{3-}$ yield $1000 \cdot \ln(\beta_{56-54}) \approx 13.7$ at 298 K (NAKAGAWA and SHIMANOUCHI, 1962; SWANSON and RAFALKO, 1976), very close to our perturbation model estimate (14.1). Errors in estimating vibrational frequency shifts upon isotopic substitution made using the perturbation method propagate to errors in $1000 \cdot \ln(\beta_{56-54})$ of approximately ±2 and ±1 per mil for $[Fe^{II}(CN)_6]^{4-}$ and $[Fe^{III}(CN)_6]^{3-}$, respectively, and ±3 per mil in $1000 \cdot \ln(\beta_{57-54})$ for $[Fe^{II}(CN)_6]^{4-}$ (all at 298 K). If the HIPPS

et al. (1984) force field is correct, however, then we are overestimating $1000 \cdot \ln(\beta_{56-54})$ by roughly twice this much.

2.4. Discussion

2.4.1. Factors Controlling the Predicted Fractionations

The results clearly predict that measurable equilibrium fractionations of the stable iron isotopes can occur between simple species at relatively low temperatures. Variations of 1 per mil or more should be evident when iron-bearing complexes with different ligands or oxidation states equilibrate. The simple complexes studied here give some insight into the properties controlling equilibrium fractionation of the iron isotopes.

The most important factor controlling the model prediction of the reduced partition function ratio is the frequency of the asymmetric stretching vibration. This can be seen in Fig. 2.3a, which plots $1000 \cdot \ln(\beta_{56-54})$ against v_3 (the asymmetric stretching frequency) for the halogeno and hexaaquo complexes listed in Table 2.2. The strong relationship between v_3 and $1000 \cdot \ln(\beta)$, in turn, suggests that strongly bonding ligands will preferentially incorporate the heavier isotopes of iron. That correlation is evident in Fig. 2.3b, which plots $1000 \cdot \ln(\beta_{56-54})$ against the position of the ligands Br^-, Cl^-, H_2O, and CN^- on the spectrochemical series (found in any inorganic chemistry text, i.e., COTTON and WILKINSON, 1988), a rough indicator of relative covalent bonding strength. The cyanide ligand (CN^-), which is near the top of the series and forms highly covalent bonds with transition metals, forms complexes with the largest calculated reduced partition function ratios. The H_2O ligand, near the middle of the series, is intermediate, and ligands at bottom of the series (Br^-, Cl^-) form complexes with the smallest reduced partition

function ratios. The ~3 per mil (at 298 K) predicted fractionation between tetrahedral and octahedral chloro-complexes of Fe(III) is also consistent with the relatively greater bond-strengths predicted for complexes with lower coordination numbers. This coordination-number effect contrasts with results given by eqn. 21 of BIGELEISEN and MAYER (1947), which predicts a reversed direction of fractionation.

The importance of the oxidation state of the iron atom in determining isotope partitioning behavior is evident. There are significant (~3 to 5 per mil at 298 K) differences in the predicted reduced partition function ratios for Fe(II) and Fe(III) complexes with a given ligand, be it Cl^-, H_2O, or CN^-. Fe(III)-bearing aquo and halogeno complexes are predicted to concentrate the heavier isotopes relative to their Fe(II)-bearing counterparts. The reverse is predicted for cyano-complexes, possibly as a result of the π-backbonding tendency of the CN^- ligand. Cyano-complexes are probably an exception to a general rule, because Fe(III)-ligand vibrations are at higher frequencies than corresponding Fe(II)-ligand vibrations in most geochemically relevant complexes and minerals. Therefore, we confirm the prediction of POLYAKOV and MINEEV (2000) that Fe(III)-bearing complexes should usually be isotopically heavier than coexisting Fe(II)-bearing complexes in otherwise similar bonding situations.

2.4.2. Comparison with Experimental Results

The accuracy of these predictions will ultimately be determined by comparison with experimental measurements in the laboratory and natural systems. There is presently little data that can be used to directly evaluate our models. The experiment performed by BEARD et al. (1999) is broadly consistent with the trends observed here, in that they measure significant fractionations, with Fe(III)-bearing ferrihydrite apparently

concentrating the heavier iron isotopes relative to bacterially reduced Fe(II) in solution. It is important to note, however, that the experimentally observed variations clearly involve biological activity, and may not correspond to equilibrium fractionations.

ANBAR et al. (2000) observe a small but measurable fractionation between ferric iron species in solution and bound to an exchange resin. This may correspond to the equilibrium fractionation between $[Fe^{III}Cl_4]^-$, the species bound to the exchange resin, and $[Fe^{III}(H_2O)_mCl_n]^{3-n}$ species in 2M HCl solution. The speciation model of BJERRUM and LUKES (1986) for $Fe^{III} + Cl^-$ solutions suggests that a trichloro-complex (n = 3) is dominant in 2M HCl solution, the *trans*-dichloro-complex (n=2) may also be important. The $^{56}Fe/^{54}Fe$ ratios of $[Fe^{III}(H_2O)_3Cl_3]^0$ and *trans*-$[Fe^{III}(H_2O)_4Cl_2]^+$ are predicted to be ~0.5 per mil and ~1.3 to 1.8 per mil higher, respectively, than coexisting $[Fe^{III}Cl_4]^-$ in equilibrium at 298 K. Although we cannot rigorously quantify the uncertainty limits of this prediction, a rough estimate of ±1.1 per mil seems reasonable, based on independent uncertainties of ±0.6 per mil for $[Fe^{III}Cl_4]^-$ and ~±0.9 per mil for *trans*-$[Fe^{III}(H_2O)_4Cl_2]^+$ and $[Fe^{III}(H_2O)_3Cl_3]^0$. The fractionation measured in ANBAR et al.'s (2000) experiment is ~0.1 per mil, in agreement within our estimated uncertainty. Unpublished experiments using isotopically labeled reagents (Clark Johnson, private communication) suggest that the fractionation measured by ANBAR et al. (2000) is largely kinetic, and that the equilibrium fractionation in this system is ~0.5 per mil, very close to the predicted fractionation between the tetrachloro- and trichloro-complexes.

2.4.3. Applications to Natural Samples

The ideal situations for finding measurable inorganic fractionations correspond to the lithologies where fractionations have already been found: banded iron formations and

Fe-Mn nodules and crusts formed from solution at low temperatures near redox

boundaries (ANBAR et al., 2000; BEARD and JOHNSON, 1999; BEARD et al., 1999; ZHU et

al., 2000). Other processes likely to lead to large fractionations are those in which a

variety of ligands are active in binding iron. Low temperature formation of sulfides in

reducing sediments is one such example. The role of biological processing in the

expression of iron-isotope variability is unclear at present. One possibility is that

biochemistry facilitates the equilibration of distinct iron-bearing species, for instance by

aiding in precipitation or dissolution and providing low-energy-barrier intermediates for

exchange. In that case, the observed fractionations in biological systems will be at least

qualitatively explicable in terms of equilibrium partitioning. Another likely process for

biological influence is the biochemical sequestration and secretion of iron, with binding

to organic ligands (i.e., siderophores) and non-equilibrium separation of the inorganic or

organic products of ingested iron. Observed fractionations in this case might be expected

to be dominantly vital, with light isotopes of iron being selectively incorporated, and the

isotopic compositions of products being more sensitive to the specific biochemistry of the

organisms involved than the equilibrium fractionation between the phases ingested and

secreted as a net result of the biological processing.

The observation that igneous rocks apparently have a very narrow range of $^{56}Fe/^{54}Fe$

ratios (BEARD et al., 1999) is not unexpected, given the predictions made here. The high

temperatures characteristic of igneous processes (T > 1000 K) lead to fractionations that

are an order of magnitude smaller than at 298 K. In addition, the iron budgets of most

crustal (and certainly igneous) rocks will be dominated by a restricted range of iron-

bearing phases: ferrous iron in silicate minerals in 6-fold or 8-fold coordination with

oxygen. The uniformity of iron-hosting phases will be compounded by the tendency of magmas to "average" the compositions of their parent rocks.

2.5. Conclusions

The equilibrium fractionation behavior of the stable iron isotopes has been investigated using published vibrational spectra and simplified force-field modeling to calculate reduced partition function ratios for iron isotope exchange in simple chemical systems. Measurable fractionations are predicted to occur between coexisting species in equilibrium, with the magnitude and direction of fractionation being determined primarily by ligand bond-strength, the oxidation state of iron, and the coordination number of the iron in the complex or molecule of interest. Complexes with strong-bonding ligands like CN^- and H_2O will concentrate heavy isotopes of iron relative to complexes with more weakly bonding ligands like Cl^- and Br^-. Fe(III)-bearing complexes should usually concentrate the heavy isotopes relative to Fe(II)-bearing complexes, although hexacyano complexes appear to be a significant exception to this rule. Tetrahedral complexes (such as $[Fe^{III}Cl_4]^-$) should concentrate heavy isotopes relative to octahedral complexes (such as $[Fe^{III}Cl_6]^{3-}$). Calculated reduced partition function ratios for $[Fe^{II}(CN)_6]^{4-}$ and α-Fe metal are in quantitative agreement with the predictions made by the Mössbauer-based technique of POLYAKOV (1997). The sense of predicted fractionations for chloro- and mixed aquo-chloro complexes agrees with recent measurements of inorganic fractionations in the laboratory (ANBAR et al., 2000; Clark Johnson private communcation).

Our results suggest that good places to look for significant inorganic fractionations of the iron isotopes are in low-temperature environments in which reduction or oxidation

of iron takes place, or in environments where more than one ligand, or bonding partner, is interacting with iron atoms. These are precisely the environments where variability in iron isotope ratios has been observed, and it will be necessary to exercise caution before interpreting these variations in terms of biological activity.

2.6. Bibliography

Adams D. M. and Morris D. M. (1968) Vibrational spectra of halides and complex halides. Part IV. Some tetrahalogenothallates and the effects of d-electronic structure on the frequencies of hexachlorometallates. *J. Chem. Soc. A*, 694-695.

Anbar A. D., Roe J. E., Barling J., and Nealson K. H. (2000) Non-biological fractionation of iron isotopes. *Science* **288**, 126-128.

Avery J. S., Burbridge C. D., and Goodgame D. M. L. (1968) Raman spectra of tetrahaloanions of Fe^{III}, Mn^{II}, Fe^{II}, Cu^{II}, and Zn^{II}. *Spectrochim. Acta* **24A**, 1721-1726.

Beard B. L. and Johnson C. M. (1999) High precision iron isotope measurements of terrestrial and lunar materials. *Geochim. Cosmochim. Acta* **63**, 1653-1660.

Beard B. L., Johnson C. M., Cox L., Sun H., Nealson K. H., and Aquilar C. (1999) Iron isotope biosignatures. *Science* **285**, 1889-1892.

Bergsma J., Van Dijk C., and Tocchetti D. (1967) Normal vibrations in α-iron. *Physics Letters* **24A**, 270-272.

Best S. P., Armstrong R. S., and Beattie J. K. (1980) Infrared metal-ligand vibrations of hexaaquametal(III) ions in alums. *Inorg. Chem.* **19**, 1958-1961.

Best S. P., Beattie J. K., and Armstrong R. S. (1984) Vibrational spectroscopic studies of trivalent hexa-aqua cations: single-crystal Raman spectra between 275 and 1200

cm^{-1} of the caesium alums of titanium, vanadium, chromium, iron, gallium, and indium. *J. Chem. Soc. Dalton Trans.*, 2611-2624.

Bigeleisen J. and Mayer M. G. (1947) Calculation of equilibrium constants for isotopic exchange reactions. *J. chem. Phys.* **15**, 261-267.

Bjerrum J. and Lukes I. (1986) The iron(III) chloride system — A study of the stability-constants and of the distribution of the tetrachloro species between organic-solvents and aqueous chloride solutions. *Acta Chem. Scand. Series A - Phys. Inorg. Chem.* **40**, 31-40.

Brockhouse B. N., Abou-Helal H. E., and Hallman E. D. (1967) Lattice vibrations in iron at 296°K. *Solid State Commun.* **5**, 211-216.

Brunet H. and Perez M. (1969) The v_3 and v_4 bands of sulfur hexafluoride. *J. Mol. Spectrosc.* **29**, 472-477.

Cotton F. A. and Wilkinson G. (1988) *Advanced Inorganic Chemistry.* Wiley-Interscience.

Hipps K. W., Williams S. D., and Mazur U. (1984) Forbidden vibrational modes in iron(II), ruthenium(II), osmium(II) hexacyanides: A tunneling, IR, and Raman spectroscopy study. *Inorg. Chem.* **23**, 3500-3505.

Housley R. M. and Hess F. (1967) Analyses of Debye-Waller-factor and Mössbauer-thermal-shift measurements II. Thermal-shift data on iron. *Phys. Rev.* **164**, 340-344.

Jones L. H., Swanson B. I., and Kubas G. J. (1974) Vibrational analysis using crystalline models: Vibrational spectra and potential constants for $Cs_2LiFe(CN)_6$. *J. Chem. Phys.* **61**, 4650-4655.

Kanno H. and Hiraishi J. (1982) A Raman study of aqueous solutions of ferric nitrate, ferrous chloride, and ferric chloride in the glassy state. *J. Raman Spectrosc.* **12**, 224-227.

Kermarrec Y. (1964) Spectres d'absorption infrarouge de cations métalliques avec six molécules d'eau de coordination. (Infrared absorption spectra of metal cations with six coordinated water molecules). *Compte. Rend. Acad. Sci. Paris* **258**, 5836-5838.

Kieffer S. W. (1982) Thermodynamics and lattice vibrations of minerals: 5. Applications to phase equilibria, isotopic fractionation, and high-pressure thermodynamic properties. *Rev. Geophys. Space Phys.* **20**, 827-849.

Konya K. and Nakamoto K. (1973) Infrared studies of coordination compounds containing high oxidation-state metals - I. Diarsine complexes. *Spectrochim. Acta* **29A**, 1965-1973.

Lassegues J. C., Grondin J., Hernandez M., Rey I., Servant L., and Wen S.-J. (1996) Spectroscopic study of the complexation between nylon-6 and $FeCl_3$. *New J. Chem.* **20**, 317-329.

Michalska-Fong D., McCarthy P. J., and Nakamoto K. (1983) Infrared and Raman spectra of trans-$[MX_2(H_2O)_4]^+$ type complex ions (M = Ti(III), V(III), Cr(III) and X = Cl and Br). *Spectrochim. Acta* **39A**, 835-842.

Murata K. and Irish D. E. (1988) Raman studies hydrated melt of $FeCl_3 \cdot 6H_2O$. *Spectrochim. Acta* **44A**, 739-743.

Nakagawa I. and Shimanouchi T. (1962) Infrared spectroscopic study on the co-ordination bond-II. Infrared spectra of octahedral metal cyanide complexes. *Spectrochim. Acta* **18**, 101-113.

Nakagawa I. and T. S. (1964) Infrared absorption spectra of aquo complexes and the nature of co-ordination bonds. *Spectrochim. Acta* **20**, 429-439.

Nakamoto K. (1997) *Infrared and raman spectra of inorganic and coordination compounds*. John Wiley & Sons, Inc.

Parrington J. R., Knox H. D., Breneman S. L., Baum E. M., and Feiner F. (1996) *Chart of the Nuclides*. General Electric Co. and KAPL Inc.

Polyakov V. B. (1997) Equilibrium fractionation of the iron isotopes: Estimation from Mössbauer spectroscopy data. *Geochim. Cosmochim. Acta* **61**, 4213-4217.

Polyakov V. B. and Mineev S. D. (2000) The use of Mössbauer spectroscopy in stable isotope geochemistry. *Geochim. Cosmochim. Acta* **64**, 849-865.

Richet P., Bottinga Y., and Javoy M. (1977) A review of hydrogen, carbon, nitrogen, oxygen, sulphur, and chlorine stable isotope fractionation among gaseous molecules. *Ann. Rev. Earth Planet. Sci.* **5**, 65-110.

Shamir J. (1991) Raman and infrared spectra of the $FeCl_6^{3-}$ anion: comparison of MCl_4 and MCl_6 vibrational frequencies. *J. Raman Spectrosc.* **22**, 97-99.

Simanouti (Shimanouchi) T. (1949) The normal vibrations of polyatomic molecules as treated by Urey-Bradley field. *J. Chem. Phys.* **17**, 245-248.

Swanson B. I. and Rafalko J. J. (1976) Perturbation of intramolecular vibrations by strong interionic forces: vibrational spectra and assignments for $Fe(CN)_6^{4-}$ and $Cs_2MgFe(CN)_6$. *Inorg. Chem.* **15**(2), 249-253.

Thiele G., Honert D., and Rotter H. (1992) Preparation and characterization of tetrabromoferrates(II) $AFeBr_4$ with monvalent cations A = Cs, Rb, Tl, NH_4, K, Na, Li, Ag. *Z. anorg. allg. Chem.* **616**, 195-200.

Urey H. C. (1947) The thermodynamic properties of isotopic substances. *J. Chem. Soc.*, 562-581.

Wilson E. B., Jr., Decius J. C., and Cross P. C. (1955) *Molecular Vibrations.* Dover.

Zakharieva-Pencheva O. and Dementiev V. A. (1982) Calculation of IR- and Raman-active vibrations of hexacyano complexes of Fe^{II}, Co^{III}, Mn^{II}, Cr^{III}, V^{II}. *J. Mol. Struct.* **90**, 241-248.

Zhu X.-K., O'Nions R. K., Guo Y., and Reynolds B. C. (2000) Secular variation of iron isotopes in North Atlantic Deep Water. *Science* **287**, 2000-2002.

Appendix 1. Notes on Vibrational Spectroscopy and Prediction of Frequency Shifts

A-1.1. Halogeno Complexes

Complexes of iron with halide ions are in many respects the simplest multiple-element compounds to model. Halogeno complexes tend to have high symmetry; the ones studied here are essentially tetrahedral (T_d) or octahedral (O_h). In addition, they have a small number of atoms, which greatly simplifies vibrational modeling. For each halogeno complex, a three-parameter Modified Urey-Bradley Force field (MUBFF) is generated to match observed vibrational frequencies using a least-squares minimization procedure. Tetrahedral XY_4 complexes have four distinct fundamental vibrational frequencies, and octahedral XY_6 complexes have five measurable distinct fundamental vibrational frequencies (a sixth fundamental mode is neither infrared-active nor Raman-active), so the three force-field parameters in the MUBFF for each complex are overconstrained. Stretching-mode vibrational frequencies calculated by the MUBFF are generally within a few percent of the observed frequencies, and calculated bending-mode frequencies are within about 10% of observed frequencies. Similar magnitudes of disagreement between calculated and measured frequencies are also observed in the molecules and complexes listed in Table 2.1. Ligand isotopic heterogeneity in chloro- and bromo-complexes is ignored in model calculations; uniform atomic masses of 35.453 amu and 79.904 amu are assumed for chlorine and bromine, respectively (PARRINGTON et al., 1996).

A-1.2. Hexaaquo Complexes

Force-field models of hexaaquo and mixed aquo-chloro complexes use the "point mass" approximation, which means that each complexed H_2O group is assumed to

behave as a single point mass. The effect of the point mass approximation is to reduce a 19-atom hexaaquo complex of ~D_{4h} symmetry to a much simpler 7-"atom" structure of O_h symmetry, which can then be modeled with the same procedure described above for hexahalogeno complexes. The point mass approximation is possible because O-H stretching and bending frequencies are much higher than Fe-O stretching and bending frequencies, and the two types of motion are expected to be more or less independent of each other. Some of the Fe-OH$_2$ distortion modes, the so-called "wagging" and "rocking" vibrations, occur at frequencies below 1000 cm^{-1} (NAKAGAWA and T., 1964), however, and there is a possibility of significant coupling between these modes and the Fe-isotope sensitive Fe-O stretching mode. We can test the point mass approximation using available vibrational spectra of isotopically substituted hexaaquo complexes. In Table 2.1, the measured isotopic frequency shift of the asymmetric Cr-O stretch (ν_3) in ^{53}Cr- and ^{50}Cr-substituted $[Cr(H_2O)_6]^{3+}$ (BEST et al., 1980) is compared to the shift predicted by a MUBFF generated using the point mass approximation. The observed shift of 5 cm^{-1} (accuracy unknown) is in rough agreement with a predicted shift of 6.3 cm^{-1}. Similarly, the fairly good match between the observed and predicted effects of deuteration on the Raman-active octahedral modes (ν_1, ν_2, and ν_5) in $[Fe^{III}(H_2O)_6]^{3+}$ (BEST et al., 1984) suggests that hydrogen is behaving more or less like a rigidly attached component of the water ligand in these vibrations, an important criterion for applying the point mass approximation. Together, the Cr-isotope and D-H substitution data justify the point mass approximation for hexaaquo iron.

A-1.3. Hexacyano Complexes

The vibrational spectra of iron hexacyano complexes have been extensively studied

(e.g., HIPPS et al., 1984; JONES et al., 1974; NAKAGAWA and SHIMANOUCHI, 1962; ZAKHARIEVA-PENCHEVA and DEMENTIEV, 1982). By symmetry, only the four triply degenerate F_{1u} vibrations of a hexacyano complex are sensitive to the mass of the central metal atom; these vibrations are conventionally numbered ν_6 -ν_9 in order of decreasing frequency. It has been shown that ν_7 and ν_8 each involve a mixture of Fe-C-N bending and Fe-C stretching motions, (HIPPS et al., 1984; ZAKHARIEVA-PENCHEVA and DEMENTIEV, 1982). The force fields given by HIPPS et al. (1984) and JONES et al. (1974) are both reasonably accurate in reproducing vibrational frequencies of isotopically normal, ^{13}C-substituted, and ^{15}N-substituted iron hexacyano complexes, but they disagree substantially in their estimates of the sensitivity of ν_7 to substitution of ^{54}Fe.

To get around the disagreements between published force fields, $^{56}\nu_7/^{54}\nu_7$ and $^{56}\nu_8/^{54}\nu_8$ for both $[Fe^{II}(CN)_6]^{4-}$ and $[Fe^{III}(CN)_6]^{3-}$ are calculated directly from the measured vibrational spectra of isotopically normal, ^{15}N-substituted, and ^{13}C-substituted $[Fe^{II}(CN)_6]^{4-}$ (HIPPS et al., 1984). This can be done using the following equation, which is derived in Appendix 2 from the first-order perturbation treatment of isotopic mass effects in WILSON et al. (1955, pp. 188-190):

$$\frac{\left(^{15N}\nu_n/\nu_n\right)^2 - 1}{\left(m_N/m_{15N}\right) - 1} + \frac{\left(^{13C}\nu_n/\nu_n\right)^2 - 1}{\left(m_C/m_{13C}\right) - 1} + \frac{\left(\nu_n/^{54Fe}\nu_n\right)^2 - 1}{\left(m_{54Fe}/m_{Fe}\right) - 1} = 1 \qquad (1)$$

where m_i is the mass of element or isotope i and $^i\nu_n$ is the frequency of ν_n in the complex substituted with isotope i. Allowing for possible errors of ± 1 cm^{-1} in the measured frequency shifts in ^{13}C- and ^{15}N-substituted $[Fe^{II}(CN)_6]^{4-}$ (K. W. Hipps, private

communication), $^{56}\nu_7/^{54}\nu_7 = 0.9916 \pm 0.0013$ and $^{56}\nu_8/^{54}\nu_8 = 0.9976 \pm 0.0018$ by this

method. Similar results ($^{56}\nu_7/^{54}\nu_7 = 0.9928 \pm 0.0014$) are obtained by performing the

same calculation with the frequencies of ν_7 in isotopically normal, ^{13}C-substituted, and

^{15}N-substituted $[Fe^{III}(CN)_6]^{3-}$ (JONES et al., 1974); for ν_8 the Jones et al. spectra are less

precise, leading to $^{56}\nu_8/^{54}\nu_8 = 0.9944 \pm 0.0036$. Our calculated shifts for both

$[Fe^{III}(CN)_6]^{3-}$ and $[Fe^{II}(CN)_6]^{4-}$ are in close agreement with the JONES et al. (1974) force

field, which predicts $^{56}\nu_7/^{54}\nu_7 \approx 0.992$. We have chosen to use the $^{56}\nu_n/^{54}\nu_n$ ratios

calculated from the HIPPS et al. (1984) measurements to model both complexes because

a) the calculated $^{56}\nu_8/^{54}\nu_8$ is more precise, b) the product ($^{56}\nu_7/^{54}\nu_7$)•($^{56}\nu_8/^{54}\nu_8$) is in close

agreement with the force fields of NAKAGAWA and SHIMANOUCHI (1962), and HIPPS et al.

(1984), and c) the measured spectra and force field of JONES et al. (1974), particularly for

ν_8, are slightly affected by lattice effects arising from mixing with the Li-N stretching

vibration in the salt they studied, $Cs_2Li[Fe^{III}(CN)_6]$. The force fields of NAKAGAWA and

SHIMANOUCHI (1962), HIPPS et al. (1984), and JONES et al. (1974) each predict that the

metal-isotope sensitivities of equivalent vibrational modes in the ferric and ferrous

hexacyano complexes are similar.

The C-N stretching frequency ν_6 is largely insensitive to the mass of the central

metal atom, the force fields of NAKAGAWA and SHIMANOUCHI (1962), JONES et al.

(1974), and HIPPS et al. (1984) all predict $^{56}\nu_6/^{54}\nu_6 > 0.99997$. A value of 0.99998 is used

for the model. The Redlich-Teller product rule (WILSON et al., 1955; pg. 183); predicts

that the product $\Pi_{i=6}^{9}(^{56}\nu_i/^{54}\nu_i) \approx 0.9867$, allowing estimation of the isotopic sensitivity of

ν_9 (a C-Fe-C bend); $^{56}\nu_9/^{54}\nu_9 \approx 0.9974$ by this method. Table 2.3 provides a summary of

observed and predicted vibrational frequencies of iron hexacyano complexes.

A reduced partition function ratio for ^{57}Fe - ^{54}Fe exchange in $[Fe^{II}(CN)_6]^{4-}$ was also calculated by the same method, for comparison with the results for $K_4Fe(CN)_6$ and $K_4Fe(CN)_6 \cdot 3H_2O$ of POLYAKOV (1997), (Fig. 2.2).

A-1.4. Metallic Iron (α-Fe)

The vibrational (phonon) spectrum of α-Fe metal has been extensively studied by inelastic neutron scattering (i.e., BERGSMA et al., 1967; BROCKHOUSE et al., 1967)). The unit cell of α-Fe consists of one atom, and there are three acoustic vibrational modes. Vibrational frequencies in metallic iron are low, the maximum frequency of the longitudinal mode barely reaches 300 cm^{-1} near the edge of the Brillouin zone. The phonon density of states calculated by BROCKHOUSE et al. (1967) is used to calculate the isotopic partition function ratio. Phonon oscillation frequencies for α-^{54}Fe are assumed to be shifted upwards by $[m(^{56}Fe)/m(^{54}Fe)]^{1/2}$ (≈ 1.0183) relative to the observed distribution in normal α-Fe, which is assumed to be equivalent to pure α-^{56}Fe. The reduced isotope partition function ratio for ^{56}Fe-^{54}Fe exchange was then calculated according to equations (15) - (17) of KIEFFER (1982). A reduced partition function ratio for ^{57}Fe-^{54}Fe exchange was also calculated for comparison with the results of POLYAKOV (1997), (Fig. 2.2).

A-1.5. Mixed Aquo-chloro Complexes

Recent work by ANBAR et al. (2000) has provided the first evidence of measurable inorganic ^{56}Fe-^{54}Fe fractionations between species in solution and bound to an ion exchange resin. The oxidized, 2 M HCl solution chemistry of Anbar et al.'s system is such that mixed ferric aquo-chloro complexes are the dominant dissolved species

(BJERRUM and LUKES, 1986); the most likely complexes are $[Fe^{III}(H_2O)_4Cl_2]^+$ (with the Fe-Cl bonds opposing each other, e.g., in the *trans*- configuration) and a poorly defined $[Fe^{III}(H_2O)_xCl_3]^0$ of unknown geometry (Anbar et al., 2000). The strongly basic exchange resin Anbar et al. used binds tetrahedral $[FeCl_4]^-$ anions, which have already been discussed above. In the case of the *trans*-dichloro complex, two Raman frequencies corresponding to the symmetric Fe-O and Fe-Cl, stretches have been reported (KANNO and HIRAISHI, 1982; MURATA and IRISH, 1988). The trichloro complex has not been studied spectroscopically.

A simple, rough estimate of the reduced partition function ratios of mixed aquo-chloro complexes of octahedral geometry can be obtained as a weighted average of the hexaaquo and hexachloro complexes they resemble, i.e.,

$$1000 \cdot \ln(\beta)_{[Fe^{III}(H_2O)_4Cl_2]^+} \approx 2/3 \cdot 1000 \cdot \ln(\beta)_{[Fe^{III}(H_2O)_6]^{3+}} + 1/3 \cdot 1000 \cdot \ln(\beta)_{[Fe^{III}Cl_6]^{3-}}$$

$$1000 \cdot \ln(\beta)_{[Fe^{III}(H_2O)_3Cl_3]^0} \approx 1/2 \cdot 1000 \cdot \ln(\beta)_{[Fe^{III}(H_2O)_6]^{3+}} + 1/2 \cdot 1000 \cdot \ln(\beta)_{[Fe^{III}Cl_6]^{3-}}$$

This is a rough approximation, but might give reasonable results if Fe-ligand bonding is similar in the simple and mixed complexes. The results of this model approach are labeled "#1" on Fig. 2.1 and in Table 2.4.

The two reported vibrational frequencies for $[Fe^{III}(H_2O)_4Cl_2]^+$ in solution, at ~425 cm^{-1} for the symmetric (A_{1g}) Fe-O stretch and ~319 cm^{-1} for the symmetric (A_{1g}) Fe-Cl stretch (MURATA and IRISH, 1988), are somewhat different from the A_{1g} symmetric stretching frequencies of $[Fe^{III}(H_2O)_6]^{3+}$ (500 cm^{-1}) in solution and $[Fe^{III}Cl_6]^{3-}$ (281 cm^{-1}) in $[Co(NH_3)_6][FeCl_6]$ (ADAMS and MORRIS, 1968; SHAMIR, 1991). This suggests that while the calculation scheme used above is a useful approximation, comparison to a more detailed model is desirable. Such a comparison is possible for the *trans*-dichloro

complex, with some help from the force field developed for *trans*-[Cr^{III}(H$_2$O)$_4$Cl$_2$]$^+$ by

MICHALSKA-FONG et al. (1983).

The vibrational spectrum of the *trans*-[Cr^{III}(H$_2$O)$_4$Cl$_2$]$^+$ complex is much better

known than is the case for the ferric analogue; 9 of the 11 expected distinct frequencies

have been measured. Based on these frequencies, and vibrational frequencies for the

related *trans*-[V^{III}(H$_2$O)$_4$Cl$_2$]$^+$ and *trans*-[Ti^{III}(H$_2$O)$_4$Cl$_2$]$^+$ complexes, MICHALSKA-FONG

et al. (1983) proposed a MUBFF-like force field for trivalent *trans*-dicholoro complexes

(it differs slightly from the MUBFF used in the present work by including *trans*-bond-

stretch interaction terms between the two pairs of opposing M-O bonds, and between the

opposing M-Cl bonds). If we adapt the Michalska-Fong et al. force-field model for *trans*-

[Fe(H$_2$O)$_4$Cl$_2$]$^+$ by changing the M-Cl and M-O stretching constants to match the

observed symmetric stretch frequencies, it is possible to predict the frequencies and

isotopic frequency shifts of the metal-isotope sensitive vibrational modes. By this

method, the asymmetric Fe-Cl stretch is predicted to occur near 400 cm^{-1} with $^{56}\nu/^{54}\nu \approx$

0.989 and the asymmetric Fe-O stretch is predicted to be $\sim$ 425 cm^{-1} with $^{56}\nu/^{54}\nu \approx 0.993$,

with other metal-isotope sensitive frequencies at 270 cm^{-1} (E$_u$, $^{56}\nu/^{54}\nu \approx 0.997$), 240 cm^{-1}

(A$_{2u}$, $^{56}\nu/^{54}\nu \approx 0.997$), and 110 cm^{-1} (E$_u$, $^{56}\nu/^{54}\nu \approx 0.997$). The calculated asymmetric

Fe-Cl stretching frequency can be compared with values measured in [Fe(dias)$_2$Cl$_2$]$^+$

(380 cm^{-1}, KONYA and NAKAMOTO, 1973)) and in the *trans*-[Fe(L')$_4$Cl$_2$]$^+$ complex

formed by the reaction of ferric chloride with nylon-6 (372 cm^{-1}, LASSEGUES et al.,

1996), suggesting that the model slightly overestimates this frequency. The observation

by KERMARREC (1964) of a strong infrared absorption band near 374 cm^{-1} in crystalline

FeCl$_3$•6H$_2$O (which contains the *trans*-[Fe(H$_2$O)$_4$Cl$_2$]$^+$ structure) is also consistent with a

somewhat lower Fe-Cl stretching frequency than is predicted by the model. An Fe-Cl

stretching frequency of 375 cm^{-1} is used in the calculations. The model isotopic partition

function ratio calculated by this method is labeled "#2" on Fig. 2.1.

38

Appendix 2. Derivation of Equation (1)

This Appendix gives a step-by-step derivation of equation (1) from the perturbation treatment for small mass changes given by Wilson et al. (1955, pp. 188-190, hereafter abbreviated as WDC). It is necessary to introduce a number of symbols from WDC which do not appear in the final equation. A descriptive glossary of these terms is provided at the end of the Appendix.

From WDC, p. 190, equations (36) and (38):

$$\lambda_k = \lambda_k^0 + \lambda_k^0 \cdot \sum_{tt'} \left(L_0^{-1}\right)_{kt} \left(L_0^{-1}\right)_{kt'} \Delta G_{tt'} \tag{36}$$

and

$$G_{tt'}^0 = \sum_{\alpha} s_{t\alpha} \cdot s_{t'\alpha} \mu_\alpha \tag{38}$$

In the case of a molecule containing three elements (i.e. $X_i Y_j Z_k$), (38) can be written out as

$$G_{tt'}^0 = \sum_X s_{tX} \cdot s_{t'X} \mu_X + \sum_Y s_{tY} \cdot s_{t'Y} \mu_Y + \sum_Z s_{tZ} \cdot s_{t'Z} \mu_Z$$

Substitution of a proportional isotopic mass-shift parameter, defined as $\rho_n = \frac{\mu_n^*}{\mu_n} \approx 1$, where μ_n^* is the reciprocal mass of the substituted isotope of element n, gives the following:

$$G_{tt'} = \sum_X s_{tX} \cdot s_{t'X} \mu_X \rho_X + \sum_Y s_{tY} \cdot s_{t'Y} \mu_Y \rho_Y + \sum_Z s_{tZ} \cdot s_{t'Z} \mu_Z \rho_Z$$

Then, taking the derivatives with respect to ρ_X, ρ_Y, and ρ_Z:

$$\frac{\partial G_{tt'}}{\partial \rho_X} = \sum_X s_{tX} \cdot s_{t'X} \mu_X$$

$$\frac{\partial G_{tt'}}{\partial \rho_Y} = \sum_Y s_{tY} \cdot s_{t'Y} \mu_Y$$

$$\frac{\partial G_{tt'}}{\partial \rho_Z} = \sum_Z s_{tZ} \cdot s_{t'Z} \mu_Z$$

Note that

$$\frac{\partial G_{tt'}}{\partial \rho_X} + \frac{\partial G_{tt'}}{\partial \rho_Y} + \frac{\partial G_{tt'}}{\partial \rho_Z} = G_{tt'}^0 \qquad (A\text{-}1)$$

Rewrite (36) in differential form with respect to ρ_X, ρ_Y, and ρ_Z:

$$\frac{\partial \lambda_{tt'}}{\partial \rho_X} = \lambda_k^0 \cdot \sum_{tt'} \left(L_0^{-1}\right)_{kt} \left(L_0^{-1}\right)_{kt'} \left(\frac{\partial G_{tt'}}{\partial \rho_X}\right) \qquad (A\text{-}2)$$

$$\frac{\partial \lambda_{tt'}}{\partial \rho_Y} = \lambda_k^0 \cdot \sum_{tt'} \left(L_0^{-1}\right)_{kt} \left(L_0^{-1}\right)_{kt'} \left(\frac{\partial G_{tt'}}{\partial \rho_Y}\right) \qquad (A\text{-}3)$$

$$\frac{\partial \lambda_{tt'}}{\partial \rho_Z} = \lambda_k^0 \cdot \sum_{tt'} \left(L_0^{-1}\right)_{kt} \left(L_0^{-1}\right)_{kt'} \left(\frac{\partial G_{tt'}}{\partial \rho_Z}\right) \qquad (A\text{-}4)$$

Equations (A-2), (A-3), and (A-4) are analogous to equation (40) in WDC p. 190. Add (A-2), (A-3), and (A-4), and apply (A-1) to the sum:

$$\frac{\partial \lambda_{tt'}}{\partial \rho_X} + \frac{\partial \lambda_{tt'}}{\partial \rho_Y} + \frac{\partial \lambda_{tt'}}{\partial \rho_Z} = \lambda_k^0 \cdot \sum_{tt'} \left(L_0^{-1}\right)_{kt} \left(L_0^{-1}\right)_{kt'} \left(\frac{\partial G_{tt'}}{\partial \rho_X} + \frac{\partial G_{tt'}}{\partial \rho_Y} + \frac{\partial G_{tt'}}{\partial \rho_Z}\right)$$

$$= \lambda_k^0 \cdot \sum_{tt'} \left(L_0^{-1}\right)_{kt} \left(L_0^{-1}\right)_{kt'} G_{tt'}^0$$

this relation can be simplified by applying equations (35), (36), (34), and (29) of WDC,

$$= [\Lambda^0 L_0^{-1} G^0 \left(L_0^{-1}\right)^\dagger]_{kk}$$

by (35) and (36),

$$= [L_0^\dagger F G^0 \left(L_0^{-1}\right)^\dagger]_{kk}$$

by (34),

$$= [\Lambda^0]_{kk}$$

$$= \lambda_k^0 \qquad (A\text{-}5)$$

by (29). Divide (A-5) by λ_k^0,

$$\frac{\partial \lambda_{tt'}}{\lambda_k^0 \partial \rho_X} + \frac{\partial \lambda_{tt'}}{\lambda_k^0 \partial \rho_Y} + \frac{\partial \lambda_{tt'}}{\lambda_k^0 \partial \rho_Z} = 1$$

and rewrite with Δ instead of ∂,

$$\partial \lambda_k \rightarrow \Delta \lambda_k = \lambda_k^{*n} - \lambda_k^0$$

$$\partial \rho_n \to \Delta \rho_n = \rho_n - 1 = \frac{\mu_n^*}{\mu_n} - 1$$

then

$$\frac{\lambda_k^{*X} - \lambda_k^0}{\lambda_k^0 \left(\frac{\mu_X^*}{\mu_X} - 1\right)} + \frac{\lambda_k^{*Y} - \lambda_k^0}{\lambda_k^0 \left(\frac{\mu_Y^*}{\mu_Y} - 1\right)} + \frac{\lambda_k^{*Z} - \lambda_k^0}{\lambda_k^0 \left(\frac{\mu_Z^*}{\mu_Z} - 1\right)} \approx 1$$

$$\frac{\left(\frac{\lambda_k^{*X}}{\lambda_k^0} - 1\right)}{\left(\frac{\mu_X^*}{\mu_X} - 1\right)} + \frac{\left(\frac{\lambda_k^{*Y}}{\lambda_k^0} - 1\right)}{\left(\frac{\mu_Y^*}{\mu_Y} - 1\right)} + \frac{\left(\frac{\lambda_k^{*Z}}{\lambda_k^0} - 1\right)}{\left(\frac{\mu_Z^*}{\mu_Z} - 1\right)} \approx 1$$

Finally, substituting $\lambda_k^i = 4\pi^2 c^2 \left(^i\nu_k\right)^2$ and $\mu_i = 1/m_i$,

$$\frac{\left(\frac{^{*X}\nu_k}{\nu_k}\right)^2 - 1}{\frac{m_X}{m_X^*} - 1} + \frac{\left(\frac{^{*Y}\nu_k}{\nu_k}\right)^2 - 1}{\frac{m_Y}{m_Y^*} - 1} + \frac{\left(\frac{^{*Z}\nu_k}{\nu_k}\right)^2 - 1}{\frac{m_Z}{m_Z^*} - 1} \approx 1 \tag{1}$$

Glossary

F Potential energy matrix.

G **and** G^0 Wilson G matrix, associated with the kinetic energy of vibration of the molecule. G^0 refers to the unsubstituted molecule.

L_0, L_0^{-1}, **and** $\left(L_0^{-1}\right)^\dagger$ The eigenvector matrix of $G^0 F$ is L_0. L_0^{-1} is the inverse of L_0, and $\left(L_0^{-1}\right)^\dagger$ is the complex conjugate of the transpose of L_0^{-1}.

λ_k, λ_k^0, **and** λ_k^{*n} Values of the kth eigenvalue of GF. λ_k^0 is the kth eigenvalue of $G^0 F$, i.e. of the unsubstituted molecule. λ_k^{*n} is the kth eigenvalue for a molecule substituted with isotope $^*n$. Each eigenvalue is related to a vibrational frequency by $\lambda_k = 4\pi^2 c^2 (\nu_k)^2$.

Λ^0 Diagonal matrix of eigenvalues of $G^0 F$.

m_n **and** μ_n Mass and reciprocal mass of element n.

m_n^* **and** μ_n^* Mass and reciprocal mass of the substituted isotope of element n.

ν_k Vibrational frequency of fundamental mode k in an unsubstituted molecule.

$^{*n}\nu_k$ Vibrational frequency of fundamental mode k in molecules substituted with isotope $^*n$.

s_{tn} **and** $s_{t'n}$ Vectors associated with the positions in the molecule occupied by atoms of element n and symmetry coordinates S_t and $S_{t'}$.

Table 2.1. Comparison between observed shifts in vibrational frequencies(v^*/v) in isotopically substituted tetrahedral and octahedral complexes and predictions made by the Modified Urey-Bradley Force Field (MUBFF). Vibrational modes v_3 and v_4 are the triply-degenerate asymmetric stretch and bend vibrations, respectively. The symmetry of each mode is indicated in parentheses.

Species	Studied Isotopes	Mode	Frequency (cm⁻¹)		$\Sigma[v_{obs}-v_{calc}]^2$	Frequency Ratio (v^*/v)		
			Observed[a]	MUBFF[§]		Observed	GVFF[†]	MUBFF[§]
SiCl$_4$	^{28}Si-^{30}Si	v_3 (F$_2$)	616.5	615.8	768	not obs.	0.9777	0.9779
		v_4 (F$_2$)	220.2	202.1		not obs.	0.9939	0.9938
	^{35}Cl-^{37}Cl	v_3 (F$_2$)	616.5	615.8		0.9908	0.9907	0.9906
SnCl$_4$	^{116}Sn-^{124}Sn	v_3 (F$_2$)	409.4±0.3	408.8	406	0.9914±0.0005	0.9911	0.9908
		v_4 (F$_2$)	126.8±0.3	112.1		not obs.	0.9909	0.9912
RuO$_4$	^{96}Ru-^{102}Ru	v_3 (F$_2$)	921.0±0.2	920.9	595	0.9943±0.0001	0.9944	0.9947
		v_4 (F$_2$)	336.0±0.2	318.3		not obs.	0.9937	0.9934
SF$_6$	^{32}S-^{34}S	v_3 (F$_{1u}$)	947.9	949.2	4525	0.9816	0.9821	0.9821
		v_4 (F$_{1u}$)	614.5	567.1		0.9946±0.0007	0.9946	0.9946
[SnCl$_6$]$^{2-}$	^{116}Sn-^{124}Sn	v_3 (F$_{1u}$)	303	302.9	393	0.9895±0.0026	0.9901	0.9914
		v_4 (F$_{1u}$)	166	153.8		not obs.	0.9886	0.9874
[PdCl$_6$]$^{2-}$	^{104}Pd-^{110}Pd	v_3 (F$_{1u}$)	346	358.2	954	0.9899±0.0015	0.9888	0.9890
		v_4 (F$_{1u}$)	200	182.8		not obs.	0.9926	0.9924
[Cr(H$_2$O)$_6$]$^{3+}$	^{50}Cr-^{53}Cr	v_3 (F$_{1u}$)[b]	555	594.4	4787	0.991	——	0.9888
[Fe(H$_2$O)$_6$]$^{3+}$	H-D	v_1 (A$_{1g}$)[b]	523		1912	0.956	——	0.9484
		v_2 (E$_g$)[b]	442±5			0.959±0.011	——	0.9484
		v_5 (F$_{2g}$)[b]	~317			0.956±0.010	——	0.9484

[a] All frequencies in this column were measured in samples prepared with the natural mixture of isotopes of the ligand atoms. For SiCl$_4$ and SF$_6$ the vibrational frequency shown is that reported for the complex containing ^{28}Si and ^{32}S, respectively. Otherwise the peak frequency of the natural-abundance mixture of metal-atom isotopes is reported.

[§] The MUBFF for all of these complexes contains three parameters. These were determined by an iterative least-squares fit to the fundamental vibrational frequencies observed in natural abundance isotopic mixtures. Tetrahedral (XY$_4$) complexes have four distinct fundamentals. Octahedral (XY$_6$) complexes have six, but the sixth is Raman- and infrared-inactive, so only five were used for fitting purposes. The total least-squares mismatch between modeled and observed frequencies is shown in the sixth column.

[†] "Exact" Generalized Valence Force-Field (GVFF) parameters are from cited references. The exact GVFF is a detailed force field with many parameters, which can usually be constrained only if measured vibrational frequencies of isotopically substituted and unsubstituted complexes are available. It is shown here for purposes of comparison with the much simpler MUBFF force-field.

[b] Skeletal (MX$_6$) frequencies, force-field calculations assume that each H$_2$O behaves like a point mass (i.e. like a single atom).

References: SiCl$_4$, Mohan and Müller (1972); SnCl$_4$, Königer and Müller (1975); RuO$_4$, McDowell et al. (1972); SF$_6$, Thakur (1971) and Brunet and Perez (1969); [SnCl$_6$]$^{2-}$ and [PdCl$_6$]$^{2-}$, Müller et al. (1975), Wharf and Shriver (1969), Debeau and Polet (1969), Woodward and Anderson (1957); [Cr(H$_2$O)$_6$]$^{3+}$, Best, Armstrong, and Beattie (1980); [Fe(H$_2$O)$_6$]$^{3+}$, Best, Beattie, and Armstrong (1984).

Table 2.2. Vibrational frequencies of iron-bearing molecules and complexes. As in Table 1, only the metal-isotope sensitive, triply-degenerate asymmetric stretching (v_3) and bending (v_4) modes are tabulated. All other vibrational mode symmetries should be unaffected by iron-isotope substitution. For each complex, a MUBFF is least-squares fit to all of the observed skeletal vibrational frequencies. The MUBFF is then used to calculate the ratio of the vibrational frequency of a ^{56}Fe-containing complex to the frequency to an ^{54}Fe-substituted complex. This ratio is reported in columns 3 and 5. Reduced partition functions are calculated assuming that ^{56}Fe-bearing complexes vibrate at the frequencies reported in columns 1 and 3.

Complex	Measured v_3 (cm^{-1})	Calculated $^{56}v_3/^{54}v_3$	Measured v_4 (cm^{-1})	Calculated $^{56}v_4/^{54}v_4$	Ref.
$[Fe^{III}Cl_4]^-$	384	0.9918	127	0.9951	1, 2
$[Fe^{II}Cl_4]^{2-}$	286	0.9923	119	0.9946	1
$[Fe^{III}Br_4]^-$	300	0.9880	94	0.9966	3
$[Fe^{III}Cl_6]^{3-}$	248	0.9936	184	0.9921	4
$[Fe^{II}(H_2O)_6]^{2+}$	389	0.9943	195*	0.9937	5, 6
$[Fe^{III}(H_2O)_6]^{3+}$	505	0.9937	304	0.9943	7

References: 1, Avery, Burbridge, and Goodgame (1968); 2, Murata and Irish (1988); 3, Thiele, Honert, and Rotter (1984); 4, Shamir (1991); 5, Nakagawa and Shimanouchi (1964); 6, Jenkins and Lewis (1981); 7, Best, Armstrong, and Beattie (1980).

*Estimated from the force-field of Nakagawa and Shimanouchi (1964) and prediction of Halley and Hautman (1987).

Table 2.3. Iron-isotope sensitive (symmetry F_{1u}) vibrational frequencies for hexacyano complexes. A value of 90 cm^{-1} was chosen for the frequency of ν_9 based on typical force-field predictions.

Complex	ν_6 (cm^{-1})	$^{56}\nu_6/^{54}\nu_6$	ν_7 (cm^{-1})	$^{56}\nu_7/^{54}\nu_7$	ν_8 (cm^{-1})	$^{56}\nu_8/^{54}\nu_8$	ν_9 (cm^{-1})	$^{56}\nu_9/^{54}\nu_9$	Ref.
$[Fe^{II}(CN)_6]^{4-}$	2044	0.99998	586	0.9916±0.0013	414	0.9976±0.0018	90	0.9974	7, 8
$[Fe^{III}(CN)_6]^{3-}$	2122	0.99998*	514	0.9916*	385	0.9976*	90	0.9974*	7, 9,10

*Frequency ratios($^{56}\nu_n/^{54}\nu_n$) for $[Fe^{III}(CN)_6]^{3-}$ are assumed to be the same as are calculated for $[Fe^{II}(CN)_6]^{4-}$. See Appendix for discussion.

References. 7, Nakagawa and Shimanouchi (1962); 8, Hipps et al. (1984); 9, Sievertsen et al. (1995); 10, Jones et al. (1974).

45

Table 2.4. Reduced partition function ratios $1000 \cdot \ln(\beta_{56\text{-}54})$ for ^{56}Fe - ^{54}Fe exchange at various temperatures. Linear interpolation between the reported temperatures will reproduce the curves shown in Fig. 1 to within 0.1 per mil. Results for $[Fe^{III}(H_2O)_3Cl_3]^0$ and $[Fe^{III}(H_2O)_4Cl_2]^+$ (#1) are weighted averages of model results for $[Fe^{III}(H_2O)_6]^{3+}$ and $[Fe^{III}Cl_6]^{3-}$; result #2 for $[Fe^{III}(H_2O)_4Cl_2]^+$ is obtained directly from calculated and observed vibrational frequencies for this complex.

Complex	0 °C	25 °C	100 °C	200 °C	300 °C
$[Fe^{II}(CN)_6]^{4-}$	20.6	17.6	11.7	7.5	5.2
$[Fe^{III}(CN)_6]^{3-}$	16.5	14.1	9.3	5.9	4.1
$[Fe^{III}(H_2O)_6]^{3+}$	13.6	11.6	7.6	4.8	3.3
$[Fe^{III}(H_2O)_4Cl_2]^+$ #1	10.6	9.0	5.9	3.7	2.6
$[Fe^{III}(H_2O)_4Cl_2]^+$ #2	10.0	8.5	5.5	3.5	2.4
$[Fe^{III}(H_2O)_3Cl_3]^0$	9.1	7.7	5.0	3.2	2.2
$[Fe^{III}Cl_4]^-$	8.5	7.2	4.7	2.9	2.0
$[Fe^{III}Br_4]^-$	7.6	6.4	4.1	2.6	1.8
$[Fe^{II}(H_2O)_6]^{2+}$	7.3	6.2	4.0	2.5	1.7
α-Fe Metal	6.3	5.3	3.4	2.1	1.5
$[Fe^{II}Cl_4]^{2-}$	4.8	4.0	2.6	1.6	1.1
$[Fe^{III}Cl_6]^{3-}$	4.6	3.8	2.5	1.5	1.1

Figure 2.1. Calculated reduced partition function ratios for ^{56}Fe-^{54}Fe exchange [$1000 \cdot \ln(\beta_{56\text{-}54})$] from 273 - 573 K (0 - 300ºC).

47
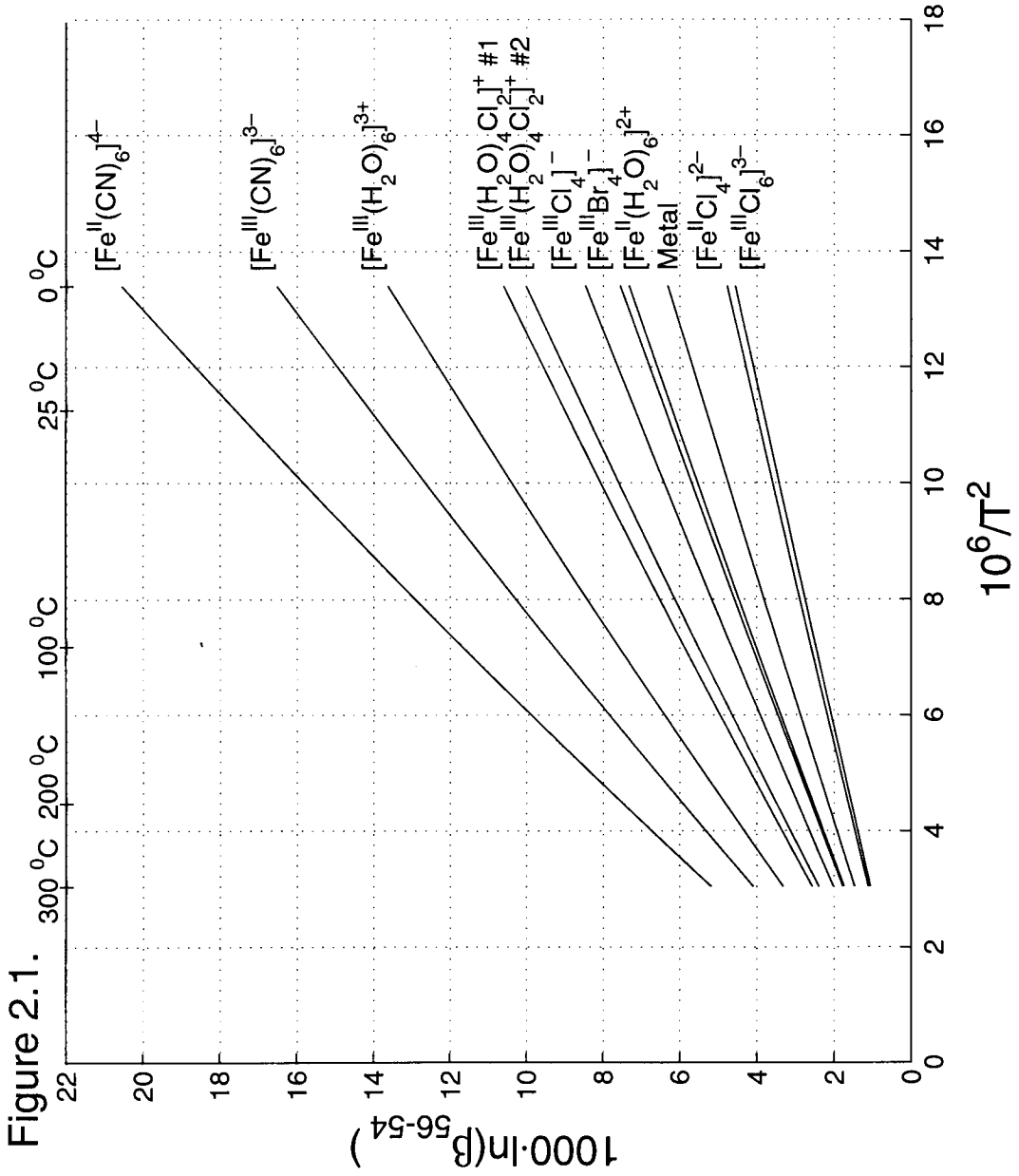
Figure 2.1.

Figure 2.2 Calculated reduced partition function ratios for ^{57}Fe-^{54}Fe exchange (solid

lines) compared with the Mössbauer spectroscopy-based models (dashed) of (POLYAKOV,

1997). Each $1000 \cdot \ln(\beta_{57-54})$ is almost exactly 1.5 times as large as the corresponding

$1000 \cdot \ln(\beta_{56-54})$ on Figure 2.1.
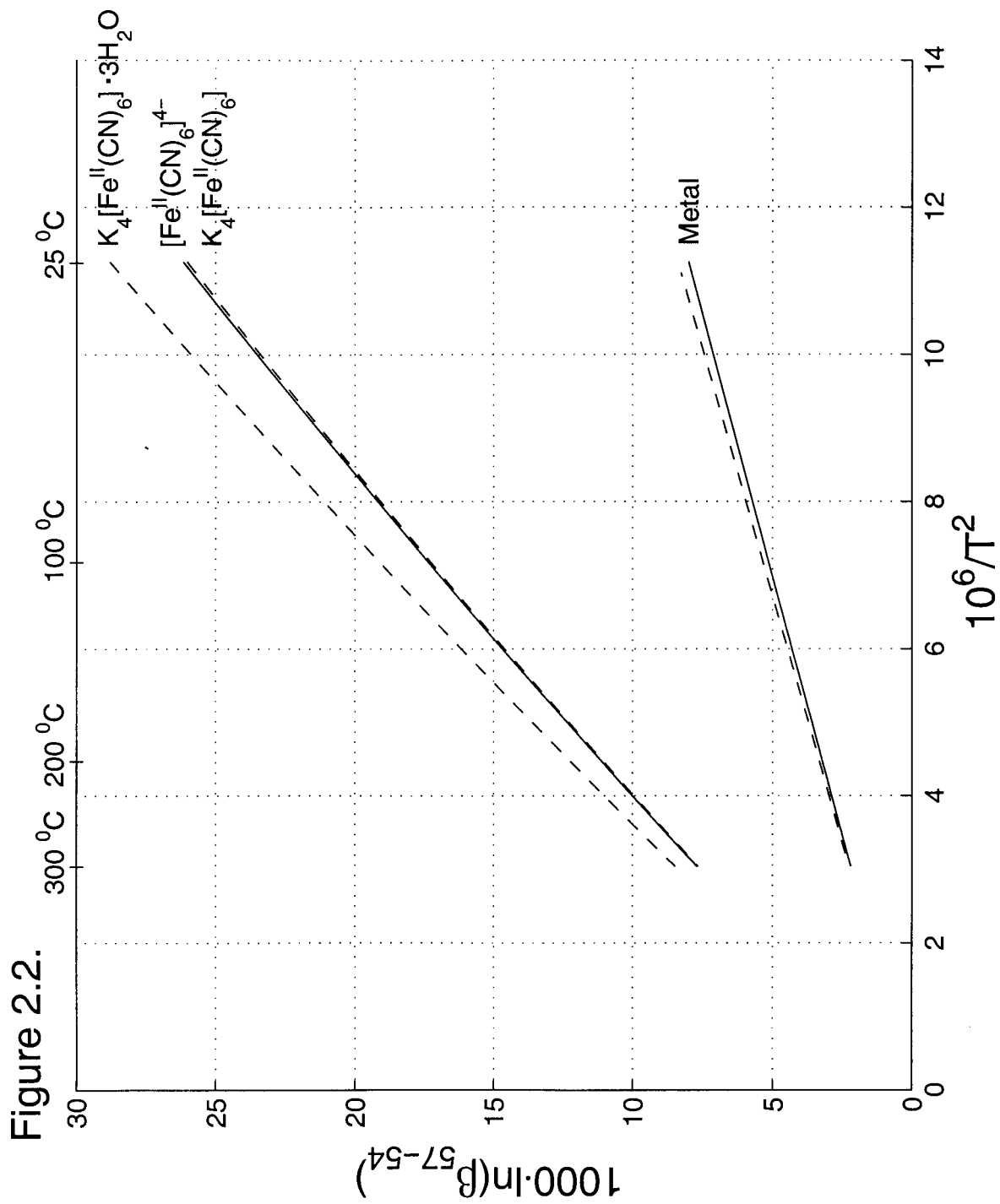
Figure 2.2.

Figure 2.3. Correlations between calculated reduced partition function ratios and spectroscopic and chemical properties. a) Asymmetric stretch (v_3) frequency vs. $1000 \cdot \ln(\beta_{56-54})$ for halogeno and aquo complexes in Table 2.2. Tetrahedral (FeX_4) complexes are shown as gray squares, octahedral complexes are shown as filled circles. b) Variation in calculated $1000 \cdot \ln(\beta_{56-54})$ with increasing covalent bond strength of the ligand. Ligands are arranged according to the spectrochemical series of increasing Δ_0, a measure of the d-orbital splitting of the metal-ligand bond (COTTON and WILKINSON, 1988). Large Δ_0 indicates strongly covalent metal-ligand bonding. The arrangement is schematic and not to scale. Ferric (Fe^{III}-bearing) complexes are indicated with filled diamonds, ferrous (Fe^{II}-bearing) complexes are indicated with open diamonds.

Figure 2.3.a
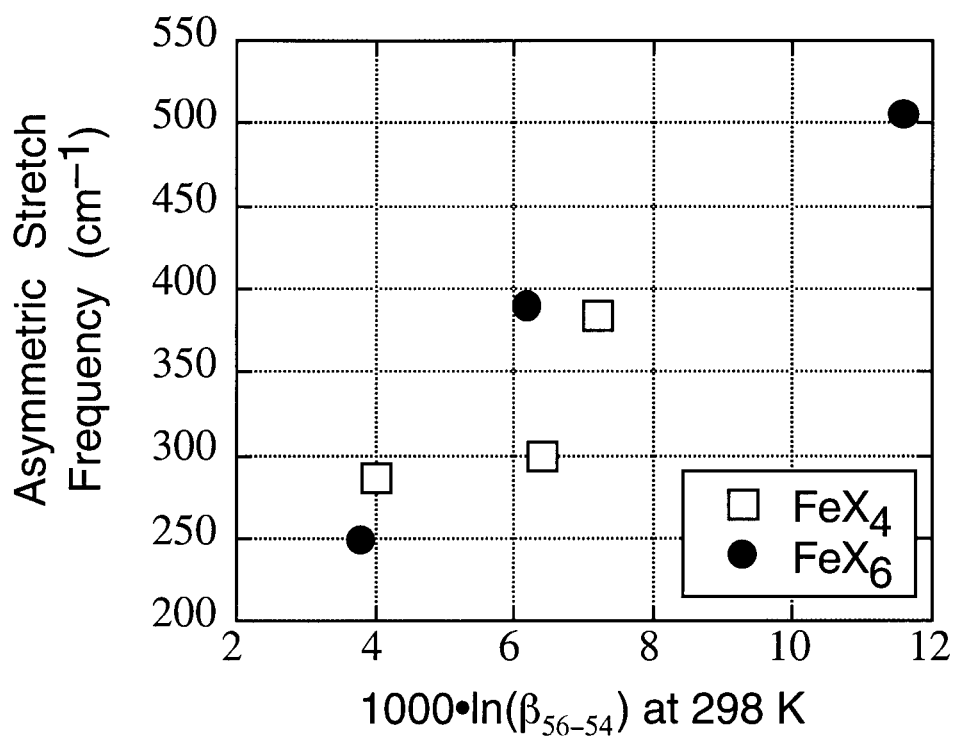
Figure 2.3.b
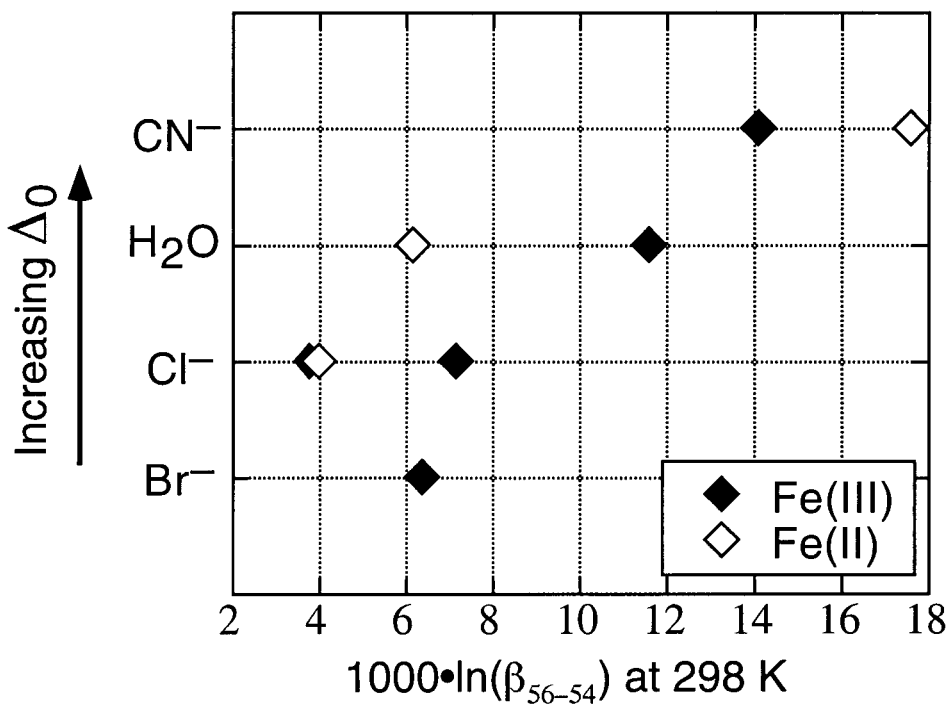
Chapter 3. Theoretical estimates of equilibrium chlorine-isotope fractionations

Equilibrium chlorine-isotope ($^{37}Cl/^{35}Cl$) fractionations have been determined using published vibrational spectra and force-field modeling to calculate reduced partition function ratios for Cl-isotope exchange. *Ab initio* force fields (calculated at the HF/6-31G* level) are used to estimate unknown vibrational frequencies of ^{37}Cl-bearing molecules, whereas crystalline phases are modeled using published lattice-dynamics models. Calculated fractionations are principally controlled by the oxidation state of Cl and its bond-partners. Molecular mass (or the absence of C-H bonds) also appears to play a role in determining relative fractionations among simple Cl-bearing organic species. Molecules and complexes with oxidized Cl (i.e., Cl^0, Cl^{+1}, etc.) will concentrate ^{37}Cl relative to chlorides (substances with Cl^-). At 298K, ClO_2 (containing Cl^{4+}) and $[ClO_4]^-$ (containing Cl^{7+}) will concentrate ^{37}Cl relative to chlorides by as much as 27‰ and 73‰, respectively, in rough agreement with earlier calculations (RICHET et al., 1977; UREY, 1947). Among chlorides, heavy chlorine will be concentrated in substances where Cl is bonded to +2 cations (i.e., $FeCl_2$, $MnCl_2$, micas and amphiboles) relative to substances where Cl is bonded to +1 cations (like NaCl) by ~2-3‰ at 298 K; organic molecules with C-Cl bonds will be even richer in ^{37}Cl (~5-9‰ at 298 K). The experiments of EGGENKAMP et al. (1995), in combination with our results, provide an estimate for Cl-isotope partitioning in brines, and suggest that silicates (to the extent that their Cl atoms are associated with nearest-neighbor +2 cations analogous with $FeCl_2$ and $MnCl_2$) will have higher $^{37}Cl/^{35}Cl$ ratios than coexisting brine (by ~2-3 ‰ at room temperature). Calculated fractionations between HCl and Cl_2, and between brines and such alteration minerals, are in qualitative agreement with both experimental results and systematics

observed in natural samples. Our results suggest that Cl-bearing organic molecules will have markedly higher $^{37}Cl/^{35}Cl$ ratios (by 5.8 ‰ to 8.5 ‰ at 295 K) than coexisting aqueous solutions at equilibrium. Predicted fractionations are consistent with the presence of an isotopically heavy reservoir of HCl that is in exchange equilibrium with Cl^-_{Aq} in large marine aerosols, as inferred by VOLPE et al. (1998).

3.1. Introduction

The purpose of this study is to provide estimates of equilibrium chlorine-isotope fractionations among a variety of geochemically interesting species. Substances studied include crystalline alkali-chloride salts, $FeCl_2$, and $MnCl_2$, in addition to gas-phase molecules and dissolved species. Atlhough chlorine was one of the first isotopic systems to be investigated theoretically (UREY, 1947; UREY and GREIFF, 1935), major gaps still exist in our understanding of chlorine-isotope partitioning in minerals, solutions, and organic molecules. Improved knowledge of equilibrium chlorine-isotope partitioning behavior should lead to greater progress in understanding the planetary chlorine cycle, groundwater processes, atmospheric chemistry, and the sources and fate of chlorine-containing pollutants.

Chlorine has two stable isotopes (^{35}Cl and ^{37}Cl), with $^{37}Cl/^{35}Cl \approx 0.320$, (PARRINGTON et al., 1996). Chlorine isotope ratios have been measured by both thermal-ionization and gas-source mass spectrometry (LONG et al., 1993; XIAO and ZHANG, 1992), and small variations have been detected in natural terrestrial samples. These variations are reported in terms of $\delta^{37}Cl_X = 10^3 \cdot (R_X/R_{standard} - 1)$, where R_X and $R_{standard}$ are the $^{37}Cl/^{35}Cl$ ratios in substance X and seawater, respectively. The observed terrestrial variation in $\delta^{37}Cl$ is approximately +7‰ to –8‰ (MAGENHEIM et al., 1995; RANSOM et

al., 1995), although larger deviations have been reported, (VENGOSH et al., 1989). The highest $^{37}Cl/^{35}Cl$ ratios are found in MORBs and Cl-bearing silicates (MAGENHEIM et al., 1995), while the lowest ratios are found in pore waters from the Nankai subduction zone (RANSOM et al., 1995). Groundwaters, evaporites, and organo-chloride pollutants also show significant deviations from the seawater ratio (JENDRZEJEWSKI et al., 2001; KAUFMANN et al., 1984).

Naturally formed chloride minerals, such as halite (NaCl), sylvite (KCl), and chloride-bearing silicates, have been extensively studied (e.g., EASTOE et al., 1999; EGGENKAMP et al., 1995; MAGENHEIM et al., 1995). Experimental studies have been conducted to determine equilibrium chlorine-isotope fractionations between halite, sylvite, bischofite ($MgCl_2 \cdot 6H_2O$), and their saturated aqueous solutions at ~22°C (EGGENKAMP et al., 1995; HOERING and PARKER, 1961). No equivalent attempts have yet been carried out for Cl^- bearing silicates.

Equilibrium stable isotope fractionations arise mainly from small differences in the vibrational energies of isotopically light and heavy substances (RICHET et al., 1977; UREY, 1947). Isotopically heavy substances vibrate at lower frequencies than their isotopically lighter equivalents, causing their vibrational energy to be slightly lower; the energy decrease caused by isotopic substitution varies from one substance to another, and is generally largest in strongly bonded substances. This variability means that there is a small energy change associated with isotopic exchange between two different substances, causing unequal partitioning of the isotopes between those substances when they are at equilibrium. Isotope partitioning in a substance is typically expressed in terms of a β-factor (i.e., β_{37-35} for ^{37}Cl-^{35}Cl exchange), defined as the ratio at equilibrium of the

isotope ratio of the substance of interest to the isotope ratio of dissociated atoms. β is equivalent to the factor $(s/s')f$ as defined by BIGELEISEN and MAYER (1947). It is convenient to report results as reduced partition function ratios (i.e., $1000 \cdot \ln\beta$), because

$$1000 \cdot \ln(\beta_{37\text{-}35}[X]) - 1000 \cdot \ln(\beta_{37\text{-}35}[Y]) \approx \delta^{37}Cl_X - \delta^{37}Cl_Y \text{ at equilibrium.}$$

3.2. Methods

3.2.1. Theory

Equilibrium chlorine-isotope fractionation factors are calculated using the standard thermodynamic, quantum mechanical approach, (i.e., UREY, 1947, eq. 4'). In general, we have chosen not to consider fractionation effects arising from vibrational anharmonicity and rotation. This is done for the sake of consistency, because (1) anharmonic parameters are only known for a few of the gas-phase molecules studied here, and (2) rotational quanta are so small that they have negligible effects on equilibrium isotope partitioning at the temperatures of interest here. A good example is HCl, which has a relatively large anharmonicity of ~2% and by far the largest rotational quanta of the molecules studied here. Our harmonic, vibration-only model for chlorine isotope partitioning in HCl gives results within 0.3‰ of the model of RICHET et al. (1977) from 0°C to 1000°C, even though the RICHET et al. (1977) model takes account of quantized rotations and anharmonicity.

Excellent spectroscopic data are available for many chlorine-containing molecules, dissolved species, and a handful of minerals and crystalline compounds. Gas-phase and matrix-isolation spectra of small molecules typically resolve frequencies of both the ^{35}Cl-endmember composition and one or more ^{37}Cl-containing isotopomers, greatly

facilitating the calculation of reduced partition function ratios. For most species, however, available spectroscopic data are incomplete, and it is necessary to calculate some or all of the vibrational frequencies of the ^{37}Cl-bearing form.

In the case of a simple molecule like Cl_2, it is a straightforward exercise to calculate the vibrational frequencies of $^{35}Cl^{37}Cl$ or $^{37}Cl_2$ from the observed frequency for $^{35}Cl_2$. For more complex molecules and condensed phases, however, it is usually necessary to create a model of the forces acting on each atom. In a previous paper (SCHAUBLE et al., 2001) we used a simple Urey-Bradley force field fitted to the known frequencies of each molecular complex. This procedure seems to work well for small, highly symmetric molecules and complexes where the number of independent force-field parameters is smaller than the number of observed frequencies. For more complex molecules, the simple force-field approach becomes cumbersome and less accurate.

3.2.2. Modeling Molecules

An alternative approach for molecules is to use *ab initio* methods to determine the force field. *Ab initio* force fields have the advantage that the calculated molecular structures and vibrational frequencies are not derived from observed structures and vibrational frequencies, so the suitability of the *ab initio* model can be independently verified by comparing it to experimental evidence. We use *ab initio* force fields for all molecules in this study for which isotopically substituted vibrational frequencies have not been measured or are incomplete. Harmonic molecular force fields are calculated at the Hartree-Fock level using the 6-31G(d) basis set (hereafter abbreviated HF/6-31G*). Calculations were performed using the Macintosh version (Brett Bode, *http://www.msg.ameslab.gov/GAMESS/dist.mac.shtml*) of the GAMESS (US) quantum

chemistry package (SCHMIDT et al., 1993). Geometry optimizations used symmetry constraints appropriate to each molecule, and atomic positions in each molecule were optimized until the residual forces on each atom were less than 10^{-5} hartree/bohr ($\approx 8.24 \times 10^{-13}$ Newtons). Vibrational frequencies were calculated at the optimized geometries.

It is well known (POPLE et al., 1993; SCOTT and RADOM, 1996; WONG, 1996) that *ab initio* force fields tend to make systematic errors in predicting vibrational frequencies. At the HF/6-31G* level, frequencies are typically overestimated by about 12%, with both high- and low-frequency vibrations off by roughly the same scale factor (SCOTT and RADOM, 1996). In cases where the *ab initio* molecular structure is close to the observed structure (angles within 1-2°, bond lengths within ~0.02 Å), and where calculated vibrational frequencies are proportional to the observed frequencies, the ratios of frequencies of isotopic molecules should be accurately predicted. However, we relaxed the structural criteria slightly for CCl_3F and the ethylene-family molecules, where the calculated C-F and C=C bond lengths were off by 0.03 to 0.04 Å. The accuracy of the *ab initio* force-field calculations can be seen in Table 3.1, which compares observed, *ab initio*, and empirical force-field estimates of ^{35}Cl-^{37}Cl frequency shifts in a variety of molecules (including some where the *ab initio* model gives a poor fit to the observed structure). The HF/6-31G* models accurately predict the frequency shifts in isotopically substituted molecules, reproducing observed $^{37}\nu/^{35}\nu$ ratios to within ~0.0005. Fifteen of the 27 ratios are reproduced within 0.0002, and the mean deviation is 0.00024. This level of accuracy corresponds to a difference of ~0.2 cm^{-1} in the isotopic shift of a 500 cm^{-1} vibration, and it is often difficult to distinguish errors in the model force field from

uncertainties in the measured shifts. Observed spectra of isotopically substituted species are complete for a few interesting molecules ($[ClO_4]^-$, CCl_4, and $OClO$), and for these it will be possible to directly compare empirical- and *ab initio*-based fractionation models. For chlorine monoxide (Cl_2O) and chlorine nitrate ($ClONO_2$), *ab initio* modeling at the HF/6-31G* level gives grossly erroneous vibrational frequencies (off by > 30 %) and/or structures (one or more bond lengths off by more than 0.05 Å). For these molecules, we use both measured shifts and the shifts calculated with published empirical or high-level *ab initio* force fields, and/or shifts calculated with the Redlich-Teller product rule (NAKAMOTO, 1997). In the remaining cases, shifts are determined by multiplying the ratios of frequencies in substituted and unsubstituted molecules calculated at the HF/6-31G* level by the observed frequencies for the ^{35}Cl-endmember compositions.

Each calculated reduced partition function ratio is calculated for an exchange reaction placing a single ^{37}Cl atom into a ^{35}Cl-endmember molecule. In nature, this is the most common exchange reaction for molecules containing 1 to 4 chlorine atoms, given the terrestrial abundance of ^{37}Cl and ^{35}Cl. Test calculations on Cl_2 and C_2Cl_4 suggest that the reduced partition function ratios calculated in this fashion are within ~0.04 ‰ of all other possible 1-atom exchange reactions over the temperature range of interest. If it were necessary to use a low-quality *ab initio* model, complete substitution of ^{37}Cl for ^{35}Cl might help mitigate errors, because the full symmetry of the molecule would then be preserved. Vibrational frequencies and calculated shifts for ^{37}Cl-substituted molecules are listed in Table 3.2.

3.2.3. Modeling Crystals.

Unlike molecules, the vibrational spectra of most solids cannot be adequately measured using standard infrared and Raman spectroscopy. The technique of choice, inelastic neutron scattering, has only been rigorously applied to a handful of minerals. Luckily, several important chlorides have been studied this way. These include halite (NaCl) (NILSSON, 1979; RAUNIO et al., 1969; SCHMUNK and WINDER, 1970), sylvite (KCl) (RAUNIO and ALMQUIST, 1969), RbCl (RAUNIO and ROLANDSON, 1970b), $MnCl_2$ (ESCRIBE et al., 1980) and $FeCl_2$ (YELON et al., 1974). Phonon spectra of isotopically substituted chlorides have not been measured, nor have those of chlorine-bearing silicates, such as amphiboles, micas, and clays.

For the crystals with measured phonon spectra, it is necessary to create a lattice-dynamical model to predict unknown frequencies. Many such models have been proposed (i.e., RAUNIO and ROLANDSON, 1970a; GAO et al., 1999; SCHMUNK and WINDER, 1970). Long-range Coulomb forces and short-range bond forces are typically treated separately in these models, and the best of them (called shell models) take account of the mechanical and electrical polarizability of ions in the lattice. Models are typically constrained using measured phonon spectra and additional information from elastic properties and/or dielectric constants.

$FeCl_2$ and $MnCl_2$ are important because they are probably the best available analogues for chlorine in silicates. Chlorine is incorporated into the hydroxyl site in both amphiboles and micas (VOLFINGER et al., 1985), and in both mineral types, the hydroxyl site is coordinated by three M^{2+} cations that are themselves in six-fold coordination. Structural refinements and compositional evidence suggest that Cl^- is strongly associated

with Fe^{2+} in these minerals (MAKINO and TOMITA, 1993; OBERTI et al., 1993; VOLFINGER et al., 1985), with a mean M^{2+}-Cl^- nearest-neighbor distance of ~2.46Å. Chlorine in $FeCl_2$ has a local coordination environment (VETTIER and YELON, 1975) that is very similar to an amphibole or mica with Fe^{2+}-Cl^- clustering (MAKINO and TOMITA, 1993; OBERTI et al., 1993). Each chlorine atom in $FeCl_2$ is bonded to three Fe^{2+} ions, with an Fe-Cl bond distance of ~2.50 Å. Thus, $FeCl_2$ should be a reasonable analogue for determining the chlorine-isotope fractionation behavior of silicates. $MnCl_2$ has the same basic structure and is much better studied spectroscopically, so it can help to confirm the $FeCl_2$ result. The best lattice-dynamics models available for both $FeCl_2$ and $MnCl_2$ are shell models similar to the ones developed for the alkali-halides (BENEDEK and FREY, 1980). Simpler lattice dynamics models for these substances (PASTERNAK, 1976; ESCRIBE et al., 1980) have also been published. In the present study, all of these models were used to calculate reduced partition function ratios, in order to get some idea of what effect different modeling schemes have on the outcome.

In reproducing published lattice-dynamics models, it was typically necessary to convert force-field parameters from their original form into a form that available lattice-dynamics software could understand. We found small differences between the frequencies we calculated and those reported by the original authors. For the most part the discrepancies are very small, on the order of 1-2%, and it is likely that these differences arise from the conversion process, or possibly from slight differences in the physical constants and computational techniques used. We found it helpful to re-optimize these models to the measured frequencies for each substance. Most of the models were found to rapidly converge with only modest changes in the converted parameters; and

residual errors for the reoptimized models are similar to the errors reported for the

original models. Differences in calculated reduced partition function ratios between re-

optimized and unreoptimized models are modest, 0.3‰ or less at 273 K. Furthermore,

reoptimization substantially reduced the scatter between different models for a given

crystal. The three NaCl models developed in RAUNIO and ROLANDSON (1970a) are

exceptions. There are large discrepancies between the observed and calculated

frequencies using these three models, and it even appears that Na-Na and Cl-Cl

interaction terms were switched for two of these models. After re-optimization, however,

the models predict reduced partition function ratios that are very similar those based on

the other lattice dynamics models for NaCl, even those that were reoptimized to a

different set of measured frequencies. The models were all optimized assuming that the

atomic mass of chlorine is 35.453 amu.

All lattice-dynamics calculations are made using GULP, the General Utility

Lattice Program (GALE, 1997). Reduced partition function ratios are calculated from the

Helmholtz free energies of ^{35}Cl- and ^{37}Cl-endmember compositions using eqn. 15 of

Kieffer (1982). In order to determine the Helmholtz free energy of each model crystal it

is necessary to integrate phonon frequencies across the entire volume of the Brillouin

zone, representing all possible phonon wave vectors in that crystal. This is done

numerically by sampling discrete, symmetrically distinct wave vectors in the Brillouin

zone. To make sure that the numerical integration was not affecting the calculated

properties, the number of sampling points was varied from 1 to ~1000. It was found that

the calculated change in the Helmholtz free energy due to isotope substitution converged

very rapidly as the number of sampling points increased, varying by no more than $2*10^{-3}$

J/mol for runs with 20 or more sampling points. The resulting error in a calculated

reduced partition function ratio is ~0.001 ‰ at 298 K, indicating that numerical

integration is not a significant source of uncertainty. Elcombe and Hulston (1975) report

a similar rate of convergence in calculating sulfur isotope fractionations between

sphalerite (ZnS) and galena (PbS). For the present study, roughly 150 wave vectors were

sampled in calculating each reduced partition function ratio.

3.3. Results

3.3.1. Calculated Fractionations

Calculated reduced partition function ratios for ^{37}Cl-^{35}Cl exchange from 273 K (0°C)

to at least 573 K (300°C) are shown in Figures 3.1-3.4 and Tables 3.3 and 3.4. Most

calculated reduced partition function ratios are approximately proportional to $1/T^2$ (T in

Kelvin) over the temperature range considered. The reduced partition function ratio

calculated for HCl behaves differently, however, because its vibrational frequency is so

high. Calculated $1000 \cdot \ln(\beta_{37-35})$'s at 298 K (25°C) range from ~2.3 per mil for RbCl to 75

per mil for $[ClO_4]^-$, a range comparable to that observed in the sulfur isotope system. The

three Cl-positions in trichloroethylene (C_2HCl_3) are predicted to have different affinities

for ^{37}Cl. At equilibrium and 298 K, the Cl closest to the H-atom in this molecule will be

~1‰ lighter than the Cl farthest from the H atom. The calculations assumed no internal

rotation about the C=C double bond, which may not be accurate at higher temperatures.

Equilibrium ^{37}Cl-^{35}Cl fractionations for a few molecules (HCl, Cl_2, ClO_2,

and$[ClO_4]^-$) have previously been calculated (Urey, 1947; Richet et al., 1977), and in

general our results agree with earlier work. For HCl and Cl_2, disagreement in

$1000 \cdot \ln(\beta_{37-35})$ is ≤ 0.3 ‰ and ≤ 0.1 ‰, respectively, over the range from 0°C to 1000°C. This good agreement is hardly surprising, because the vibrational spectra for these two molecules were accurately measured many decades ago. In addition, vibrational frequencies for ^{37}Cl-bearing diatomic molecules are easily calculated without any need for a force-field model, and there is good agreement been the calculated and observed frequencies. For ClO_2 and the $[ClO_4]^-$ anion, our calculated $1000 \cdot \ln(\beta_{37-35})$ values are ~2.2‰ and 8‰ lower, respectively, than the values reported by (UREY, 1947) at 0°C. The ν_2 vibrational frequency in ClO_2 is now known to be much lower than was thought in 1947 (448 cm^{-1} vs. 529 cm^{-1}), and this difference is largely responsible for the change in calculated $1000 \cdot \ln(\beta_{37-35}[ClO_2])$. For $[ClO_4]^-$, vibrational frequencies of the $[^{35}ClO_4]^-$ endmember used by UREY (1947) are very similar to the frequencies we used. The difference in the calculated reduced partition function ratios is attributable almost entirely to differences in the calculated frequencies for $[^{37}ClO_4]^-$. Urey's valence force-field model predicts a large shift (16.7 cm^{-1}, $^{37}\nu/^{35}\nu \approx 0.9849$) in the high-frequency ν_3 vibration upon substitution of ^{37}Cl. Measured spectra show a smaller shift of 13-15 cm^{-1} (CHABANEL et al., 1996; DECIUS and MURHAMMER, 1980), consistent with our calculated shift of 14.1 cm^{-1}. Present calculations for both ClO_2 and $[ClO_4]^-$, therefore, are probably more accurate than those reported previously.

3.3.2. Accuracy Estimates

Calculated reduced partition function ratios may be in error for several reasons: (1) uncertainty in the measured or (in the case of crystals) calculated vibrational frequencies for ^{35}Cl-endmember substances; (2) errors in the frequency shifts calculated for ^{37}Cl substitution; and (3) anharmonicity effects.

In general, the vibrational frequencies of ^{35}Cl end-member molecular species are known to a high degree of accuracy. Except for $[ClO_4]^-$, the studied species are all neutral and amenable to spectroscopic measurement in the gas phase and/or in noble-gas matrices. The fundamental vibrational frequencies for these species are reliable to within one or at most a few cm^{-1}. Propagated errors in the reduced partition function ratios for measurement uncertainties of this size are quite small, as random shifts of 2 cm^{-1} change $1000 \cdot ln(\beta_{37-35})$ by less than 0.2 ‰ over the temperature range of interest for all of the neutral molecules.

The perchlorate anion, $[ClO_4]^-$, does not lend itself to gas-phase measurements, and its geochemical relevance is as a solute species. The vibrational frequency of the v_3 mode of $[ClO_4]^-$ in solution varies over a range of ~25 cm^{-1} depending on the type of solution, while the v_4 mode varies over a range of ~10 cm^{-1} (CHABANEL et al., 1996). This suggests that $1000 \cdot ln(\beta_{37-35}[ClO_4]^-)$ could vary by several per mil, depending on the solution chemistry. Although that error is quite large relative to errors for gas-phase molecules, it is much smaller than the predicted fractionation between $[ClO_4]^-$ and other substances. Vibrational frequencies for neutral molecules may also change when they are dissolved, adsorbed, or are held at high pressure, and associated errors may be much larger than 0.1‰ under such circumstances. Experiments reported by HUANG et al. (1999) suggest that molecules in solution tend to concentrate ^{37}Cl relative to gas-phase molecules, with equilibrium vapor-liquid fractionations as large as 0.5‰ observed for trichloroethylene (C_2HCl_3).

For crystals, uncertainty in vibrational (phonon) frequencies of ^{35}Cl-endmember compositions may be a significant source of error. It is time-consuming to measure

vibrations with inelastic neutron scattering, and measurements are usually limited to wave-vectors along high-symmetry directions in the Brillouin zone. Thermodynamic properties, however, are largely determined by off-symmetry wave-vectors, and lattice dynamics models can be used to make the necessary extrapolation. The reoptimized lattice dynamics models for NaCl, KCl, and RbCl reproduce measured high-symmetry frequencies within ~1–2%, but for KCl and RbCl we don't know how well the rest of the vibrational spectrum is predicted. For NaCl, a large number of off-symmetry vibrational frequencies have been measured (NILSSON, 1979), and it is possible to compare those frequencies with model predictions. Surprisingly, measured off-symmetry frequencies turn out to be very close to the calculated frequencies, typically within 1–2%, suggesting (at least for NaCl) that the reoptimized lattice dynamics models are fairly accurate. Note that a uniform 1% shift in vibrational frequencies for NaCl would change the calculated $1000 \cdot \ln(\beta_{37-35}[\text{NaCl}])$ by ~0.08 ‰ at 0°C, and at higher temperatures the size of this error is approximately proportional to $1/T^2$. For KCl and RbCl, equivalent measurement errors would propagate to somewhat smaller errors of ~0.06 ‰ at 0°C.

Spectroscopic measurements on $FeCl_2$ and $MnCl_2$ are not as extensive as for the alkali halides, limiting the accuracy of calculated reduced partition function ratios for these divalent substances. In addition, the lattice dynamics models do not match measured frequencies as well. $MnCl_2$ is the better studied of the two, and frequencies calculated with the model of Benedek and Frey (1980) are generally within a few % of measured frequencies. However, frequencies are about 10% too high in one longitudinal optical (LO) branch of A_1 symmetry, and > 10% too high in the longitudinal acoustic

(LA) phonon branch in the Γ–K direction, and this could lead to errors as large as 0.7 ‰ in the predicted $1000 \cdot \ln(\beta_{37\text{-}35})$ at 0°C.

For crystalline solids, and molecules containing more than two atoms, the largest sources of error in our calculations probably come from uncertainties in the predicted frequencies for ^{37}Cl-bearing species. This problem is particularly acute for molecules in which two or more vibrations at moderate to low frequencies (0 to ~1000 cm^{-1}) have the same symmetry. Higher frequency vibrations are usually only slightly sensitive to Cl-isotope substitution, and are therefore less important. A large data set is available for ^{37}Cl-species that can be used to check the *ab initio* force-field models (Table 3.1). These comparisons suggest that *ab initio* modeling reproduces observed frequency shifts ($^{37}\nu/^{35}\nu$) to within about 0.0005 in most cases, in agreement with our earlier findings utilizing empirical force fields (SCHAUBLE et al., 2001).

For [ClO$_4$]$^-$, CCl$_4$, and OClO, it is possible to use measured frequencies for ^{37}Cl-bearing species to calculate $1000 \cdot \ln(\beta_{37\text{-}35})$, and thus directly estimate the effects of force-field errors. Measured shifts for [ClO$_4$]$^-$, CCl$_4$, and OClO give results that differ by 3.07, 0.32, and 0.13‰ at 25°C, respectively. If we perturb the calculated frequency shifts (for moderate-low frequency vibrations) for other molecules by a similar amount (0.0003-0.0005) in a way consistent with the Redlich-Teller product rule, the calculated values of $1000 \cdot \ln(\beta_{37\text{-}35})$ change by about 0.1 to 0.7 ‰ (at 298 K). The sensitivity of the calculated values of $1000 \cdot \ln(\beta_{37\text{-}35})$ to errors in calculated vibrational frequencies is greatest for higher frequency vibrations, particularly when vibrations of the same symmetry have very different frequencies (i.e., ν_3 vs. ν_4 in CCl$_4$). It is, unfortunately, not possible to give

a quantitative estimate of errors in calculated frequencies for ^{37}Cl-bearing crystals. However, the general agreement between several lattice-dynamics models (of varying complexity) for each crystalline chloride provides some assurance that the results are not grossly erroneous.

The calculations reported here assume that molecular and crystalline vibrations are harmonic, mostly out of necessity because anharmonic effects have not been quantified for many of the substances of interest. Resulting errors are probably small for the molecules we studied, at least over the temperature range of interest, but they may be significant for the chloride crystals. We estimate that typical molecular anharmonicities of ~1% will cause errors of 0.1 to 0.2 ‰ for most molecules. Larger errors of up to 0.5 ‰ and 2 ‰ may result for ClO_2 and $[ClO_4]^-$, respectively. In compiling molecular vibrational frequencies, we have used a number of data that have been "corrected" for anharmonicity using measured overtone- and combination-band frequencies. Zero-point energies should be more accurately approximated with corrected frequencies than by using the raw, measured fundamental frequencies; therefore, we have used the corrected frequencies when they are available.

In crystals, and particularly in halides like NaCl, anharmonicity typically causes vibrational frequencies to decrease with increasing temperature. The frequencies used to constrain the lattice-dynamics calculations for crystals were, for the most part, measured at very low temperatures (77-120 K). Measurements made at ~300 K in NaCl (RAUNIO et al., 1969; SCHMUNK and WINDER, 1970), KCl (TANAKA and HISANO, 1989; WAKAMURA, 1993), and RbCl (RAUNIO and ROLANDSON, 1970b) suggest that vibrational frequencies are typically ~ 2-5% lower at this temperature than at ~120 K. As a consequence, the

calculated values of $1000 \cdot \ln(\beta_{37-35})$ for NaCl, KCl, and RbCl are probably ~0.1 to 0.4‰ too high at room temperature. The estimated error of 0.1–0.4 ‰ may be reasonable over the entire temperature range of interest, because further reductions in vibrational frequencies at higher temperatures are counterbalanced by rapid decreases in absolute $1000 \cdot \ln(\beta_{37-35})$ values. There do not appear to be any major differences in the temperature dependence of phonon frequencies in the different alkali halides, so the effect is expected to be approximately the same for all of them. The same types of errors probably affect calculations for $FeCl_2$ and $MnCl_2$, but there is not enough information justify a quantitative error estimate.

Combining all three sources of error described above, it is possible to make a rough estimate of the total errors in calculated $1000 \cdot \ln(\beta_{37-35})$ values. For $[ClO_4]^-$, the total error amounts to approximately ±5 ‰ at 298 K. For the gas-phase molecules, OClO: ±1 ‰, HCl and Cl_2: ±0.3 ‰, other molecules: ±0.5 ‰ to 0.8 ‰. In general, errors are largest for molecules that tend to concentrate ^{37}Cl, and for molecules with three or more atoms. Because we cannot compare model and measured frequencies for ^{37}Cl-bearing crystals, the combined error estimates for crystals should be considered lower bounds on the true errors. Uncertainties in model frequencies of ^{35}Cl-dominated crystals and the lack of consideration of anharmonicity (T-dependence of vibrational frequencies) lead to errors of approximately +0.0 ‰/−0.5 ‰ for NaCl, KCl, and RbCl. Errors in model frequencies of $Fe^{35}Cl_2$ and $Mn^{35}Cl_2$ could cause errors as large as ±0.7 ‰ at 25°C. Errors are likely to be smaller when closely related species are compared (i.e., NaCl vs. RbCl) than they will be for chemically distinct species (i.e., $ClONO_2$ vs. $FeCl_2$).

3.4. Discussion

3.4.1. Factors Controlling Predicted Fractionations

Predicted reduced partition function ratios are determined from vibrational frequencies of Cl-bearing substances, and by the sensitivities of those vibrations to Cl-isotope substitution. Molecules and crystals with high-frequency, highly Cl-isotope sensitive vibrations will tend to concentrate ^{37}Cl. The tremendous range in the masses of bonding partners for Cl, however, means that there is a poor correlation between the frequency of Cl-X stretching vibrations and calculated values of $1000 \cdot \ln(\beta_{37-35})$. A good correlation is found between $1000 \cdot \ln(\beta_{37-35})$ and the oxidation state of chlorine (Fig. 3.5). Substances with oxidized chlorine (Cl^{+1}, Cl^{+2}, Cl^{+7}, etc.) will tend to be heavier than the crystals containing Cl^{-1}. For molecules with C-Cl bonds, covalent bonding makes assigning an oxidation state less clear-cut. These substances are similar to typical Cl^0 and Cl^{+1} molecules in their affinities for ^{37}Cl. Furthermore, the chlorine-bearing organic molecules studied are all similar to one another, spanning a total range of ~1.8 ‰ at room temperature. For metal chlorides, there is a strong effect exerted by the bond partner; crystals with M^{+1}-Cl bonds (i.e., NaCl, KCl, and RbCl) will tend to have low ^{37}Cl/^{35}Cl ratios when in equilibrium with crystals having M^{+2}-Cl bonds (FeCl$_2$, MnCl$_2$). At low temperatures, HCl follows this trend, but here the tiny mass of the H atom is a more important factor than its oxidation state. At high temperatures, where bond stiffness is most important, HCl is most similar to the chlorine-bearing organic molecules (with C-Cl bonds) in its affinity for ^{37}Cl. A similar bond-partner mass effect may control relative fractionations among the organic molecules, though here the relevant mass is the entire molecule, not just the nearest-neighbor atom. The heaviest molecules studied (i.e., C$_2$Cl$_4$,

CCl_4, CCl_3F) are predicted to concentrate ^{37}Cl relative to lighter, more H-rich molecules like CH_3Cl. C-Cl bonds are probably the least stiff bonds in a small organic molecule, so the C-atom and some of its other bond partners (even other Cl's) behave as a single quasi-coherent mass during C-Cl stretching vibrations. The heavier the effective counter-mass, the greater the sensitivity of the Cl-C stretching vibrations to Cl-isotope substitution, leading to a greater affinity for ^{37}Cl. A large countermass will also tend to reduce the Cl-C stretching frequency, which may explain the poor correlation between Cl-X stretch frequencies and $1000 \cdot \ln(\beta_{37-35})$ among Cl-bearing organic molecules. This counter-mass effect may also control internal fractionation in trichloroethylene (C_2HCl_3), with heavy Cl tending to be concentrated in the part of the molecule farthest from the light H atom.

3.4.2. Comparison with Experimental Results and Natural Samples

The best way to evaluate the accuracy of predicted fractionations is to compare them with high-quality experimental measurements. Estimated errors for calculated fractionations are large relative to the typical precision of a Cl-isotope measurement, so even if our predictions are correct, significant refinement should be possible through careful empirical studies.

Laboratory experiments have been carried out to characterize equilibrium Cl-isotope fractionations between a few substances. Hoering and Parker (1961) equilibrated Cl_2 and HCl at 296 K, measuring a fractionation of 3.8±0.4 ‰. At this temperature, our calculated fractionation between Cl_2 and HCl is 2.7±0.4 ‰, not quite in agreement within the reported errors. The same authors measured a fractionation of 0.9±0.3 ‰ between HCl and crystalline NH_4Cl at 473 K, which can be crudely compared with our predicted

fractionations of ~1.4 – 1.9 ‰ between HCl and NaCl at the same temperature.

Eggenkamp et al. (1995) measured fractionations between NaCl, KCl, and saturated

brines. At 295 K, NaCl is 0.3±0.1 ‰ heavier than the coexisting NaCl-saturated brine,

while KCl is 0.1±0.1 ‰ lighter than KCl-saturated brine. Our results predict that NaCl

will be ~0.8 ‰ heavier than coexisting KCl at this temperature. It is unclear difference

there might be in the isotopic behavior of a KCl-brines and NaCl-brines (both saturate at

roughly 6 mol/l), though it is reasonable to expect a general similarity if there is not much

direct ion pairing between solvated M^{+1} and Cl^-. If we assume that the two brines are

identical (at least with respect to Cl-isotope partitioning), the Eggenkamp et al. (1995)

result suggests a ~0.4 ‰ fractionation between crystalline NaCl and KCl, which is in

qualitative agreement with our theoretical calculation. Using the Eggenkamp et al. (1995)

results, we can estimate that $1000 \cdot \ln(\beta_{37\text{-}35}[\text{Brine}]) \approx 2.1$–$3.0$ at 295 K (22°C) for brines

where NaCl or KCl is the dominant solute.

Calculated fractionations can also be compared with the chlorine-isotope

systematics observed in natural samples. One result of great interest is the predicted

fractionation between NaCl- and KCl-saturated brines and the divalent-metal chlorides

$FeCl_2$ and $MnCl_2$. If $FeCl_2$ and $MnCl_2$ are good analogues for structurally bound Cl^- in

micas and amphiboles, our results suggest that, at equilibrium, these minerals will be

~2–3‰ heavier than their coexisting brines (at 22°C). This agrees qualitatively with the

observed systematics in hydrothermally altered oceanic crust (MAGENHEIM et al., 1995),

where Cl-bearing silicates have been found to be characteristically heavier than seawater,

particularly for low-temperature minerals like smectite. Subduction-zone pore waters,

which have strongly negative $\delta^{37}Cl$ relative to seawater (RANSOM et al., 1995), are also

consistent with preferential retention or fixation of ^{37}Cl in silicates. The bonding structure around dissolved Cl⁻ probably changes considerably as the temperature, pressure, and solute composition change, however, so it is not clear how to extrapolate our results for room-temperature NaCl- and KCl-saturated brines to other conditions of interest.

3.4.3. Chlorine/isotopes, Groundwater Pollution, and Atmospheric Chlorine Cycling

Several of the studied molecular species are important in studies of groundwater pollution and atmospheric chlorine cycles. It is not clear that equilibrium fractionations will be observed in these natural systems, because of the importance of biological activity, slow reaction kinetics, and photochemistry. However, understanding the equilibrium fractionations underlying chemical transformations in these systems may help in designing and interpreting experiments on both natural systems and laboratory analogues. In this section we briefly relate our results to the isotopic systematics that have been observed in these systems.

Our results suggest that chlorine-bearing organic molecules will concentrate ^{37}Cl relative to coexisting aqueous chloride or (at T ≤ 400°C) gas-phase HCl. This result is of interest because chlorine-isotope measurements are being evaluated as a way of monitoring the remediation of chlorinated organic pollutants in groundwater (HERATY et al., 1999; STURCHIO et al., 1998). In oxidizing groundwaters, it is thought that chlorinated organic molecules are destroyed via oxidation to inorganic species (i.e., $CH_2Cl_2 + ^3/_2 O_2 \rightarrow CO_2 + 2 Cl^-_{Aq} + 2 H^+_{Aq}$). Cl^-_{Aq} and HCl are both predicted to be isotopically light relative to coexisting organics like $CHCl_3$ and C_2HCl_3, with equilbrium fractionations of 4.1-5.8 ‰ between the studied organics and HCl, and 5.8-8.5 ‰ between the studied organics and brine. The predicted equilibrium fractionations are quite large relative to

observed fractionations. The largest measured fractionation, 3.8±0.3 ‰, is observed

during biologically mediated oxidation of CH_2Cl_2 (HERATY et al., 1999). Although we

have not directly calculated fractionations for the CH_2Cl_2 molecule, it is probably

intermediate between $CHCl_3$ and CH_3Cl, suggesting a fractionation of 6–7 ‰ between

CH_2Cl_2 and brine at 22°C. The empirical observations suggest that oxidation reactions in

the environment are not exhibiting equilibrium fractionation. Therefore, isotope

fractionations in these systems may be sensitive to the details of reaction pathways and

local biogeochemistry.

Chlorine-isotope reduced partition function ratios have been calculated for the

most abundant Cl-bearing atmospheric molecules (HCl, ClO, and $ClONO_2$), as well as a

number of other species that are of interest in particular atmospheric reactions (i.e., Cl_2,

$ClNO_2$). One potential application of these results is to the study of Cl-volatilization from

marine aerosols. VOLPE and SPIVACK (1994) and VOLPE et al. (1998) measured $\delta^{37}Cl$ and

solute compositions on suites of marine aerosol particles collected on Bermuda and in the

central equatorial Pacific. In the largest size-fractions among collected Pacific aerosols,

$\delta^{37}Cl$ decreases with increasing chlorine loss (as indicated by low Na/Cl ratios), and

VOLPE et al. (1998) suggest this is the result of rapid cycling of Cl between aerosols and a

gas-phase reservoir; they infer a 2.8-3.0 ‰ fractionation between the gas-phase reservoir

and the aerosol chloride. The calculated equilibrium fractionation between HCl and brine

is ~1.7-2.6 ‰ at 295 K, quite close to their inferred fractionation. This suggests that HCl

may indeed dominate a gas-phase reservoir that reaches exchange equilibrium with large

aerosols. VOLPE and SPIVACK (1994) suggest that the fractionation observed in aerosol

evaporation experiments (and in small natural aerosols), which goes in the opposite

direction than the fractionation observed in large aerosols, is probably fundamentally kinetic. This is consistent with our results, because neither HCl nor any other plausible Cl-bearing vapor species (except monoatomic Cl) will be ^{37}Cl-depleted relative to a saturated NaCl-brine.

3.5. Conclusions

Equilibrium chlorine-isotope (^{37}Cl/^{35}Cl) fractionations have been investigated by using published vibrational spectra and force-field modeling to calculate reduced partition function ratios for Cl-isotope exchange. Calculated fractionations are mainly controlled by the oxidation state of Cl and its bond partners. Molecular mass also appears to play a role in determining relative fractionations among simple Cl-bearing organic species. Molecules and complexes with oxidized Cl (i.e., Cl^{0}, Cl^{+1}, Cl^{+2}, etc.) will concentrate ^{37}Cl relative to chlorides (substances with Cl^{-}). Among chlorides, heavy chlorine will be concentrated in substances where Cl is bonded to +2 cations (i.e., FeCl$_2$, MnCl$_2$, micas and amphiboles) relative to substances where Cl is bonded to +1 cations (NaCl, KCl, and RbCl); organic molecules with C-Cl bonds will be heavier still. The experiments of EGGENKAMP et al. (1995), in combination with our results, suggest that silicates (to the extent they are analogous with FeCl$_2$ and MnCl$_2$) will have higher ^{37}Cl/^{35}Cl ratios than coexisting brine, by ~2–3 ‰ at room temperature. Calculated fractionations between HCl and Cl$_2$, and between brines and alteration minerals (mica and amphibole), are in qualitative agreement with experimental results and systematics observed in natural samples. Our results suggest that Cl-bearing organic molecules will have markedly higher ^{37}Cl/^{35}Cl ratios (by 5.8 ‰ to 8.5 ‰ at 295 K) than coexisting aqueous solutions at equilibrium. In addition, our results are consistent with the presence

of an isotopically heavy reservoir of HCl in exchange equilibrium with Cl^-_{Aq} in large marine aerosols, as inferred by VOLPE et al. (1998).

3.6. Bibliography

Abel B., Hamann H. H., Kachanov A. A., and Troe J. (1995) Intracavity laser absorption spectroscopy of HOCl overtones. I. The $3v_1+2v_2$ band and numbers of vibrational states. *J. Chem. Phys.* **104**(9), 3189-3197.

Benedek G. and Frey A. (1980) Lattice dynamics of layered transition-metal dihalides. *Physical Review B.* **21**, 2482-2498.

Bigeleisen J. and Mayer M. G. (1947) Calculation of equilibrium constants for isotopic exchange reactions. *J. chem. Phys.* **15**, 261-267.

Black G. M. and Law M. M. (2001) The general harmonic force field of methyl chloride. *Journal of Molecular Spectroscopy* **205**, 280-285.

Burkholder J. B., Hammer P. D., Howard C. J., Maki A. G., Thompson G., and Chackerian C. J. (1987) Infrared measurements of the ClO radical. *Journal of Molecular Spectroscopy* **124**, 139-161.

Castro J. B. and Anacona J. R. (1994) Normal-coordinate analysis and Coriolis coupling constants of ethylene type molecules, C_2X_4 (X = F,Cl, Br, I). *Journal of Molecular Structure* **304**, 273-278.

Chabanel M., Legoff D., and Touaj K. (1996) Aggregation of perchlorates in aprotic donor solvents Part 1. — lithium and sodium perchlorates. *J. Chem. Soc. Faraday Trans.* **92**, 4199-4205.

Clark R. J. H., Ellestad O. H., and Escribiano R. (1976) The vapour phase Raman spectra, Raman band contour analyses, Coriolis coupling constants, and force constants

for the molecules $F^{12}CH_3$, $F^{13}CH_3$, $H^{12}CCl_3$, and $H^{13}CCl_3$. *Molecular Physics* **31**, 65-81.

Clyne M. A. A. and Coxon J. A. (1970) The visible band absorption spectrum of chlorine. *Journal of Molecular Spectroscopy* **33**, 381-406.

Copley J. R. D., MacPherson R. W., and Timusk T. (1969) Lattice dynamics of potassium chloride. *Physical Review* **182**, 965-972.

Decius J. F. and Murhammer D. (1980) Absolute i.r. intensities, dipole derivatives, and vibrational charge parameters in the perchlorate anion. *Spectrochim. Acta* **36A**, 965-969.

Duxbury G. and McPheat R. (1995) High-resolution absorption spectrum of the v_2 band of nitryl chloride, $ClNO_2$, at 793 cm^{-1}. *Journal of Molecular Spectroscopy* **174**, 446-458.

Eastoe C. J., Long A., and Knauth L. P. (1999) Stable chlorine isotopes in the Palo Duro Basin, Texas: Evidence for preservation of Permian evaporite brines. *Geochimica et Cosmochimica Acta* **63**, 1375-1382.

Eggenkamp H. G. M., Kreulen R., and Van Groos A. F. K. (1995) Chlorine stable isotope fractionation in evaporites. *Geochimica et Cosmochimica Acta* **59**, 5169-5175.

Elcombe M. M. and Hulston J. R. (1975) Calculation of sulphur isotope fractionation between sphalerite and galena using lattice dynamics. *Earth and Planetary Science Letters* **28**, 172-180.

Escribe C., Bouillot J., and Ziebeck K. R. A. (1980) Lattice dynamics of $MnCl_2$. *J. Phys. C.: Solid State Phys.* **13**, 4053-4060.

Gale J. D. (1997) GULP - a computer program for the symmetry adapted simulation of solids. *J. Chem. Soc. Faraday Trans.* **93**, 629-637.

Heraty L. J., Fuller M. E., Huang L., Abrajano T. J., and Sturchio N. C. (1999) Isotopic fractionation of carbon and chlorine by microbial degradation of dichloromethane. *Organic Geochemistry* **30**, 793-799.

Hoering T. C. and Parker P. L. (1961) The geochemistry of the stable isotopes of chlorine. *Geochimica et Cosmochimica Acta* **23**, 186-199.

Huang L., Sturchio N. C., Abrajano T. J., Heraty L. J., and Holt B. D. (1999) Carbon and chlorine isotope fractionation of chlorinated aliphatic hydrocarbons by evaporation. *Organic Geochemistry* **30**, 777-785.

Jendrzejewski N., Eggenkamp H. G. M., and Coleman M. L. (2001) Characterisation of chlorinated hydrocarbons from chlorine and carbon isotopic compositions: scope of application to environmental problems. *Applied Geochemistry* **16**, 1021-1031.

Jones L. H., Swanson B. I., and Ekberg S. A. (1984) Isotope shifts and force field for carbon tetrachloride in a krypton matrix. *J. Phys. Chem.* **88**, 5560-5563.

Kaufmann R., Long A., Bentley H., and Davis S. (1984) Natural chlorine isotope variations. *Nature* **309**, 338-340.

Kieffer S. W. (1982) Thermodynamics and lattice vibrations of minerals: 5. Applications to phase equilibria, isotopic fractionation, and high-pressure thermodynamic properties. *Rev. Geophys. Space Phys.* **20**, 827-849.

King S. T. (1968) Infrared study of matrix-isolated chlorinated tetrahedral molecules. *J. Chem. Phys.* **49**, 1321-1330.

Kisiel Z. and Pszczólkowski L. (1996) Assignment and analysis of the mm-wave rotational spectrum of trichloroethylene: observation of a new, extended ^bR-band and an overview of high-J, R-type bands. *Journal of Molecular Spectroscopy* **178**, 125-137.

Long A., Eastoe C. J., Kaufmann R. S., Martin J. G., Wirt L., and Finley J. B. (1993) High-precision measurement of chlorine stable isotope ratios. *Geochimica et Cosmochimica Acta* **57**, 2907-2912.

Magenheim A. J., Spivack A. J., Michael P. J., and Gieskes J. M. (1995) Chlorine stable isotope composition of the oceanic crust: Implications for Earth's distribution of chlorine. *Earth and Planetary Science Letters* **131**, 427-432.

Makino K. and Tomita K. (1993) Effect of chlorine on the crystal structure of a chlorine-rich hastingsite. *Mineralogical Magazine* **57**, 677-685.

Mohan N. and Müller A. (1972) Determination of the exact force-field of SiCl$_4$ from ^{35}Cl-^{37}Cl isotope shift and analysis of the vibrational spectra of Si^{35}Cl$_3$Cl, Si^{35}Cl$_2$^{37}Cl$_2$, Si^{35}Cl^{37}Cl$_3$, ^{28}SiCl$_4$, ^{29}SiCl$_4$, and ^{30}SiCl$_4$. *Journal of Molecular Spectroscopy* **42**, 203-207.

Müller H. S. P., Helminger P., and Young S. H. (1997a) Millimeter and submillimeter spectroscopy of chlorine nitrate: the Cl quadrupole tensor and the harmonic force field. *Journal of Molecular Spectroscopy* **181**, 363-378.

Müller H. S. P., Sorensen G. O., Birk M., and Friedl R. R. (1997b) The rotational spectrum and anharmonic force field of chlorine dioxide, OClO. *Journal of Molecular Spectroscopy* **186**, 177-188.

Müller H. S. P. and Willner H. (1993) Vibrational and electronic spectra of chlorine dioxide, OClO, and chlorine superoxide, ClOO, isolated in cryogenic matrices. *J. Phys. Chem.* **97**, 10589-10598.

Nakamoto K. (1997) *Infrared and Raman Spectra of Inorganic and Coordination Compounds*. John Wiley & Sons, Inc.

Nilsson G. G. (1979) Phonon frequencies in off-symmetry directions of NaCl determined by neutron inelastic scattering. *Phys. Stat. Sol. B* **91**, 83-86.

Oberti R., Ungaretti L., Cannillo E., and Hawthorne F. C. (1993) The mechanism of Cl incorporation in amphibole. *American Mineralogist* **78**, 746-752.

Orphal J., Morillon-Chapey M., Diallo A., and Guelachvili G. (1997) High-resolution infrared spectra and harmonic force field of chlorine nitrate. *J. Phys. Chem. A* **101**, 1062-1067.

Orphal J., Morillon-Chapey M., Klee S., Mellau G. C., and Winnewisser M. (1998) The far-infrared spectrum of $ClNO_2$ studied by high-resolution Fourier-transform spectroscopy. *Journal of Molecular Spectroscopy* **190**, 101-106.

Parekunnel T., Hirao T., Le Roy R. J., and Bernath P. F. (1999) FTIR emission spectra and molecular constants for DCl. *Journal of Molecular Spectroscopy* **195**, 185-191.

Parrington J. R., Knox H. D., Breneman S. L., Baum E. M., and Feiner F. (1996) *Chart of the Nuclides*. General Electric Co. and KAPL Inc.

Pasternak A. (1976) Lattice dynamics of $FeCl_2$. *J. Phys. C.: Solid State Phys.* **9**, 2987-2995.

Pople J. A., Scott A. P., Wong M. W., and Radom L. (1993) Scaling factors for obtaining fundamental vibrational frequencies and zero-point energies from HF/6-31G* and MP2/6-31G* harmonic frequencies. *Israel Journal of Chemistry* **33**, 345-350.

Ransom B., Spivack A. J., and Kastner M. (1995) Stable Cl isotopes in subduction-zone pore waters: Implications for fluid-rock reactions and the cycling of chlorine. *Geology* **23**, 715-718.

Raunio G. and Almquist L. (1969) Dispersion relations for phonons in KCl at 80 and 300oK. *Phys. Stat. Sol.* **33**, 209-215.

Raunio G., Almquist L., and Stedman R. (1969) Phonon dispersion relations in NaCl. *Physical Review* **178**, 1496-1501.

Raunio G. and Rolandson S. (1970a) Lattice dynamics of NaCl, KCl, RbCl, and RbF. *Physical Review B.* **2**, 2098-2103.

Raunio G. and Rolandson S. (1970b) Phonon dispersion relations in RbCl and RbF at 80 K. *J. Phys. C.: Solid State Phys.* **3**, 1013-1025.

Richet P., Bottinga Y., and Javoy M. (1977) A review of hydrogen, carbon, nitrogen, oxygen, sulphur, and chlorine stable isotope fractionation among gaseous molecules. *Ann. Rev. Earth Planet. Sci.* **5**, 65-110.

Rochekind M. M. and Pimentel G. C. (1965) Infrared spectrum and vibrational assignment for chlorine monoxide, Cl_2O. *J. Chem. Phys.* **42**, 1361-1368.

Schauble E. A., Rossman G. R., and Taylor H. P., Jr. (2001) Theoretical estimates of equilibrium Fe-isotope fractionations from vibrational spectroscopy. *Geochimica et Cosmochimica Acta* **65**, 2487-2497.

Schmidt K. H. and Müller A. (1974) Vibrational Spectrum of H^{13}CCl$_3$ and the force field of chloroform. *Journal of Molecular Spectroscopy* **50**, 115-125.

Schmidt M. W., Baldridge K. K., Boatz J. A., Elbert S. T., Gordon M. S., Jensen J. J., Koseki S., Matsunaga N., Nguyen K. A., Su S., Windus T. L., Dupuis M., and Montgomery J. A. (1993) General atomic and molecular electronic-structure system. *J. Comput. Chem.* **14**, 1347-1363.

Schmunk R. E. and Winder D. R. (1970) Lattice dynamics of sodium chloride at room temperature. *J. Phys. Chem. Solids* **31**, 131-141.

Schnöckel H. G. and Becher H. J. (1975) ^{35}Cl/^{37}Cl-verschiebungen in den Infrarotspektren von matrixisoliertem Tetrachloräthylen und Phosgen und ihre Auswertung in der Kraftkonstantenberechnung. *J. Mol. Struct.* **25**, 369-376.

Schrader B. and Meier W. (1974) *DMS Raman/IR Atlas of Organic Compounds.* Verlag Chemie GmbH.

Scott A. P. and Radom L. (1996) Harmonic vibrational frequencies: An evaluation of Hartree-Fock, Møller-Plesset, quadratic configuration interaction, density functional theory, and semiempirical scale factors. *J. Phys. Chem.* **100**, 16502-16513.

Snels M., D'Amico G., Piccarreta L., Hollenstein H., and Quack M. (2001) Diode-laser jet spectra and analysis of the ν_1 and ν_4 fundamentals of CCl$_3$F. *Journal of Molecular Spectroscopy* **205**, 102-109.

Sturchio N. C., Clausen J. L., Heraty L. J., Huang L., Holt B. D., and Abrajano T. J. (1998) Chlorine isotope investigation of natural attenuation of trichloroethene in an aerobic aquifer. *Environmental Science & Technology* **32**(20), 3037-3042.

Tanaka H. and Hisano K. (1989) A far-infrared emission study on the phonon self-energy of KCl at high temperature. *J. Phys.: Condens. Matter* **1**, 9539-9545.

Urey H. C. (1947) The thermodynamic properties of isotopic substances. *J. Chem. Soc.*, 562-581.

Urey H. C. and Greiff L. J. (1935) Isotopic exchange equilibria. *J. Am. Chem. Soc.* **57**, 321-327.

Vengosh A., Chivas A. R., and McCulloch M. T. (1989) Direct determination of boron and chlorine isotopic compositions in geological materials by negative thermal-ionization mass spectrometry. *Chemical Geology* **79**, 333-343.

Vettier C. and Yelon W. B. (1975) The structure of $FeCl_2$ at high pressures. *J. Phys. Chem. Solids* **36**, 401-405.

Volfinger M., Robert J.-L., Vielzeuf D., and Neiva A. M. R. (1985) Structural control of the chlorine content of OH-bearing silicates (micas and amphiboles). *Geochimica et Cosmochimica Acta* **49**, 37-48.

Volpe C. and Spivack A. J. (1994) Stable chlorine isotopic composition of marine aerosol particles in the western Atlantic Ocean. *Geophysical Research Letters* **21**(12), 1161-1164.

Volpe C., Wahlen M., Pszenny A. A. P., and Spivack A. J. (1998) Chlorine isotopic composition of marine aerosols: Implications for the release of reactive chlorine and HCl cycling rates. *Geophysical Research Letters* **25**(20), 3831-3834.

Wakamura K. (1993) Thermal expansion and anharmonic phonon-phonon interaction effects on an effective charge in GaAs and KCl. *J. Phys. Chem. Solids* **54**(3), 387-395.

Wong M. W. (1996) Vibrational frequency prediction using density functional theory. *Chemical Physics Letters* **256**, 391-399.

Xiao Y.-K. and Zhang C.-G. (1992) High precision isotopic measurement of chlorine by thermal ionization mass spectrometry of the Cs_2Cl^+ ion. *Intl. J. Mass Spectrom. Ion Proc.* **116**, 183-192.

Xu Y., McKellar A. R. W., Burkholder J. B., and Orlando J. J. (1996) High-resolution infrared spectrum of the ν_1 and ν_3 bands of dichlorine monoxide, Cl_2O. *Journal of Molecular Spectroscopy* **175**, 68-72.

Yelon W. B., Scherm R., and Vettier C. (1974) Acoustic phonon spectra of $FeCl_2$. *Solid State Communications* **15**, 391-394.

Table 3.1. Comparison between observed, *ab initio* (HF/6-31G*), and empirical force-field derived shifts in vibrational frequencies ($^{37}\nu/^{35}\nu$). The symmetry of each vibrational mode is indicated in parentheses.

Species	Vibrational Mode	Frequency w/^{35}Cl (cm^{-1})		# of ^{37}Cl's in substituted molecule	Mode symm. in substituted molecule	Frequency Ratio ($^{37}\nu/^{35}\nu$)		
		Expt.	HF/6-31G*			Observed	Emp. FF	HF/6-31G*
SiCl$_4$	ν_3 (F$_2$)	616.5	650.20	4	F$_2$	0.9908	0.9907	0.9910
CCl$_3$F	ν_1 (A$_1$)	1081.28	1269.49	1	A´	0.9995	—	1.0000
	ν_2 (A$_1$)	538.16	583.95	1	A´	0.9952[a], 0.9955[b]	—	0.9951
	ν_3 (A$_1$)	351.41	385.25	1	A´	0.9938	—	0.9938
	ν_5 (E)	838.5	966.51	1	A´	0.9984	—	0.9984
CCl$_4$	ν_4 (F$_2$)	313.6	348.25	1	E	0.9962	0.9962	0.9962
	ν_4 (F$_2$)	313.6	348.25	1	A$_1$	0.9879	0.9879	0.9880
	ν_3 (F$_2$)	779.01	902.40	1	E	0.9977	—	0.9976
	ν_3 (F$_2$)	779.01	902.40	1	A$_1$	0.9997	—	0.9999
CHCl$_3$	ν_2 (A$_1$)	675.5	730.74	3	A$_1$	0.9930	0.9926	0.9929
	ν_3 (A$_1$)	366.8	403.47	3	A$_1$	0.9771	0.9770	0.9766
	ν_5 (E)	774.25	874.49	3	E	0.9952	0.9949	0.9950
CH$_2$Cl$_2$	ν_5 (A$_1$)	711.9	774.44	1	A´	0.9961	0.9954	0.9959
	ν_9 (B$_2$)	749.4	842.64	1	A´	0.9973	0.9971	0.9970
CH$_3$Cl	ν_3 (A$_1$)	732.84	782.60	1	A$_1$	0.9920	0.9918	0.9919
	ν_6 (E)	1018.07	1138.36	1	E	0.99962	0.99961	0.99961
C$_2$Cl$_4$	ν_9 (B$_{2u}$)	908	999.67	4	B$_{2u}$	0.9948	—	0.9947
	ν_9 (B$_{3u}$)	777	850.31	1	A´	0.9977	—	0.9982
[ClO$_4$]$^-$	ν_3 (F$_2$)	1101.5	1188.09	1	F$_2$	0.9867[c], 0.9879[d]	0.9880[d]	0.9874
	ν_4 (F$_2$)	624	668.08	1	F$_2$	0.9952[c]	0.9944[d]	0.9949
ClNO$_2$	ν_2 (A$_1$)	792.76	934.26	1	A1	0.9994	—	0.9997
	ν_3 (A$_1$)	370.15	519.20	1	A$_1$	0.9848	—	0.9848

85

^{2}Cl$_2$O	ν_1 (A$_1$)	641.97	756.66	1	A´	0.9954	—	0.99512
OClO	ν_1 (A$_1$)	945.59	1067.94	1	A$_1$	0.9937	0.9937	0.9939
	ν_2 (A$_1$)	447.70	507.65	1	A$_1$	0.9936	0.9936	0.9931

References: SiCl$_4$ (MOHAN and MÜLLER, 1972); CCl$_3$F [a](SNELS et al., 2001), [b](KING, 1968); CCl$_4$ (JONES et al., 1984); CHCl$_3$ (CLARK et al., 1976; SCHMIDT and MÜLLER, 1974); CH$_2$Cl$_2$ (KING, 1968); CH$_3$Cl (BLACK and LAW, 2001); C$_2$Cl$_4$ (SCHNÖCKEL and BECHER, 1975); [ClO$_4$]$^-$ [c](CHABANEL et al., 1996), [d](DECIUS and MURHAMMER, 1980); ClNO$_2$ (DUXBURY and McPHEAT, 1995; ORPHAL et al., 1998); Cl$_2$O (XU et al., 1996); OClO (MÜLLER et al., 1997b; MÜLLER and WILLNER, 1993).

[1] - Ab initio model suspect because it predicts erroneous structures and frequencies.

[2] - Ab initio model suspect because it grossly overestimates the ν_3 (B$_2$) frequency (calc. 906 cm^{-1}, obs. 687 cm^{-1}).

Table 3.2. Vibrational frequencies of chlorine-bearing molecules and complexes. Only frequencies that are sensitive to [37]Cl-subsitution are listed. For each molecule, the ratio of the vibrational frequencies of [37]Cl-substituted (one [37]Cl per molecule) and [35]Cl-endmember species were calculated using an *ab initio* (HF/6-31G[*]) model. The symmetry and degeneracy of each vibrational mode in the [35]Cl-endmember molecule is indicated in parentheses. Isotopic substitution lowers the symmetry of some molecules, splitting degenerate vibrational modes into two or more distinct modes with different frequencies.

Species	Vibrational Mode	Frequency w/[35]Cl (cm^{-1})	Frequency Ratio ($^{37}v/^{35}v$) HF/6-31G[*]	Degeneracy of mode in [37]Cl-bearing molecule
HCl	–	2990.92	0.99924[1]	1
Cl$_2$	–	559.7	0.98640[1]	1
CCl$_3$F	v_1 (A$_1$, 1)	1081.28	0.99999	1
	v_2 (A$_1$, 1)	538.16	0.99514	1
	v_3 (A$_1$, 1)	351.41	0.99377	1
	v_4 (E, 2)	849.53	0.99993	1
			0.99838	1
	v_5 (E, 2)	399.2	0.99931	1
			0.99078	1
	v_6 (E, 2)	244.1	0.99492	1
			0.99010	1
CCl$_4$	v_1 (A$_1$, 1)	460.2	0.99332	1
	v_2 (E, 2)	218.8	0.99310	2
	v_3 (F$_2$, 3)	779.01	0.99992	2
			0.99756	1
	v_4 (F$_2$, 3)	313.6	0.99621	2
			0.98797	1
CHCl$_3$	v_1 (A$_1$, 1)	3033.1	1.00000	1
	v_2 (A$_1$, 1)	675.5	0.99758	1
	v_3 (A$_1$, 1)	366.8	0.99242	1
	v_4 (E, 2)	1219.7	0.99999	1
			0.99986	1
	v_5 (E, 2)	773.7	0.99995	1
			0.99674	1
	v_6 (E, 2)	259.9	0.99252	1
			0.99002	1
CH$_3$Cl	v_1 (A$_1$, 1)	3088.4	1.00000	1
	v_2 (A$_1$, 1)	1396.3	0.99991	1
	v_3 (A$_1$, 1)	751.2	0.99194	1
	v_4 (E, 2)	3183.3	1.00000	2
	v_5 (E, 2)	1496.2	0.99999	2
	v_6 (E, 2)	1036.8	0.99961	2
C$_2$Cl$_4$	v_1 (A$_{1g}$, 1)	1571	0.99997	1
	v_2 (A$_{1g}$, 1)	447	0.99336	1
	v_3 (A$_g$, 1)	235	0.99323	1

	ν_4 (A$_u$, 1)	110	0.99319	1
	ν_5 (B$_{1g}$, 1)	1000	0.99954	1
	ν_6 (B$_{1g}$, 1)	347	0.99348	1
	ν_7 (B$_{1u}$, 1)	288	0.99901	1
	ν_8 (B$_{2g}$, 1)	512	0.99980	1
	ν_9 (B$_{2u}$, 1)	908	0.99869	1
	ν_{10} (B$_{2u}$, 1)	176	0.99329	1
	ν_{11} (B$_{3u}$, 1)	777	0.99821	1
	ν_{12} (B$_{3u}$, 1)	310	0.99379	1
C_2HCl_3	ν_1 (A´, 1)	3082	1.00000/1.00000/1.00000[2]	1
	ν_2 (A´, 1)	1586	0.99998/0.99996/0.99997[2]	1
	ν_3 (A´, 1)	1247	1.00000/0.99995/0.99993[2]	1
	ν_4 (A´, 1)	931	0.99880/0.99893/0.99967[2]	1
	ν_5 (A´, 1)	780	0.99830/0.99996/0.99512[2]	1
	ν_6 (A´, 1)	630	0.99891/0.99129/0.99983[2]	1
	ν_7 (A´, 1)	384	0.98491/0.99834/0.99194[2]	1
	ν_8 (A´, 1)	277	0.99053/0.99013/0.99506[2]	1
	ν_9 (A´, 1)	178	0.99825/0.98698/98941[2]	1
	ν_{10} (A´´, 1)	840	0.99997/0.99999/0.99996[2]	1
	ν_{11} (A´´, 1)	451	0.99974/0.99905/0.99994[2]	1
	ν_{12} (A´´, 1)	215	0.99670/0.99991/0.99596[2]	1
$ClNO_2$	ν_1 (A$_1$, 1)	1267.99	0.99999	1
	ν_2 (A$_1$, 1)	792.76	0.99971	1
	ν_3 (A$_1$, 1)	370.15	0.98482	1
	ν_4 (B$_1$, 1)	652.3	0.99959	1
	ν_5 (B$_2$, 1)	1683.89	1.00000	1
	ν_6 (B$_2$, 1)	408.1	0.99532	1
HOCl	ν_1 (A´, 1)	3794.1	1.00000	1
	ν_2 (A´, 1)	1271.6	0.99966	1
	ν_3 (A´, 1)	742.5	0.99125	1
Cl_2O	ν_1 (A$_1$, 1)	641.97	0.99539[3]	1
	ν_2 (A$_1$, 1)	300	0.98812[3]	1
	ν_3 (B$_2$, 1)	686.59	0.99692[3]	1
$ClONO_2$	ν_1 (A´, 1)	1736.9	1.00000/0.999994[4]	1
	ν_2 (A´, 1)	1292.7	1.00000/0.999992[4]	1
	ν_3 (A´, 1)	809.4	0.99778/0.99792[4]	1
	ν_4 (A´, 1)	780.2	0.99846/0.99826[4]	1
	ν_5 (A´, 1)	563.1	0.99645/0.99690[4]	1
	ν_6 (A´, 1)	434.0	0.99470/0.99371[4]	1
	ν_7 (A´, 1)	273.3	0.98903/0.98956[4]	1
	ν_8 (A´´, 1)	711.0	1.00000/0.99999[4]	1
	ν_9 (A´´, 1)	121.9	0.99672/0.99643[4]	1
ClO	–	853.72	0.99149[1]	1

OClO	ν_1 (A$_1$, 1)	945.59	0.99389	1
	ν_2 (A$_1$, 1)	447.70	0.99309	1
	ν_3 (B$_2$, 1)	1110.11	0.98916	1
$[ClO_4]^-$	ν_3 (F$_2$, 3)	1115[5]	0.98737	3
	ν_4 (F$_2$, 3)	630[5]	0.99494	3

References: HCl, (PAREKUNNEL et al., 1999); Cl$_2$, (CLYNE and COXON, 1970); CCl$_3$F, (SNELS et al., 2001); CCl$_4$, (JONES et al., 1984);CHCl$_3$, (CLARK et al., 1976; SCHMIDT and MÜLLER, 1974); CH$_3$Cl, (BLACK and LAW, 2001); C$_2$Cl$_4$, (CASTRO and ANACONA, 1994); C$_2$HCl$_3$, (SCHRADER and MEIER, 1974) as tabulated in KISIEL and PSZCZÓLKOWSKI (1996); ClNO$_2$, (DUXBURY and McPHEAT, 1995; ORPHAL et al., 1997); HOCl, (ABEL et al., 1995); Cl$_2$O, (XU et al., 1996) for ν_1 and ν_3, (ROCHEKIND and PIMENTEL, 1965) for ν_2; ClONO$_2$, (ORPHAL et al., 1997); ClO, (BURKHOLDER et al., 1987);OClO, (MÜLLER et al., 1997b; MÜLLER and WILLNER, 1993) ; $[ClO_4]^-$, (CHABANEL et al., 1996) - aqueous solution average.

[1] Frequency ratios calculated from atomic and isotopic masses.

[2] Frequency ratios are listed for C$_2$HCl$_3$ molecules substituted at each of the three distinct Cl positions. The order in which the ratios are reported follows the labeling convention of KISIEL and PSZCZÓLKOWSKI (1996). The 2nd ratio listed corresponds to a molecule with ^{37}Cl at the position farthest from H, the 3rd ratio corresponds to a molecule with ^{37}Cl at the position nearest H.

[3] These frequency ratios are taken from published spectra (XU et al., 1996) and (for ν_2) the Redlich-Teller product rule, because HF/6-31G* ab initio model failed to give accurate vibrational frequencies for ^{35}Cl$_2$O.

[4] Frequency ratios are taken from force-field calculation of ORPHAL et al. (1997) (on left) and MÜLLER et al. (1997a) (on right), because HF/6-31G* ab initio model predicts an erroneous structure for ClONO$_2$.

[5] Frequencies measured in aqueous solution.

Table 3.3. Calculated reduced partition function ratios [$1000 \cdot \ln(\beta_{37-35})$] for ^{37}Cl-^{35}Cl exchange in molecules at various temperatures. Linear interpolation (with respect to $1/T^2$) between the temperatures reported here will reproduce the curves shown in Figs. 3.1-3.3 to within 0.1‰

Molecule		0°C	25°C	100°C	200°C	400°C	1000°C
Cl_2		8.62	7.37	4.88	3.11	1.57	0.45
HCl		5.21	4.71	3.61	2.69	1.67	0.61
C_2Cl_4		12.35	10.56	7.01	4.49	2.28	0.65
C_2HCl_3*	Cl-1: 11.64		9.95	6.59	4.21	2.14	0.61
	Cl-2: 12.26		10.50	6.99	4.49	2.28	0.65
	Cl-3: 11.02		9.45	6.31	4.06	2.07	0.59
	Mean: 11.64		9.97	6.63	4.25	2.16	0.62
CCl_3F		12.14	10.34	6.81	4.33	2.18	0.62
CCl_4		11.63	9.90	6.50	4.13	2.08	0.59
$CHCl_3$		10.98	9.40	6.24	4.00	2.03	0.58
CH_3Cl		10.16	8.80	6.00	3.92	2.03	0.59
$ClNO_2$		6.88	5.84	3.82	2.41	1.21	0.34
Cl_2O		8.88	7.60	5.04	3.23	1.64	0.47
HOCl		9.83	8.51	5.78	3.77	1.94	0.56
$ClONO_2$ #1		10.72	9.18	6.10	3.91	1.99	0.57
$ClONO_2$ #2		10.85	9.29	6.18	3.96	2.01	0.57
ClO		11.03	9.58	6.56	4.30	2.23	0.65
OClO		33.20	29.01	20.20	13.46	7.10	2.09
$[ClO_4]^-$		85.68	74.99	52.44	34.06	18.58	5.49

*Beta factors were calculated for each of the three Cl positions in C_2HCl_3. Results are labeled according to the convention of Kisiel and Pszczólkowski (1996). Cl-2 corresponds to the Cl position farthest from H, and Cl-3 corresponds to the Cl closest to H.

Table 3.4. Calculated reduced partition function ratios [$1000 \cdot \ln(\beta_{37\text{-}35})$] for ^{37}Cl-^{35}Cl exchange in NaCl (halite), KCl (sylvite), RbCl, MnCl$_2$, and FeCl$_2$. For the alkali halides, each tabulated result is the mean of several re-optimized lattice dynamics models. Numbers in parentheses show the number of models averaged and the standard deviation at each temperature. Linear interpolation (with respect to $1/T^2$) between the temperatures reported here will reproduce the curves shown in Fig. 3.4 to within 0.1‰.

Crystal	0°C	25°C	100°C	300°C
NaCl (n=4)	3.87 (0.060)	3.26 (0.050)	2.09 (0.032)	0.89 (0.014)
KCl (n=6)	2.96 (0.070)	2.48 (0.059)	1.59 (0.038)	0.68 (0.016)
RbCl (n=3)	2.78 (0.034)	2.34 (0.028)	1.50 (0.018)	0.64 (0.008)
FeCl$_2$	6.66	5.61	3.60	1.54
MnCl$_2$	6.20	5.22	3.35	1.43

References: NaCl 3 models from RAUNIO and ROLANDSON (1970a) were re-optimized to frequencies reported by RAUNIO et al. (1969); model II from SCHMUNK and WINDER (1970) was not reoptimized, because the measured frequencies are not tabulated. KCl 3 models from RAUNIO and ROLANDSON (1970a) were re-optimized to frequencies reported in RAUNIO and ALMQUIST (1969); the COPLEY et al. (1969) models (II, V, and VI) were re-optimized to the Copley et al. (1969) measured frequencies. RbCl, 3 models from RAUNIO and ROLANDSON (1970a) (3 models) were re-optimized to frequencies reported by RAUNIO and ROLANDSON (1970b). FeCl$_2$ and MnCl$_2$ models are from Benedek and Frey (1980), and were not re-optimized.

Figure 3.1 Plot of calculated reduced partition function ratios for ^{37}Cl-^{35}Cl exchange [$1000\cdot\ln(\beta_{37\text{-}35})$] vs. $10^6/T^2$ above 273 K for several substances studied (see Tables 3.3 and 3.4).

Fig. 3.1.
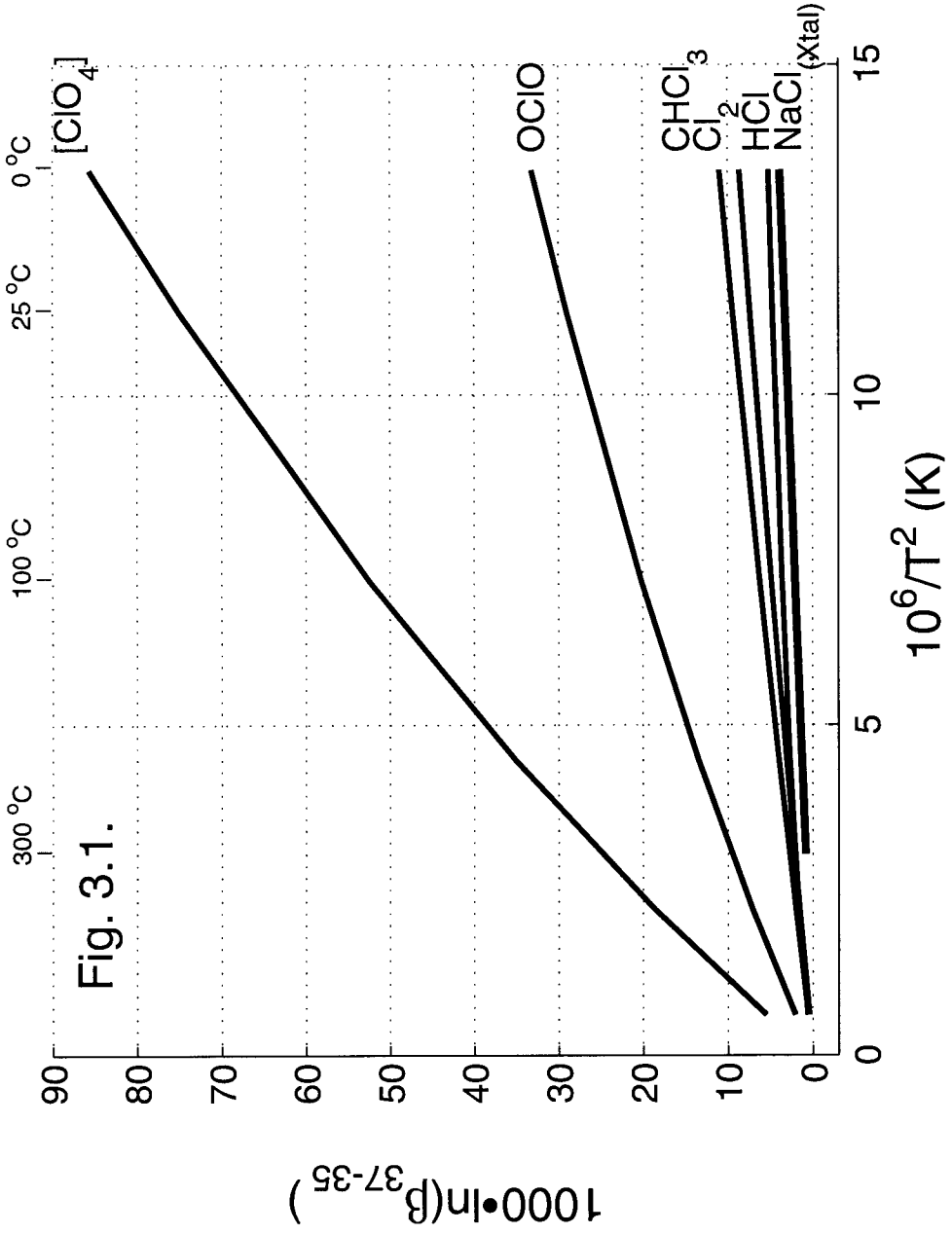
Figure 3.2 Plot of calculated reduced partition function ratios for ^{37}Cl-^{35}Cl exchange [1000•ln(β_{37-35})] vs. $10^6/T^2$ in small Cl-bearing organic molecules (see Table 3.3).

Fig. 3.2.
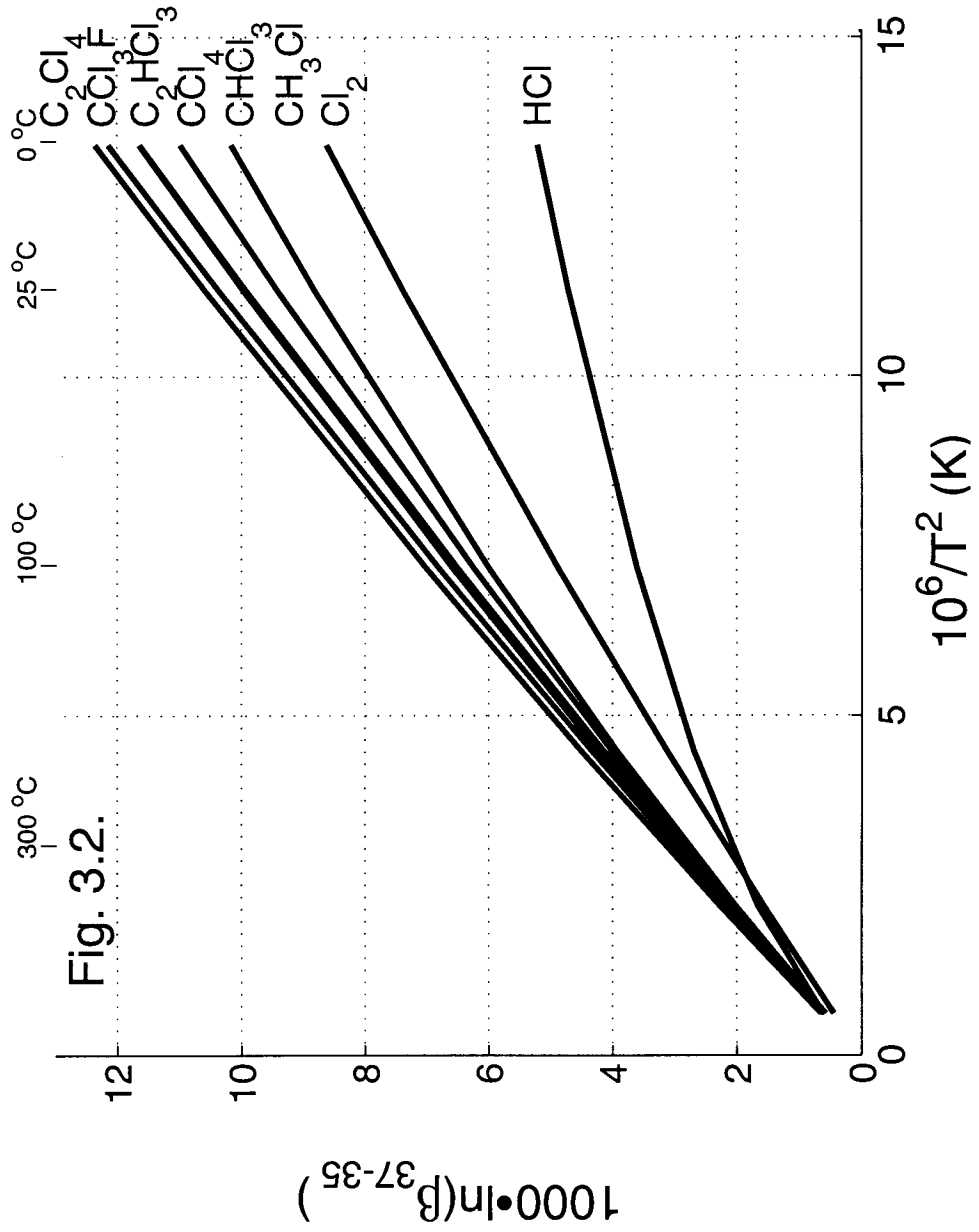
Figure 3.3 Plot of calculated reduced partition function ratios ^{37}Cl-^{35}Cl exchange [$1000 \cdot \ln(\beta_{37\text{-}35})$] vs. $10^6/T^2$ in molecules of interest in atmospheric chemistry(see Table 3.3).

Fig. 3.3.
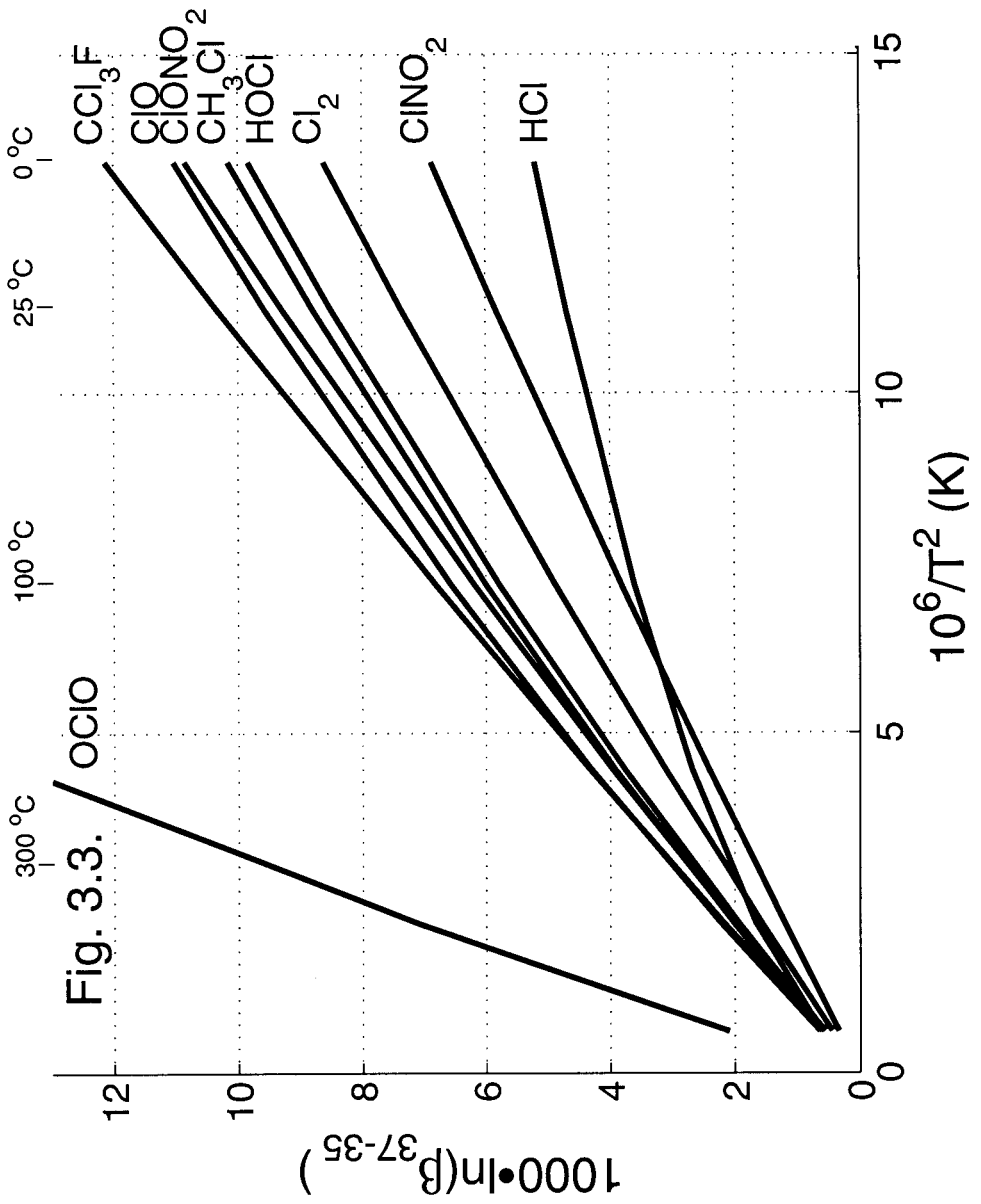
Figure 3.4 Plot of calculated reduced partition function ratios ^{37}Cl-^{35}Cl exchange

[$1000 \cdot \ln(\beta_{37\text{-}35})$] vs. $10^6/T^2$ in solid chlorides. The thicknesses of lines plotted for NaCl,

KCl, and RbCl represent ranges calculated using different reoptimized lattice dynamics

models(see text).

98
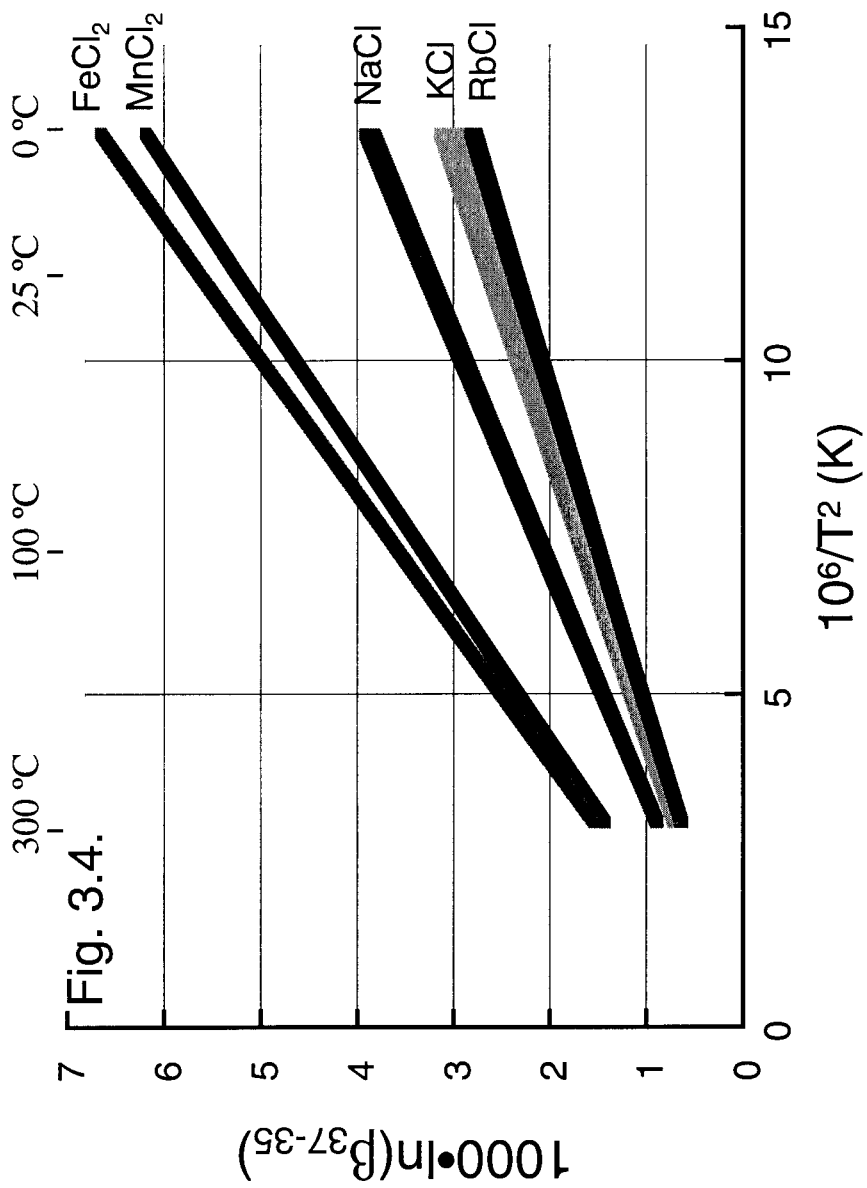
Fig. 3.4.

Figure 3.5 Correlation between calculated reduced partition function ratios (at 298 K) and the oxidation state of chlorine in substances containing Cl-metal and Cl-O bonds. Chlorine-bearing organic species have been excluded from this plot.

Fig. 3.5.
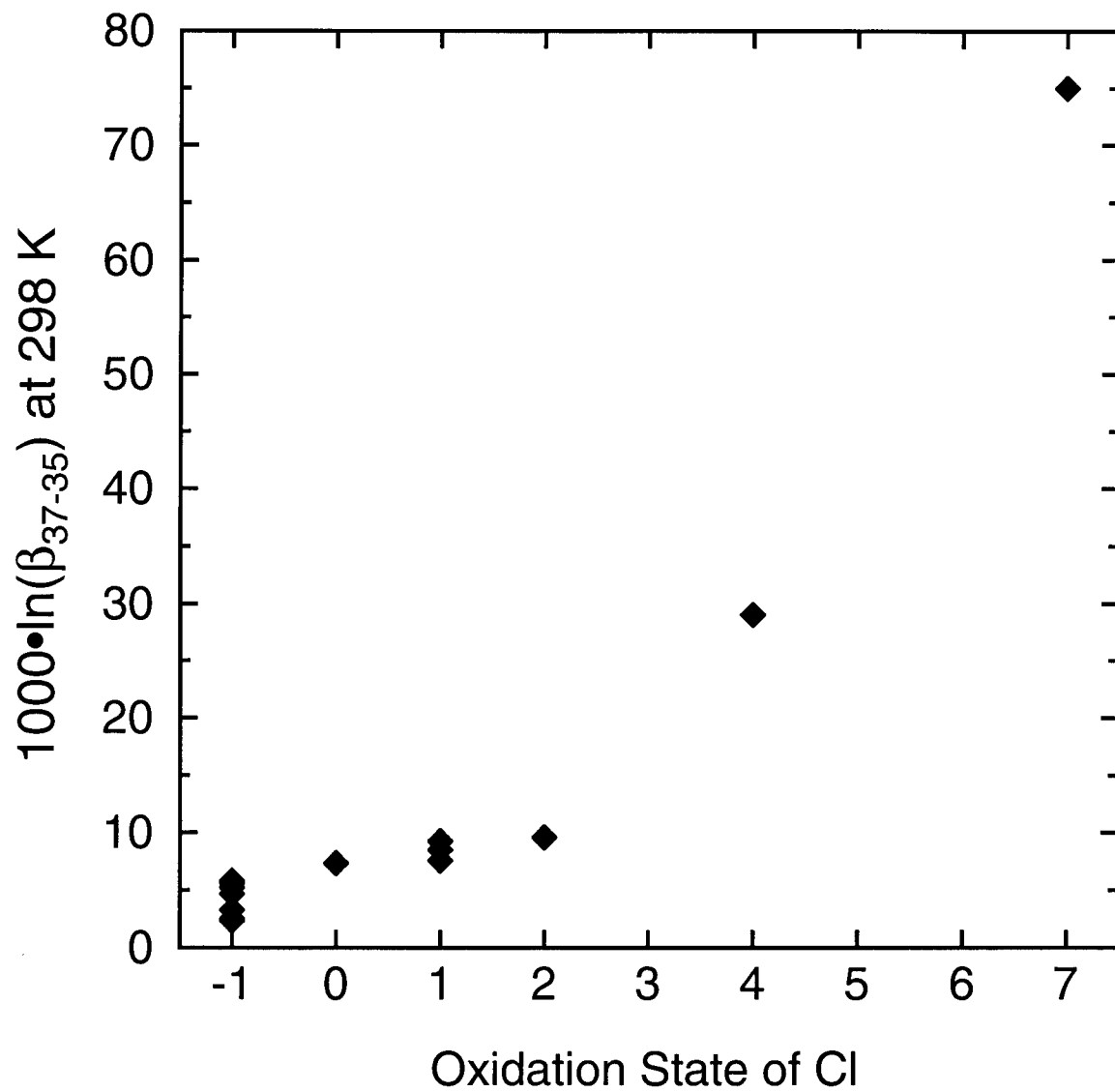
Chapter 4. Theoretical estimates of equilibrium chromium-isotope fractionations

Equilibrium Cr-isotope (^{53}Cr/^{52}Cr) fractionations are calculated using published

vibrational spectra and both empirical and *ab initio* force-field models. Reduced partition

function ratios for chromium isotope exchange [i.e., $1000 \cdot \ln(\beta_{53-52})$] are calculated for a

number of simple complexes, crystals, and the $Cr(CO)_6$ molecule. Large (> 1‰)

fractionations are predicted between coexisting species with different oxidation states or

bond partners. The highly oxidized $[Cr^{6+}O_4]^{2-}$ anion will tend to concentrate ^{53}Cr when in

equilibrium with compounds containing Cr^{3+} or Cr^0. Substances containing chromium

bonded to strongly bonding ligands like CO will concentrate ^{53}Cr relative to compounds

with weaker bonds, like $[CrCl_6]^{3-}$. Substances with short Cr-ligand bonds (Cr-C in

$Cr(CO)_6$, Cr-O in $[Cr(H_2O)_6]^{3+}$ or $[CrO_4]^{2-}$) will also tend to concentrate ^{53}Cr relative to

substances with longer Cr-ligand bonds ($[Cr(NH_3)_6]^{3+}$, $[CrCl_6]^{3-}$, Cr-metal). These results

are similar to the systematics found in an earlier study on Fe-isotope fractionation

(SCHAUBLE et al., 2001).

The calculated equilibrium fractionation between $[CrO_4]^{2-}$ and $[Cr(H_2O)_6]^{3+}$ (or

Cr_2O_3) agrees qualitatively with the fractionation observed during experimental (kinetic?)

reduction of $[CrO_4]^{2-}$ in solution (ELLIS et al., 2002), although the calculated

fractionation (~6-7‰ at 298 K) does appear to be significantly larger than the

experimental fractionation (3.3-3.5‰). Our results suggest that natural inorganic Cr-

isotope fractionation at the earth's surface will be driven largely by reduction and

oxidation processes.

4.1. Introduction

The purpose of this study is to estimate equilibrium chromium-isotope fractionations, to help provide a theoretical framework for planning and interpreting Cr-isotope measurements on natural samples. The authors are not aware of any prior theoretical work on this subject. A variety of Cr-bearing complexes, molecular $Cr(CO)_6$, and crystalline Cr_2O_3 and Cr-metal are investigated, with a focus on analogues for geochemically important species.

Chromium is one of a group of transition elements which are being examined with renewed interest, because of recent measurements of variability in the abundances of their stable isotopes (BALL and BASSETT, 2000; ELLIS et al., 2002). Chromium, with four stable isotopes (mass #'s 50, 52, 53, and 54) is interesting because of its variable redox chemistry (Cr^{3+} vs. Cr^{6+}) in natural and polluted waters. In rocks, Cr almost always occurs as a substituent in oxides, oxyhydroxides, or silicates as a 3+ cation with a strong preference for octahedral coordination. Chromium is highly insoluble in the 3+ oxidation state. Cr^{6+}, in contrast, forms soluble tetrahedral oxyanions, $[CrO_4]^{2-}$ and $[HCrO_4]^{-}$, making this form of chromium useful for industrial applications such as electroplating. Unfortunately, Cr^{6+} is also a carcinogen (KORTENKAMP et al., 1996) and groundwater pollutant. Cr-isotope abundance anomalies of up to 8‰ (in $^{53}Cr/^{52}Cr$) have been measured in both natural and Cr^{6+}-polluted groundwaters (BALL and BASSETT, 2000), and 3-4‰ fractionations are observed in laboratory experiments where Cr^{6+} is reduced to Cr^{3+} (ELLIS et al., 2002).

Equilibrium stable isotope fractionations are caused mainly by small differences in the vibrational energies of isotopically light and heavy substances (BIGELEISEN and

MAYER, 1947; RICHET et al., 1977; UREY, 1947). The isotopically heavy form of a substance vibrates at lower frequencies than the isotopically light form, so that the vibrational energy of the heavy form is also lower than the light form. This decrease in vibrational energy varies from one substance to another, typically it is most pronounced in substances with strong, stiff chemical bonds. The variability in the change in vibrational energy means that there is a small energy associated with isotopic exchange between different substances, causing unequal partitioning of the isotopes between those substances when they equilibrate. The tendency of a substance to concentrate heavy isotopes is expressed in terms of a β-factor (i.e., $\beta_{53\text{-}52}$ for $^{53}Cr\text{-}^{52}Cr$ exchange), defined as the ratio at equilibrium of the isotope ratio of the substance of interest to the isotope ratio of dissociated atoms. β is equivalent to the factor $(s/s')f$ as defined by BIGELEISEN and MAYER (1947). It is convenient to report results as reduced partition function ratios [i.e., $1000 \cdot \ln\beta$], because $1000 \cdot \ln(\beta_{53\text{-}52}[X]) - 1000 \cdot \ln(\beta_{53\text{-}52}[Y]) \approx \delta^{53}Cr_X - \delta^{53}Cr_Y$ at equilibrium. In the present study calculated $^{53}Cr/^{52}Cr$ fractionations are reported. Fractionations between other Cr-isotopes can be easily calculated from these data, because the magnitude of fractionation scales almost linearly with the difference in the masses of the isotopes of interest.

4.2. Methods

Equilibrium Cr-isotope fractionation factors are calculated using the standard thermodynamic, quantum mechanical approach (i.e., KIEFFER, 1982, eqn. 15 for crystals and UREY, 1947, eq. 4' for complexes). In this approach, it is necessary to know the frequencies of all Cr-isotope sensitive vibrational modes for at least two isotopic forms of each substance. Calculations assume that vibrations are harmonic, mainly because

anharmonic corrections are unavailable for the substances of interest. The effects of anharmonicity are expected to be quite small for gas-phase molecules, on the order of a few tenths per mil at room temperature, less is known about anharmonicity in condensed phases. Cr_2O_3 is a refractory oxide with a high Debye temperature, suggesting that anharmonicity is not a major source of error at moderate temperatures. The effects of temperature on vibrational frequencies in α-Cr metal have been directly measured (TRAMPENAU et al., 1993), allowing a direct estimate of anharmonicity-induced errors. Studied species are either metal-centered complexes, or minerals, so the effects of quantized rotations should be negligible. Measured vibrational frequencies for each substance have been compiled from the literature. In most cases, spectral measurements on complexes were made on weakly bonded salts or molecular crystals. For these complexes, lattice effects and intermolecular vibrations are ignored, and only internal vibrations for each complex are used in calculations. When possible, vibrational frequencies measured in different salts are compared to estimate the errors resulting from this simplified treatment.

Cr^{3+} is a d^3 cation, and as such strongly prefers octahedral (6-fold) coordination in most chemical environments. It forms many stable, kinetically inert octahedral complexes. This stability makes Cr^{3+} a good subject for spectroscopic study, and high-quality vibrational spectra are available for a variety of Cr^{3+}-bearing substances. Complexes containing Cr^{6+} have also been extensively studied. In most cases, measured samples were prepared with the natural mixture of chromium isotopes, which is dominated by ^{52}Cr (83.8 atom %). However, some vibrational data are available for isotopically substituted Cr-bearing substances, including α-Cr_2O_3 (TARTE and

PREUDHOMME, 1970), $[Cr(H_2O)_6]^{3+}$ (BEST et al., 1980), $[Cr(NH_3)_6]^{3+}$ (SCHMIDT and MÜLLER, 1974), and $[CrO_4]^{2-}$ (MÜLLER and KÖNIGER, 1974). Chromium hexacarbonyl $(Cr^0(CO)_6)$ is an example of a low-spin d^6 metal complex, and one vibrational frequency has been identified in several Cr-isotopic forms (TEVAULT and NAKAMOTO, 1975). In general, however, the vibrational spectra of isotopically substituted species are incomplete, and it is necessary to create a model to predict unknown vibrational species.

In the present work we used simple empirical force fields fit to known vibrational frequencies, as well as *ab initio* molecular force fields calculated from first principles. Empirical molecular force fields (like the Modified Urey-Bradley Force Field, or MUBFF for short (NAKAMOTO, 1997)) have been shown to give reasonably accurate predictions of unknown frequencies for isotopically substituted tetrahedral and octahedral molecules and metal-bearing complexes (SCHAUBLE et al., 2001). *Ab initio* force fields are superior, at least in principle, because calculated vibrational frequencies and molecular structures can be compared to independent measurements. Density functional theory (DFT) and hybrid Hartree-Fock/DFT methods are commonly used to estimate structures and frequencies for molecules and complexes containing transition elements. We used the hybrid B3LYP method (including the VWN5 functional, HERTWIG and KOCH, 1997), as well as computationally faster (but less accurate) Hartree-Fock methods to generate force fields for $Cr(CO)_6$, $[Cr(H_2O)_6]^{3+}$, and $[CrO_4]^{2-}$. It is worth mentioning that the B3LYP method is not strictly *ab initio*, because some semi-empirical coefficients were used in the original determination of relative DFT and Hartree-Fock contributions to the electron exchange-correlation functional (BECKE, 1993). Atomic orbitals are built up from the medium-sized all-electron 6-31G* basis set (RASSOLOV et al., 1998), as well as

with the smaller LANL2DZ basis set (HAY and WADT, 1985), which uses effective core potentials for inner-shell transition element electrons. *Ab initio* models treat all three species as gas-phase molecules. Calculations were performed using Macintosh and Unix versions of the GAMESS (US) quantum chemistry package (SCHMIDT et al., 1993). Geometry optimizations used symmetry constraints appropriate to each molecule, complex, and cluster, and atomic positions in each molecule were optimized until the residual forces on each atom were less than 2 x 10^{-5} hartree/bohr ($\approx 1.6 \times 10^{-12}$ N). Vibrational frequencies were calculated at the optimized geometries. The B3LYP models gave reasonably accurate bond lengths (within ~0.02 Å) and vibrational frequencies (within ~10%) for $Cr(CO)_6$ and $[CrO_4]^{2-}$, Hartree-Fock models for $Cr(CO)_6$ and $[CrO_4]^{2-}$ gave Cr-C bonds that were ~0.07 Å too long and Cr-O bonds that were ~0.05 Å too short. Hartree-Fock vibrational frequencies were also not as close to measured values as were B3LYP frequencies. All *ab initio* results for $[Cr(H_2O)_6]^{3+}$ were less than satisfactory (bonds 0.02-0.04 Å too long, frequencies > 10 % too low), and we found it necessary to add a shell of 12 2nd-nearest neighbor water molecules around the complex to make the models reasonably accurate. These results are in accord with prior *ab initio* work on cationic aquo complexes (e.g., ÅKESSON et al., 1994; RUDOLPH et al., 2000). A more detailed description of the methods applied to each complex may be found in the Appendix.

For all of the Cr-bearing complexes and $Cr(CO)_6$, force fields are used to calculate ratios of vibrational frequencies in ^{52}Cr- and ^{53}Cr-bearing species. The calculated ratios are multiplied by observed (^{52}Cr-dominated) frequencies to get model frequencies for the

^{53}Cr-endmember species. For crystals, frequency spectra generated by lattice-dynamics models are used directly in the calculation of reduced partition function ratios.

4.3. Results

4.3.1. Calculated Fractionations

Calculated reduced partition function ratios for ^{52}Cr-^{53}Cr exchange are shown in Table 4.2 and Figure 4.1. The results clearly suggest that measurable fractionations of the stable chromium isotopes will occur when chemically distinct Cr-bearing substances equilibrate. The highly oxidized $[CrO_4]^{2-}$ complex will tend to concentrate ^{53}Cr relative to substances containing Cr^{3+} and Cr^0. Among Cr^{3+} species, those with Cr-O bonds (including Cr_2O_3 and $[Cr(H_2O)_6]^{3+}$) will concentrate ^{53}Cr relative to species with Cr-N and Cr-Cl bonds ($[Cr(NH_3)_6]^{3+}$ and $[CrCl_6]^{3-}$). The low-spin, Cr^0-bearing $Cr(CO)_6$ molecule will be intermediate between Cr^{6+}- and Cr^{3+}-bearing species, while metallic chromium will tend to concentrate ^{52}Cr relative to most other species. The two Cr^{3+}-O bearing species are predicted to have similar affinities for ^{53}Cr, suggesting that fractionations among different Cr^{3+}-oxide, hydroxide, and aquo species will be small, ca. 1‰ or less at room temperature.

4.3.2. Accuracy Estimates

The results in Table 4.2 and Fig. 4.1 also clearly show that calculated isotope fractionations depend somewhat on the model used to predict vibrational frequencies for ^{53}Cr-bearing species. Near room temperature (ca. 298 K), the discrepancies between different models for the same substance are much larger than quoted Cr-isotope measurement uncertainties (ELLIS et al., 2002). Interestingly, there is no obvious

systematic difference between empirical force-field models, *ab initio* force-field models, and measured Cr-isotope vibrational frequency shifts. Measured shifts for $[CrO_4]^{2-}$ are larger than most of the force-field calculations suggest, while for $[Cr(H_2O)_6]^{3+}$ and $[Cr(NH_3)_6]^{3+}$ measured shifts are smaller than calculated shifts. For $Cr(CO)_6$, observed ^{53}Cr-^{52}Cr shifts for the ν_7 mode ($^{53}\nu/^{52}\nu \approx 0.9970$) are at the small end of calculated shifts, but the opposite is true for ^{54}Cr-^{53}Cr shifts (TEVAULT and NAKAMOTO, 1975)! We do not completely understand the source of the disagreements, but we can identify some of the factors likely to play a role. One is measurement uncertainty. Measured shifts are typically on the order of 1-5 cm^{-1}, and uncertainties as small as 0.5 cm^{-1} between the different isotopic forms of each substance are significant. This level of precision can be difficult to obtain, particularly when absorption peaks are broad and multiple absorption peaks are closely grouped. Another possible source of measurement uncertainty is imperfect isotopic substitution. Force-field models assume 100% isotopic purity for Cr-isotopic forms of each substance, but measured substances are isotopically impure. In the case of $[Cr(H_2O)_6]^{3+}$, likely ^{52}Cr contamination of ^{50}Cr- and ^{53}Cr-bearing species may have caused measured shifts for ν_3 to be as much as ~0.2 cm^{-1} smaller than in an ideal system. For $[CrO_4]^{2-}$ the difference may be as much as 0.6 cm^{-1}, for $[Cr(NH_3)_6]^{3+}$ ~0.3 cm^{-1}. Finally, it is possible that not all Cr-isotope sensitive vibrations for each substance were identified. This is particularly true for $[Cr(H_2O)_6]^{3+}$, where *ab initio* results suggest that there are Cr-isotope sensitive bending vibrations at frequencies below those so far measured, and that some higher frequency $Cr-OH_2$ wagging/rocking vibrations may also be slightly Cr-isotope sensitive. The measured shifts for this complex are much smaller that a Redlich-Teller Product Rule (NAKAMOTO, 1997) calculation would suggest, which

also suggests that one or more Cr-isotope sensitive frequencies were not identified. Measurement error is probably random, while incomplete isotopic substitution and missed Cr-isotope sensitive vibrational modes will cause measured shifts to be smaller than shifts calculated with force fields.

It is also important to note the significant disagreements between different force fields for each substance. These clearly show that force-field calculations contain their own errors, but as yet it is not possible to definitively identify the most robust type of force field. The relatively good agreement between B3LYP force fields constructed with LANL2DZ and 6-31G* basis sets, however, and their fidelity to measured structures and vibrational frequencies, suggest that these may be the most reliable. The B3LYP/6-31G* force-fields models are thus considered the "best guess," otherwise MUBFF force-field models are preferred for the sake of consistency. For Cr_2O_3, the two lattice dynamics force fields (MAY et al., 1997; SCHOBER et al., 1995) give similar results, differing by ~0.7‰ at 298 K. Both models are broadly consistent with the measurements of TARTE and PREUDHOMME (1970), which showed that the lowest-frequency IR-active vibration (at ca. 310 cm^{-1}) is highly sensitive to Cr-isotope substitution. In contrast to the TARTE and PREUDHOMME (1970) results, however, both models also predict measurable (> 0.3 cm^{-1}/amu) Cr-isotope sensitivity for higher-frequency IR-active vibrations.

The other likely source of error in calculated reduced partition function ratios is uncertainty in measured vibrational frequencies for the natural (^{52}Cr-dominated) isotopic form of each substance. These uncertainties are largest for charged complexes and crystalline Cr_2O_3. For $Cr(CO)_6$, which can be measured in the gas-phase and in inert-gas matrices, measured frequencies are probably accurate to within a few cm^{-1}, suggesting

uncertainties of ~0.2‰ in calculated reduced partition function ratios. In the case of charged complexes, most vibrational spectroscopic measurements (particularly infrared measurements) are made in molecular crystals rather than on species in solution. Observed frequencies may be affected by other components of the crystal and by other lattice effects. One way to evaluate these effects is to compare frequencies measured for a given complex in multiple types of crystal and in solution. In earlier work on Fe-bearing complexes, we found that frequencies could shift by as much as ~5% depending on the counter-ion in molecular crystals, or the composition of an aqueous solution (SCHAUBLE et al., 2001). Chromium-bearing complexes appear to behave similarly. Vibrational frequencies in the $[CrO_4]^{2-}$ anion have been measured in aqueous solution, and in K-, Rb-, and Cs-sulfate host lattices (KIEFER and BERNSTEIN, 1972; MÜLLER and KÖNIGER, 1974). The Cr-O stretching frequencies (v_3) of $[CrO_4]^{2-}$ in these substances range from 884-890 cm^{-1} in aqueous solution to 916 cm^{-1} in the K_2SO_4 lattice, a total range of ~4%. The Cr-O bending frequency (v_4) likewise varies by about 4%, from 368-369 cm^{-1} in aqueous solution to 383 cm^{-1} in Cs_2CrO_4. This variation suggests uncertainty of ~0.6‰ in the calculated reduced partition function ratio (at 298 K), although the relatively smaller range of measured frequencies in aqueous solutions might allow a smaller uncertainty. Vibrational frequencies of the $[CrCl_6]^{3-}$ complex have been measured in Rb_3CrCl_6, $Cr(NH_3)_6CrCl_6$, $Co(NH_3)_6CrCl_6$, $Rh(NH_3)_6CrCl_6$, and $Co(pn)_3CrCl_6$ (pn = 1,2-diaminopropane) (ADAMS and MORRIS, 1968; EYSEL, 1972), v_3 varies by ~4% from 313 cm^{-1} in $Co(NH_3)_6CrCl_6$ to 325 cm^{-1} in Rb_3CrCl_6, v_4 also varies by ~4% from 194 cm^{-1} in Rb_3CrCl_6 to 201 cm^{-1} in $Cr(NH_3)_6CrCl_6$. These uncertainties propagate to possible errors of ±0.2‰ in the reduced partition function ratio at 298 K. Measured frequencies for v_3

and ν_4 in the $[Cr(NH_3)_6]^{3+}$ complex in $Cr(NH_3)_6(NO_3)_3$, $Cr(NH_3)_6Cl_3$, $Cr(NH_3)_6(ClO_4)_3$ and aqueous solutions range from 461-470 cm^{-1} and 254-270 cm^{-1}, respectively, suggesting uncertainty of ~0.3‰ in the reduced partition function ratio at 298 K. Infrared-active frequencies of the $[Cr(H_2O)_6]^{3+}$ have only, to our knowledge, been measured in $CsCr(SO_4)_2 \bullet 12H_2O$ alum (Best et al. 1980), so we cannot directly estimate the uncertainties associated with lattice and solution-compositional effects. By analogy with the other complexes studied, it seems reasonable to estimate an uncertainty of ±5% in the measured frequency for the ν_3 Cr-O stretch – causing ±0.5‰ uncertainty in $1000 \bullet \ln(\beta_{53-52})$ at 298 K. For O-Cr-O bending (ν_4 in an ideal octahedral complex), we must consider the possibility of a low-frequency, Cr-isotope sensitive vibration that has not been detected. Our *ab initio* calculations suggest that this vibration may have a frequency of ~225-255 cm^{-1}, nearly 100 cm^{-1} lower than the measured "ν_4" frequency (Best et al, 1980). In this instance, the force-field-derived reduced partition function ratios in Table 4.2 could be as much as 0.6‰ too high. Errors resulting from neglect of possible Cr-isotope sensitive Cr-OH$_2$ wagging/rocking vibrations are smaller, probably causing calculated reduced partition function ratios to be no more than 0.2-0.3‰ too low.

Uncertainty in vibrational frequencies for ^{52}Cr-dominated Cr_2O_3 is likely to be an important source of error, but is more difficult to quantify. Only a tiny fraction of the vibrational density-of-states of Cr_2O_3 has been measured, and lattice dynamics force-field models are required to make the necessary extrapolation. In general, the models reproduce measured frequencies to within a few percent, but a few optical branches (including some IR and Raman active modes) are off by ca. 10 %. A rough estimate of

±1‰ for the uncertainty in calculated reduced partition function ratios for Cr_2O_3 may be reasonable.

Taken together, errors resulting from uncertainties in measured vibrational frequencies of ^{52}Cr-dominated substances, and calculated frequencies of ^{53}Cr-substituted substances (and $^{52}Cr_2O_3$) are on the order of +1/–2‰ at 298 K for $[CrO_4]^{2-}$, perhaps somewhat more than ±1‰ for Cr_2O_3, and ±1‰ for $Cr(CO)_6$, and $[Cr(H_2O)_6]^{3+}$. Smaller errors are likely for $[Cr(NH_3)_6]^{3+}$ (±0.5‰), $[CrCl_6]^{3-}$ (±0.3‰), and Cr-metal (±0.3‰).

4.4. Discussion

4.4.1. Factors Controlling Predicted Fractionations

The results predict measurable equilbrium stable isotope fractionation among chromium-bearing molecules, complexes, and minerals. Changes in oxidation state (Cr^{6+}-Cr^{3+}) or bond partner (H_2O vs. NH_3 or Cl^-) can drive fractionations of 1 to 6‰ at room temperature. The chemical systematics of calculated fractionations indicate which processes are likely to control equilibrium Cr-isotope fractionation in nature. By and large, these systematics are similar to those predicted for Fe-isotope fractionation.

Calculated reduced partition function ratios are mainly controlled by the frequencies of asymmetric Cr-ligand stretching vibrations. Figure 4.2a shows this relationship for the complexes and molecules that have well-defined asymmetric stretching modes. Cr-ligand stretching frequencies are themselves determined by the stiffness (e.g., spring constants) of Cr-ligand bonds, suggesting that strongly bonding ligands will preferentially bind heavy isotopes of chromium, particularly when those bonds are short. These relationships are shown in Figure 4.2b and c, which show $1000 \cdot \ln(\beta_{53-52})$ plotted against the position of

the ligands Cl⁻, H_2O, NH_3, and CO in the spectrochemical series (COTTON and

WILKINSON, 1988), and against the mean Cr-ligand bond length in each substance

studied. The position of a ligand in the spectrochemical series is a rough indicator of

relative covalent bonding strength. Chromium complexes with the strongest ligand (CO)

will concentrate heavy Cr-isotopes relative to most complexes with weaker ligands, while

the weakest ligand (Cl⁻) will concentrate light isotopes. As expected, NH_3 and H_2O are

intermediate, however $[Cr(H_2O)_6]^{3+}$ is predicted to concentrate heavy Cr-isotopes relative

to $[Cr(NH_3)_6]^{3+}$ despite the opposite arrangement of NH_3 and H_2O in the spectrochemical

series. A possible explanation is the length of Cr-N bonds in $[Cr(NH_3)_6]^{3+}$ (2.07 Å), ~0.1

Å longer than Cr-O bonds in $[Cr(H_2O)_6]^{3+}$ (~1.96 Å). Indeed, there is almost a monotonic

relationship between mean bond length and $1000 \cdot \ln(\beta_{53-52})$, suggesting that it may be

possible to crudely estimate equilibrium metal-isotope fractionations with structural data.

Coordination number is also likely to be important, but is difficult to evaluate for

Chromium because both major oxidation states have strongly preferred coordination

numbers.

The oxidation state of Cr is clearly a major factor controlling isotopic partitioning

behavior. A fractionation of ~6‰ is calculated between Cr^{6+} and Cr^{3+} in aqueous solution

at 298 K. As with iron (and other metals), frequencies of Cr-ligand stretching vibrations

generally increase with increasing oxidation state (as bond strength increases and bond

lengths decrease), suggesting that this behavior will be a general phenomenon in metal-

isotope systems, particularly when the bond partner does not change. Similar behavior is

also observed for S, Cl, and Se, and can be predicted for other heavy, redox-active

elements.

Calculated $1000 \cdot \ln(\beta_{53-52})$'s for Cr_2O_3 and $[Cr(H_2O)_6]^{3+}$ suggest that fractionations between different species where Cr^{3+} is octahedrally coordinated to oxygen will be modest. The results are consistent with no measurable fractionation between the two substances, although the best guess is that the aquo complex will tend to be slightly richer in ^{53}Cr. Chromium near the earth's surface occurs dominantly in the 3+ oxidation state in octahedral coordination with O^{2-} or OH^-, and we suggest that this important class of substances will have relatively homogenous fractionation behavior. We speculate that this may also be true of other metals (i.e., Mg^{+2}, Ti^{+4}, Fe^{+2}, Fe^{3+}, Ni^{+2}) that tend to form octahedral bonding arrangements in oxides, oxy-hydroxides, and aquo complexes. However, the calculated fractionations of POLYAKOV and MINEEV (2000) and measurements by ZHU et al. (2002) do suggest significant fractionations between different Fe^{+2} oxides, and between different Fe^{3+} oxides.

4.4.2. Comparison with Measured Fractionations

Recent measurements by BALL and BASSETT (2000) and ELLIS et al. (2002) on the isotopic composition of dissolved Cr^{6+} (probably either $[CrO_4]^{2-}$ or $[HCrO_4]^-$) in laboratory reduction experiments and natural groundwaters have demonstrated significant fractionations. The results show that Cr^{6+} in groundwater is typically heavier than the NIST SRM 979 standard (which appears to be close to bulk Earth, ELLIS et al., 2002). This is consistent with the predicted tendency of $[CrO_4]^{2-}$ to concentrate heavy Cr-isotopes in natural environments where it is in equilibrium with Cr^{3+}-bearing species. The samples measured by BALL and BASSETT (2000) do not permit a quantitative estimate of actual fractionations, however. ELLIS et al. (2002) performed partial reduction experiments on dissolved Cr^{6+}, using a variety of reducing agents, that clearly show

progressive heavy Cr-isotope enrichment of the remaining Cr^{6+} as more and more is reduced to Cr^{3+}. Using a Rayleigh fractionation model, ELLIS et al. (2002) infer a fractionation of 3.3-3.5‰ between Cr^{6+} and Cr^{3+} species. The calculated equilibrium fractionation is ca. 6.3+1.4/–2.2‰ for $[CrO_4]^{2-}$ vs. $[Cr(H_2O)_6]^{3+}$, and ~7.0±1.4/–2.2‰ for $[CrO_4]^{2-}$ vs. Cr_2O_3, in qualitative agreement with ELLIS et al. (2002). Calculated equilibrium fractionations are larger than the observed fractionations, and the difference appears to be significant relative to uncertainties in the calculations and measurements. It seems unlikely that the discrepancy can be attributed to a difference in the Cr-isotope partitioning behavior of the reduction product in the ELLIS et al. (2002) experiments (likely a oxyhydroxide phase) and Cr_2O_3 or $[Cr(H_2O)_6]^{3+}$. A better explanation might be that the reduction experiments do not achieve isotopic exchange equilibrium, so that the measured fractionations are fundamentally kinetic. If the rate limiting step occurs at an intermediate oxidation state (where bonds are stronger and shorter than in the ultimate Cr^{3+} species), then it would make sense that the observed fractionation would not be quite as large as the equilibrium fractionation. This mechanism would only work if the chemical state of Cr at the rate limiting step were the same (or nearly so) in all of the reduction experiments. It should also be pointed out that the theoretical equilibrium fractionation between $[Fe(H_2O)_6]^{3+}$ and $[Fe(H_2O)_6]^{+2}$, calculated in the same way, also appears to be larger (~5.4‰) than what is observed (~2.8‰) in fractionation experiments designed to approach exchange equilibrium (JOHNSON et al., 2002).

4.4.3. Applications to Natural Systems

One implication of the present study is that large, inorganic Cr-isotope fractionations are most likely to occur at low temperatures, during partial reduction or oxidation

reactions. Because chromium generally prefers to bond with oxygen or hydroxyl in low temperature environments, ligand-exchange effects may not be as important as they are for iron, copper, zinc, and other chalcophile and siderophile metals. Chromium has a strong preference for octahedral coordination in the 3+ oxidation state, and tetrahedral coordination in the 6+ oxidation state. Therefore, changes in coordination number (absent oxidation or reduction) are less likely to drive isotopic fractionations of chromium than of zinc and iron, which commonly occur in both tetrahedral and octahedral coordination environments — or copper, which forms a variety of distorted octahedral, 5-coordinate, and tetrahedral complexes due to the Jahn-Teller effect. These observations suggest that Cr-isotope studies are most likely to be useful in monitoring modern and ancient redox environments.

4.5. Conclusions

We have estimated the equilibrium fractionation behavior of stable Cr-isotopes using published vibrational spectra and both empirical and *ab initio* force-field models. Reduced partition function ratios for chromium isotope exchange (i.e., $1000 \cdot \ln(\beta_{53\text{-}52})$) have been calculated for a number of simple complexes, crystals, and the $Cr(CO)_6$ molecule. Large (> 1‰) fractionations are predicted between coexisting species with differing oxidation states or bond partners. The highly oxidized $[Cr^{6+}O_4]^{2-}$ anion will tend to concentrate ^{53}Cr when in equilibrium with compounds containing Cr^{3+} or Cr^0. Substances containing chromium bonded to strongly bonding ligands like CO or H_2O will concentrate ^{53}Cr relative to compounds with weaker bonds like the $[CrCl_6]^{3-}$ complex. Substances with short Cr-ligand bonds (Cr-C in $Cr(CO)_6$, Cr-O in $[Cr(H_2O)_6]^{3+}$ or $[CrO_4]^{2-}$) will also tend to concentrate ^{53}Cr relative to substances with longer Cr-ligand

bonds ($[Cr(NH_3)_6]^{3+}$, $[CrCl_6]^{3-}$, Cr-metal). These results are very similar to the systematics found in our earlier study of Fe-isotope fractionation.

The calculated equilibrium fractionation between $[CrO_4]^{2-}$ and $[Cr(H_2O)_6]^{3+}$ (or Cr_2O_3) agrees qualitatively with experimental (kinetic?) fractionations associated with the reduction of Cr^{6+} in solution (ELLIS et al., 2002), although the calculated fractionation (~6-7‰ at 298 K) appears to be significantly larger than the experiments suggest (3.3-3.5‰). Our results suggest that natural inorganic Cr-isotope fractionation at the earth's surface will be driven largely by reduction and oxidation processes.

4.6. Bibliography

Adams D. M. and Morris D. M. (1968) Vibrational spectra of halides and complex halides. Part IV. Some tetrahalogenothallates and the effects of d-electronic structure on the frequencies of hexachlorometallates. *J. Chem. Soc. A*, 694-695.

Åkesson R., Pettersson L. G. M., Sandström M., and Wahlgren U. (1994) Ligand field effects in the hydrated divalent and trivalent metal ions of the first and second transition periods. *J. Am. Chem. Soc.* **116**, 8691-8704.

Ball J. W. and Bassett R. L. (2000) Ion exchange separation of chromium from natural water matrix for stable isotope mass spectrometric analysis. *Chemical Geology* **168**, 123-124.

Becke A. D. (1993) Density-functional thermochemistry. III. The role of exact exchange. *J. Chem. Phys.* **98**(5648-5652).

Bell S. and Dines T. J. (2000) An ab initio study of the structures and vibrational spectra of chromium oxo-anions and oxyhalides. *J. Phys. Chem. A* **104**, 11403-11413.

Best S. P., Armstrong R. S., and Beattie J. K. (1980) Infrared metal-ligand vibrations of hexaaquametal(III) ions in alums. *Inorg. Chem.* **19**, 1958-1961.

Bigeleisen J. and Mayer M. G. (1947) Calculation of equilibrium constants for isotopic exchange reactions. *J. chem. Phys.* **15**, 261-267.

Cotton F. A. and Wilkinson G. (1988) *Advanced Inorganic Chemistry*. Wiley-Interscience.

Doclo K., De Corte D., Daul C., and Güdel H.-U. (1998) Ground state and excited stated(sic) properties of hexaamminechromium(III) ion: a density functional study. *Inorg. Chem.* **37**, 3842-3847.

Elcombe M. M. and Hulston J. R. (1975) Calculation of sulphur isotope fractionation between sphalerite and galena using lattice dynamics. *Earth and Planetary Science Letters* **28**, 172-180.

Ellis A. S., Johnson T. J., and Bullen T. D. (2002) Chromium isotopes and the fate of hexavalent chromium in the environment. *Science* **295**, 5562-5565.

Eysel H. H. v. (1972) Hexamminmetal(III)-hexachlorochromate(III): Darstellung, Kristallgitter und Spektren. *Z. anorg. allg. Chem.* **390**, 210-216.

Friedrich G., Fink H., and Seifert H. J. (1987) Über alkali-hexachlorochromate(III): Na_3CrCl_6. *Z. anorg. allg. Chem.* **548**, 141-150.

Gale J. D. (1997) GULP - a computer program for the symmetry adapted simulation of solids. *J. Chem. Soc. Faraday Trans.* **93**, 629-637.

Hay P. J. and Wadt W. R. (1985) *Ab initio* effective core potentials for molecular calculations. Potentials for K to Au including the outermost core orbitals. *J. Chem. Phys.* **82**, 299-310.

Hertwig R. H. and Koch W. (1997) On the parameterization of the local correlation functional. What is Becke-3-LYP? *Chem. Phys. Lett.* **268**(5-6), 345-351.

Johnson C. M., Skulan J. L., Beard B. L., Sun H., Nealson K. H., and Braterman P. S. (2002) Isotopic fractionation between Fe(III) and Fe(II) in aqueous solutions. *EPSL* **195**(1-2), 141-153.

Jonas V. and Thiel W. (1995) Theoretical study of the vibrational spectra of the transition metal carbonyls $M(CO)_6$ [M=Cr, Mo, W], $M(CO)_5$ [M=Fe, Ru, Os], and $M(CO)_4$ [M=Ni, Pd, Pt]. *J. Chem. Phys.* **102**(21), 8474-8484.

Jonas V. and Thiel W. (1999) Symmetry force fields for neutral and ionic transition metal carbonyl complexes from density functional theory. *J. Phys. Chem. A* **103**, 1381-1393.

Jones L. H., McDowell R. S., and Goldblatt M. (1969) Force constants of the hexacarbonyls of chromium, molybdenum, and tungsten from the vibrational spectra of isotopic species. *Inorg. Chem.* **8**(11), 2349-2363.

Kiefer W. and Bernstein H. J. (1972) The resonance Raman effect of the permanganate and chromate ions. *Molecular Physics* **23**(5), 835-851.

Kieffer S. W. (1982) Thermodynamics and lattice vibrations of minerals: 5. Applications to phase equilibria, isotopic fractionation, and high-pressure thermodynamic properties. *Rev. Geophys. Space Phys.* **20**, 827-849.

Kortenkamp A., Casadevall M., Faux S. P., Jenner A., Shayer R. O. J., Woodbridge N., and O'Brien P. (1996) A role for molecular oxygen in the formation of DNA damage during the reduction of the carcinogen chromium(VI) by glutathione. *Arch. Biochem. Biophys.* **329**(2), 199-207.

May T., Strauch D., Schober H., and Dorner B. (1997) Lattice dynamics of Cr_2O_3. *Physica B* **234-236**, 133-134.

Müller A. and Königer F. (1974) Schwingungsspektren von $^{50}CrO_4^{2-}$, $^{53}CrO_4^{2-}$, $Cr^{18}O_4^{2-}$, $^{92}MoO_4^{2-}$, $^{100}MoO_4^{2-}$ und $Ru^{18}O_4^{-}$. Zur Berechnung exakter Kraftkonstanten von Ionen. *Spectrochimica Acta* **30A**, 641-649.

Nakamoto K. (1997) *Infrared and raman spectra of inorganic and coordination compounds*. John Wiley & Sons, Inc.

Parrington J. R., Knox H. D., Breneman S. L., Baum E. M., and Feiner F. (1996) *Chart of the Nuclides*. General Electric Co. and KAPL Inc.

Pearson W. B. (1958) *A handbook of lattice spacings and structures of metals and alloys*. Pergamon Press.

Polyakov V. B. and Mineev S. D. (2000) The use of Mössbauer spectroscopy in stable isotope geochemistry. *Geochimica et Cosmochimica Acta* **64**, 849-865.

Rassolov V. A., Pople J. A., Ratner M. A., and Windus T. L. (1998) 6-31G* basis set for atoms K through Zn. *J. Chem. Phys.* **109**(4), 1223-1229.

Richens D. T. (1997) *The chemistry of aqua ions*. John Wiley & Sons.

Richet P., Bottinga Y., and Javoy M. (1977) A review of hydrogen, carbon, nitrogen, oxygen, sulphur, and chlorine stable isotope fractionation among gaseous molecules. *Ann. Rev. Earth Planet. Sci.* **5**, 65-110.

Rudolph W. W., Mason R., and Pye C. C. (2000) Aluminum(III) hydration in aqueous solution. A Raman spectroscopic investigation and an ab initio molecular orbital study of aluminum(III) water clusters. *Phys. Chem. Chem. Phys.* **2**, 5030-5040.

Schauble E. A., Rossman G. R., and Taylor H. P., Jr. (2001) Theoretical estimates of equilibrium Fe-isotope fractionations from vibrational spectroscopy. *Geochimica et Cosmochimica Acta* **65**, 2487-2497.

Schmidt K. H. and Müller A. (1974) Vibrational spectra and force constants of $[Cr(NH_3)_6]^{3+}$, $[Co(NH_3)_6]^{3+}$, $[Cu(NH_3)_4]^{2+}$, and $[Pd(NH_3)_4]^{2+}$ with $^{50}Cr/^{53}Cr$, $^{63}Cu/^{65}Cu$, $^{104}Pd/^{110}Pd$, and H/D isotopic substitution. *Journal of Molecular Structure* **22**, 343-352.

Schmidt M. W., Baldridge K. K., Boatz J. A., Elbert S. T., Gordon M. S., Jensen J. J., Koseki S., Matsunaga N., Nguyen K. A., Su S., Windus T. L., Dupuis M., and Montgomery J. A. (1993) General atomic and molecular electronic-structure system. *J. Comput. Chem.* **14**, 1347-1363.

Schober H., May T., Dorner B., Strauch D., Steigenberger U., and Morrii Y. (1995) Lattice dynamics of Cr_2O_3. *Z. Phys. B* **98**, 197-205.

Schober H., Strauch D., and Dorner B. (1993) Lattice dynamics of sapphire (Al_2O_3). *Z. Phys. B* **92**, 273-283.

Shaw W. M. and Muhlestein L. D. (1971) Investigation of the phonon dispersion relations of chromium by inelastic neutron scattering. *Physical Review B* **4**(3), 969-973.

Tarte P. and Preudhomme J. (1970) *Spectrochimica Acta* **26A**, 2207-?

Tevault D. and Nakamoto K. (1975) Matrix isolation and computer simulation spectra of $Cr(CO)_6$ and $Mo(CO)_6$. *Inorg. Chem.* **14**(10), 2371-2373.

Trampenau J., Petry W., and Herzig C. (1993) Temperature dependence of the lattice dynamics of chromium. *Physical Review B* **47**(6), 3132-3137.

Urey H. C. (1947) The thermodynamic properties of isotopic substances. *J. Chem. Soc.*, 562-581.

Zhu X. K., Guo Y., Williams R. J. P., O'Nions R. K., Matthews A., Belshaw N. S., Canters G. W., de Waal E. C., Weser U., Burgess B. K., and Salvato B. (2002) Mass fractionation processes of transition metal isotopes. *EPSL **in press***.

Appendix. Notes on Vibrational Spectroscopy and Prediction of Frequency Shifts

A-1.1. [$Cr^{3+}Cl_6$]$^{3-}$

The hexachloro complex is among the simplest studied, it is octahedral (with O_h symmetry) and has only 7 atoms. This complex is modeled using a simplified, empirical Modified Urey-Bradley Force field (MUBFF) that has been optimized to match the observed vibrational frequencies. The complex has five distinct measurable vibrational modes, overconstraining the 3-parameter MUBFF. The resulting force field is accurate to within ~10 % for all of the input frequencies, and is within a few % for the v_1 and v_3 stretching modes. The quality of this result is similar to MUBFF results on other halogeno complexes (SCHAUBLE et al., 2001). A uniform atomic mass of 35.453 amu is assumed for all chlorine atoms (PARRINGTON et al., 1996).

A-1.2. [$Cr^{3+}(NH_3)_6$]$^{3+}$

Force-field models for hexaamminechromium(III) use the point-mass approximation, which means that each complexed NH_3 group is assumed to behave as a single point mass. By making this assumption it is possible to treat the 25-atom complex as a much simpler 7-"atom" structure just like hexachlorochromium(III). The point-mass approximation is possible because N-H stretching and bending modes vibrate at much higher frequencies than Cr-N stretching and bending modes, and the two types of motion are expected to be more or less independent of each other. This assumption is supported by measurements on [$^{50}Cr^{III}(NH_3)_6$]$^{3+}$ and [$^{53}Cr^{III}(NH_3)_6$]$^{3+}$, which show that only two vibrational modes are sensitive to Cr-isotope substitution (SCHMIDT and MÜLLER, 1974). Measured spectra for [$Co^{III}(NH_3)_6$]$^{3+}$ and [$Co^{III}(ND_3)_6$]$^{3+}$ also show a clear distinction

between the infrared active NH_3-rocking and internal vibrations (which are highly H-isotope sensitive) and the modestly H-isotope sensitive Co-N stretching vibrations (SCHMIDT and MÜLLER, 1974). In addition to a MUBFF force field, we have applied the empirical force field of SCHMIDT and MÜLLER (1974).

SCHMIDT and MÜLLER (1974) measured Cr-isotope shifts for both Cr-isotope sensitive vibrations in $[Cr^{III}(NH_3)_6]^{3+}$, so it is possible to calculate the reduced partition function ratio from experimental data alone. Measured shifts in vibrational frequencies resulting from ^{50}Cr-^{53}Cr substitution are scaled by 1/3 to give an estimate of the effects of ^{52}Cr-^{53}Cr substitution.

A-1.3. $[Cr^{3+}(H_2O)_6]^{3+}$

The hexaaquo complex is modeled using both empirical and *ab initio* force fields. We originally calculated *ab initio* force fields in much the same way as for $Cr(CO)_6$ and $[CrO_4]^{2-}$, treating the $[Cr(H_2O)_6]^{3+}$ complex as a gas-phase molecule of T_h symmetry. An important shortcoming of these models is that calculated vibrational frequencies are 13% to 30% lower than measured frequencies. In addition, calculated Cr-O bond lengths are somewhat longer than measurements suggest, 2.003 (B3LYP/LANL2DZ) - 2.025 Å (HF/6-31G*) vs. 1.96 - 1.98 Å (meas.)(RICHENS, 1997). Similar behavior has been observed in *ab initio* studies of other cationic complexes (e.g., ÅKESSON et al., 1994; DOCLO et al., 1998; RUDOLPH et al., 2000). Although the calculated ratios of vibrational frequencies in isotopically substituted forms of the complex are similar to those calculated with empirical force fields, a better *ab initio* model is clearly desirable. Significant improvement comes from explicitly including at least a second sphere of solvent molecules to accept hydrogen bonds from the H_2O molecules directly bound to

the central metal ion (ÅKESSON et al., 1994). Here we follow the approach of RUDOLPH et al. (2000), including an explicit second solvation sphere consisting of 12 H_2O molecules (further lowering the symmetry of the cluster to T), each accepting one hydrogen bond from a Cr-bound water molecule. After including the 12 additional H_2O molecules, model Cr-O bond lengths are shortened by ~0.02 Å, and vibrational frequencies become much closer to measured values. Vibrations of the second-sphere water molecules are separated from vibrations of the $[Cr(H_2O)_6]^{3+}$ core by setting the masses of atoms in the outer sphere to be very large (9000 amu). One important consequence of the lowered symmetry of the $[Cr(H_2O)_6]^{3+} \cdot 12H_2O$ complex is mixing of the three triply-degenerate O-Cr-O bending vibrations (v_4 - v_6). Reduced partition function ratios are calculated using the ratio $(^{53}v_{Bend\#1} *^{53}v_{Bend\#2} *^{53}v_{Bend\#3}) / (^{52}v_{Bend\#1} *^{52}v_{Bend\#2} *^{52}v_{Bend\#3})$ and the measured frequency of v_4 (BEST et al., 1980). There is little mixing between Cr-O skeletal vibrations and the Cr-OH$_2$ rocking, wagging, and twisting vibrations, so the latter are predicted to be only slightly sensitive to Cr-isotope substitution, and are ignored for the purpose of calculating reduced partition function ratios. For this reason, tabulated shifts calculated with *ab initio* force fields do not strictly obey the Redlich-Teller Product Rule.

Empirical force fields use the point mass approximation for complexed H_2O molecules, ignoring O-H stretching, bending, and Cr-O-H deformational modes. As was the case with hexaamminechromium(III) above, the point mass approximation allows the complex to be treated with a simple 3-parameter MUBFF. It is justified by the large difference between measured Cr-O stretching and O-Cr-O bending frequencies (~200-560 cm^{-1}) and O-H stretching and H-O-H bending frequencies (> 1000 cm^{-1}). *Ab initio* models and measurements suggest that there is only one strongly Cr-isotope sensitive

frequency above 400 cm^{-1} (BEST et al., 1980), further supporting the point mass approximation. (BEST et al., 1980) measured the effects of Cr-isotope substitution on vibrational frequencies in both $[^{50}Cr(H_2O)_6]^{3+}$ and $[^{53}Cr(H_2O)_6]^{3+}$, so it is possible to calculate a reduced partition function ratio without using a force field. However, the product of isotopic frequencies ($^{53}v_3 \cdot {}^{53}v_4$)/ ($^{50}v_3 \cdot {}^{50}v_4$) measured by BEST et al. (1980) is ~0.9881, much closer to one than the Redlich-Teller Product Rule value of ~0.9805. This strongly suggests that not all of the Cr-isotope sensitive frequencies were identified, and explains why the reduced partition function ratio calculated with measured shifts is so much lower than other models. In this respect, the point-mass approximation is open to question. Note that measured spectra only extend down to ca. 300 cm^{-1}, and would miss lower-frequency Cr-isotope sensitive bending vibrations. The measured shifts are scaled by 1/3 to estimate ^{52}Cr-^{53}Cr shifts.

A-1.4. $[Cr^{6+}O_4]^{2-}$

The tetrahedral $[CrO_4]^{2-}$ anion is modeled using two empirical force fields: a MUBFF and a generalized force field based on measured spectra of $[^{50}CrO_4]^{2-}$ and $[^{53}CrO_4]^{2-}$ (MÜLLER and KÖNIGER, 1974).Three *ab initio* force fields, calculated at the HF/6-31G*, B3LYP/LANL2DZ, and B3LYP/6-31G* levels, and a semi-empirical force field based on a scaled B3LYP/LANL2DZ model (BELL and DINES, 2000) are also used to calculate frequencies for $[^{53}CrO_4]^{2-}$.

MÜLLER and KÖNIGER (1974) measured Cr-isotope sensitive vibrational frequencies in both $[^{50}CrO_4]^{2-}$ and $[^{53}CrO_4]^{2-}$, and it is possible to calculate a reduced partition function ratio without using a force field. The measured shifts are scaled by 1/3 to estimate ^{52}Cr-^{53}Cr shifts.

A-1.5. $Cr^0(CO)_6$

Chromium hexacarbonyl is modeled using a variety empirical and *ab initio* force fields. This molecule is octahedral (O_h symmetry), and has four Cr-isotope sensitive vibrational modes (these are infrared-active and belong to the F_{1u} group). Two empirical force fields (JONES et al., 1969; TEVAULT and NAKAMOTO, 1975), and one *ab initio* force field (JONAS and THIEL, 1999) have been published. In addition, we have calculated new *ab initio* force fields at the HF/6-31G*, B3LYP/LANL2DZ, and B3LYP/6-31G* levels.

A-1.6. Metallic chromium (Cr-metal)

The vibrational spectrum of Cr-metal has been extensively studied by inelastic neutron scattering. (i.e., SHAW and MUHLESTEIN, 1971; TRAMPENAU et al., 1993). Cr-metal has a body-centered cubic structure with one chromium atom per primitive unit cell. Vibrational (phonon) frequencies in metallic chromium are low, topping out at ~330 cm^{-1}. The phonon density of states model of TRAMPENAU et al. (1993) is used to calculate a reduced partition function ratio for Cr-isotope exchange in metallic chromium. Observed spectra are assumed to represent the ^{52}Cr-endmember, frequencies for ^{53}Cr-metal are calculated by applying a uniform shift equal to $[m(^{52}Cr)/m(^{52}Cr)]^{1/2}$ (≈ 0.99051) to the model spectrum for ^{52}Cr-metal.

A-1.7. $Cr^{3+}_2O_3$

The vibrational spectrum of Cr_2O_3 has been studied by SCHOBER et al. (1993) and (MAY et al., 1997), using inelastic neutron scattering techniques. Cr_2O_3 is structurally analogous to corundum, each chromium atom is bound to six oxygen atoms in a distorted octahedral arrangement. Both lattice-dynamics studies provide dynamical (force-field) models optimized to measured frequencies. The model of MAY et al. (1997) is apparently

based on a larger set of measurements, but is also essentially identical to a third model presented in the older SCHOBER et al. (1993) work. Both lattice dynamics models were used to calculate reduced partition function ratios, based on vibrational frequencies in pure ^{52}Cr- and ^{53}Cr-endmember crystals. Lattice-dynamics calculations are made using GULP, the General Utility Lattice Program (GALE, 1997). Reduced partition function ratios are calculated from the Helmholtz free energies of ^{35}Cl- and ^{37}Cl-endmember compositions using eqn. 15 of KIEFFER (1982). Phonon frequencies were sampled at discrete wavevectors in the symmetrically irreducible subspace of the Brillouin zone. It was found that the calculated change in the Helmholtz free energy due to isotope substitution converged very rapidly as the number of sampling points increased, varying by no more than $2*10^{-3}$ J/mol for runs with 10-200 sampling points. The resulting error in a calculated reduced partition function ratio is ~0.001‰ at 298 K, indicating that numerical integration is not a significant source of uncertainty. This agrees with earlier modeling of Cl-isotope fractionation in alkali chlorides (Schauble et al. *in prep.*), and the study of ELCOMBE and HULSTON (1975) on sulfur isotope fractionation between sphalerite (ZnS) and galena (PbS). For the present study, roughly 50 wave vectors were sampled to calculate each reduced partition function ratio.

Table 4.1. Vibrational frequencies and frequency ratios used to calculate reduced partition function ratios of Cr-bearing complexes and molecules.

$[CrCl_6]^{3-}$
$^{52}\nu_3$ (F_{1u}) = 315 cm^{-1}, $^{52}\nu_4$ (F_{1u}) = 199 cm^{-1} (EYSEL, 1972)

Model	$^{53}\nu_3/^{52}\nu_3$	$^{53}\nu_4/^{52}\nu_4$
MUBFF	0.99494	0.99742

$[Cr(NH_3)_6]^{3+}$
$^{52}\nu_3$ (F_{1u}) = 470 cm^{-1}, $^{52}\nu_4$ (F_{1u}) = 270 cm^{-1} (SCHMIDT and MÜLLER, 1974)

Model	$^{53}\nu_3/^{52}\nu_3$	$^{53}\nu_4/^{52}\nu_4$
MUBFF	0.99666	0.99705
[1]Schmidt & Müller FF	0.99724	0.99647
Obs.[*]	0.99715	0.99627

$[Cr(H_2O)_6]^{3+}$
$^{52}\nu_3$ (F_{1u}) = 555 cm^{-1}, $^{52}\nu_4$ (F_{1u}) = 329 cm^{-1} (BEST et al., 1980)

Model	$^{53}\nu_3/^{52}\nu_3$	$^{53}\nu_4/^{52}\nu_4$
MUBFF	0.99636	0.99723
HF/6-31G*	0.99659	0.99760
B3LYP/LANL2DZ	0.99637	0.99803
B3LYP/6-31G*	0.99642	0.99768
Obs.*	0.99701	0.99899

$[CrO_4]^{2-}$
$^{52}\nu_3$ (F_2) = 890 cm^{-1}, $^{52}\nu_4$ (F_2) = 368 cm^{-1}

Model	$^{53}\nu_3/^{52}\nu_3$	$^{53}\nu_4/^{52}\nu_4$
MUBFF	0.99731	0.99745
[2]Bell & Dines FF	0.99671	0.99806
[3]Müller & Königer FF	0.99694	0.99782
HF/6-31G*	0.99655	0.99822
B3LYP/LANL2DZ	0.99673	0.99805
B3LYP/6-31G*	0.99669	0.99809
Obs.[*]	0.99681	0.99808

Cr(CO)$_6$
$^{52}\nu_6$ (F_{1u}) = 2043 cm^{-1}, $^{52}\nu_7$ (F_{1u}) = 671 cm^{-1}, $^{52}\nu_8$ (F_{1u}) = 447 cm^{-1},
$^{52}\nu_9$ (F_{1u}) = 97 cm^{-1} (JONES et al., 1969)

Model	$^{53}\nu_6/^{52}\nu_6$	$^{53}\nu_7/^{52}\nu_7$	$^{53}\nu_8/^{52}\nu_8$	$^{53}\nu_9/^{52}\nu_9$
[4]Jones et al. FF	1.0	0.99603	0.99787	0.99885
[5]Tevault & Nakamoto FF	1.0	0.99670	0.99728	0.99877
[6]Jonas & Thiel FF	1.0	0.99615	0.99811	0.99849
HF/6-31G*	1.0	0.99710	0.99710	0.99854
B3LYP/LANL2DZ	1.0	0.99607	0.99820	0.99850

B3LYP/6-31G*	1.0	0.99620	0.99803	0.99842

[1] (SCHMIDT and MÜLLER, 1974)
[2] (BELL and DINES, 2000)
[3] (MÜLLER and KÖNIGER, 1974)
[4] (JONES et al., 1969)
[5] (TEVAULT and NAKAMOTO, 1975)
[6] (JONAS and THIEL, 1999)

Table 4.2. Calculatd reduced partition function ratios $1000 \cdot \ln(\beta_{53-52})$ for ^{53}Cr-^{52}Cr exchange at various temperatures. The best guess model (either B3LYP/6-31G* or MUBFF) for each substance is indicated in bold type. Results are nearly linear functions of $1/T^2$, and linear interpolation with respect to $1/T^2$ is accurate to < 0.1‰ for temperatures between those reported.

Substance	Model	0°C	25°C	100°C	300°C
$[CrCl_6]^{3-}$					
	MUBFF	**4.0**	**3.4**	**2.2**	**0.9**
$[Cr(NH_3)_6]^{3+}$					
	MUBFF	**6.1**	**5.2**	**3.4**	**1.5**
	[1]Schmidt & Müller FF	5.6	4.7	3.1	1.3
	Obs.*	5.7	4.9	3.2	1.4
$[Cr(H_2O)_6]^{3+}$					
	MUBFF	8.8	7.5	5.0	2.2
	HF/6-31G*	8.1	6.9	4.6	2.0
	B3LYP/LANL2DZ	8.2	7.0	4.6	2.0
	B3LYP/6-31G*	**8.4**	**7.2**	**4.7**	**2.1**
	Obs.*	6.4	5.4	3.6	1.6
$[CrO_4]^{2-}$					
	MUBFF	13.4	11.6	7.9	3.6
	[2]Bell & Dines FF	15.4	13.4	9.1	4.2
	[3]Müller & Königer FF	14.6	12.7	8.7	4.0
	HF/6-31G*	15.9	13.8	9.4	4.3
	B3LYP/LANL2DZ	15.3	13.3	9.1	4.2
	B3LYP/6-31G*	**15.5**	**13.4**	**9.2**	**4.2**
	Obs.*	15.1	13.1	8.9	4.1
$Cr(CO)_6$					
	[4]Jones et al. FF	13.2	11.3	7.6	3.4
	[5]Tevault & Nakamoto FF	12.2	10.5	7.0	3.1
	[6]Jonas & Thiel FF	12.6	10.8	7.2	3.2
	HF/6-31G*	11.4	9.8	6.5	2.9
	B3LYP/LANL2DZ	12.7	10.9	7.3	3.2
	B3LYP/6-31G*	**12.6**	**10.8**	**7.2**	**3.2**
Cr-Metal					
	[7]Trampenau et al. FF	4.1	3.4	2.2	0.9
Cr_2O_3					
	[8]Schober et al. FF	7.2	6.1	4.0	1.7
	[9]May et al. FF	8.0	6.8	4.5	2.0

[1] (SCHMIDT and MÜLLER, 1974)
[2] (BELL and DINES, 2000)
[3] (MÜLLER and KÖNIGER, 1974)
[4] (JONES et al., 1969)
[5] (TEVAULT and NAKAMOTO, 1975)
[6] (JONAS and THIEL, 1999)

[7] (TRAMPENAU et al., 1993)
[8] (SCHOBER et al., 1995)
[9] (MAY et al., 1997)

Figure 4.1 Calculated reduced partition function ratios for ^{53}Cr-^{52}Cr exchange [$1000 \cdot \ln(\beta_{53-52})$] as a function of temperature from 273-573 K (0-300°C). Best-guess models (B3LYP/6-31G* or MUBFF) are shown with solid lines, lightly shaded fields show the range of models for each substance. Darker shaded field shows the range of two lattice-dynamics models for Cr_2O_3.

134

Fig. 4.1

$[CrO_4]^{2-}$

$Cr(CO)_6$

$[Cr(H_2O)_6]^{3+}$
Cr_2O_3

$[Cr(NH_3)_6]^{3+}$

Cr-Metal
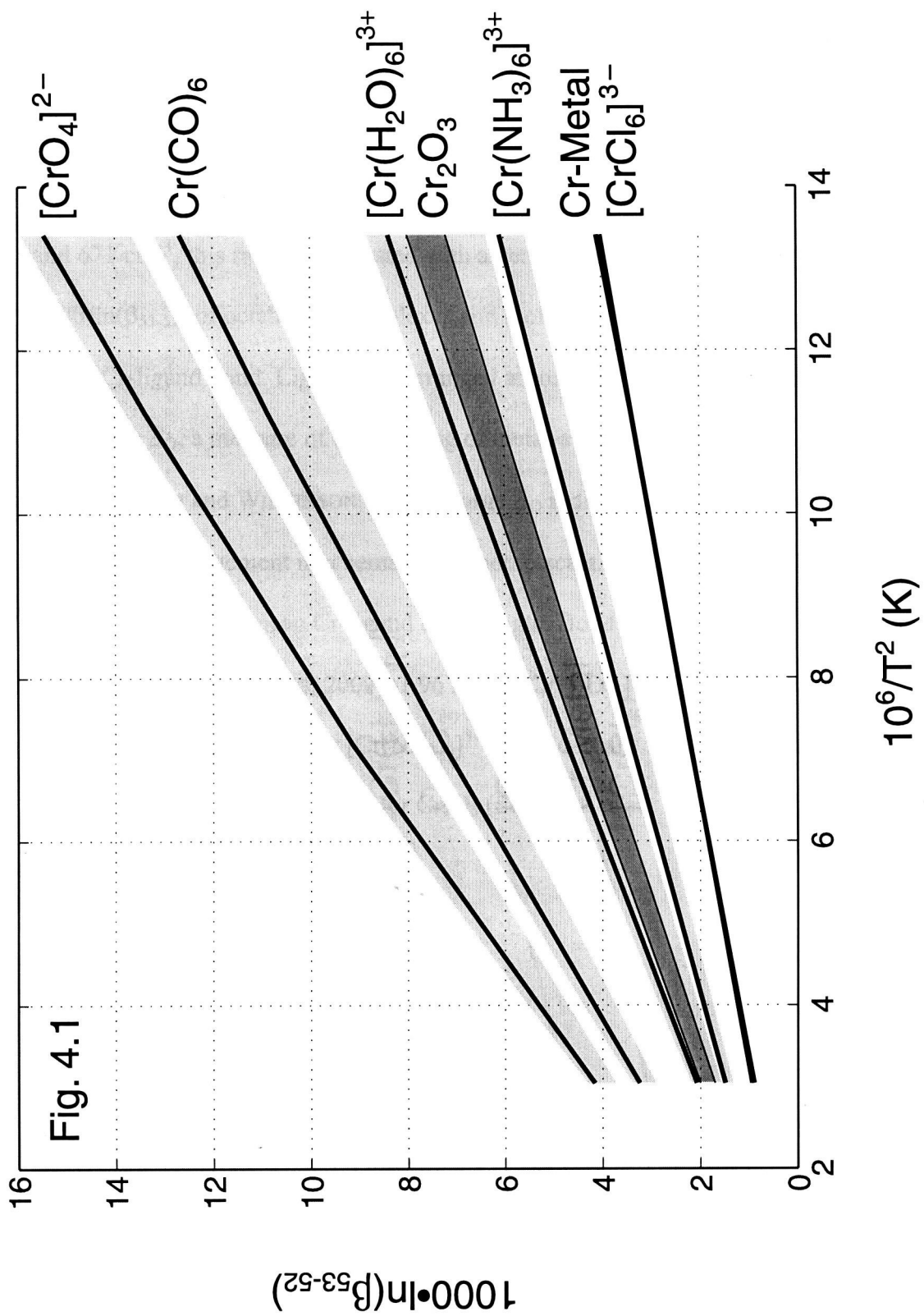$[CrCl_6]^{3-}$

$1000 \cdot \ln(\beta_{53-52})$

$10^6/T^2$ (K)

Figure 4.2 Correlation between calculated reduced partition function ratios and spectroscopic and chemical properties. a) Asymmetric Cr-ligand stretch (ν_3) frequency vs. $1000 \cdot \ln(\beta_{53\text{-}52})$ for chloro-, ammino-, aquo-, and oxo-complexes and hexacarbonyl molecule from Table 4.2. The Cr-C stretch in $Cr(CO)_6$ is split between modes at 447 cm^{-1} and 671 cm^{-1}, this range is indicated with a vertical bar. b) Variation in calculated $1000 \cdot \ln(\beta_{53\text{-}52})$ of octahedral complexes and molecules with increasing covalent strength of the Cr-ligand bond. Ligands are arranged according to the spectrochemical series of increasing Δ_O, a measure of the splitting of metal-atom d-orbitals caused by the ligand field (COTTON and WILKINSON, 1988). Large Δ_O indicates strong, covalent metal-ligand bonds. The arrangement is schematic and not to scale. c) Variation in calculated $1000 \cdot \ln(\beta_{53\text{-}52})$ with mean Cr-ligand bond length. Bond lengths used are 1.65 Å for $[CrO_4]^{2-}$ (BELL and DINES, 2000), 1.96 Å for $[Cr(H_2O)_6]^{3+}$, 1.915 Å for $Cr(CO)_6$ (JONAS and THIEL, 1995), 2.07 Å for $[Cr(NH_3)_6]^{3+}$ (DOCLO et al., 1998), 2.35 Å for $CrCl_6$ (FRIEDRICH et al., 1987), 1.99 Å for Cr_2O_3 (SCHOBER et al., 1995), and 2.49 Å for Cr-metal (PEARSON, 1958).

Fig. 4.2.
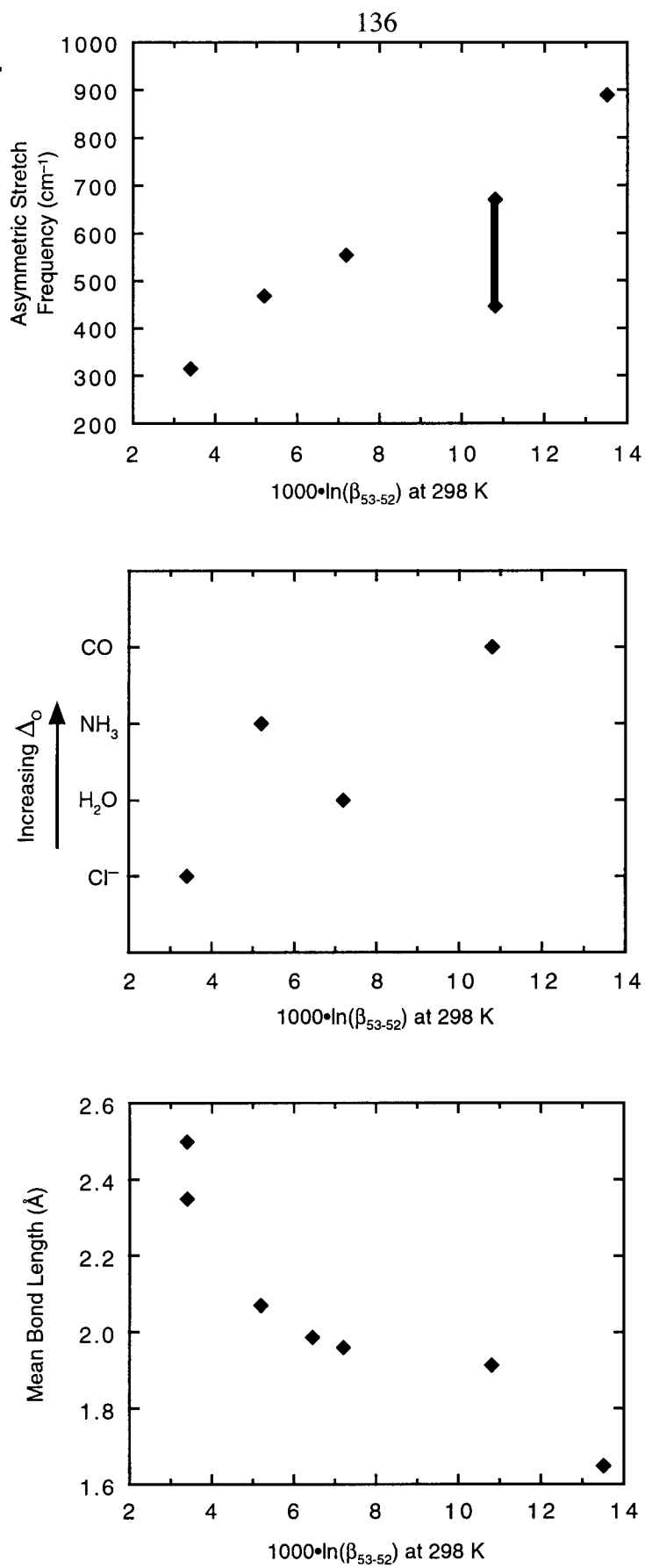
Chapter 5. Oxygen-isotope compositions of Mesozoic and Cenozoic granitoids of the northeastern Great Basin, Nevada and Utah, and their relationship to radiogenic isotopes

$^{18}O/^{16}O$ ratios of granitoid plutons from NE Nevada and NW Utah indicate systematic involvement of different source rocks during each of three stages of magmatism in this region during the Late Jurassic, Late Cretaceous, and mid-Cenozoic. The temporal variation in magmatic sources is particularly evident when oxygen isotope data are combined with radiogenic-isotope data previously obtained on these same plutons. Late Cretaceous (90-70 Ma) granites have elevated whole-rock $\delta^{18}O$ (+9.3 to + 12.1) and $^{87}Sr/^{86}Sr_i$ (0.711 to 0.734), and low εNd (-13 to -23) suggestive of a source dominated by evolved crustal rocks. However, the 170-150 Ma late Jurassic plutons in this region span an even larger range of $\delta^{18}O$ values (+7.2 to +13.2), despite having Sr and Nd isotopic compositions that are much less "crustal" ($^{87}Sr/^{86}Sr_i$ = 0.705 to 0.711, εNd = -2.5 to -6.5) than the Late Cretaceous plutons. The wide range of $^{18}O/^{16}O$ in the Jurassic granitoids strongly suggests moderate to extensive (typically 20% - 40%) mixing or assimilation of high-$\delta^{18}O$ sedimentary rocks into a more mafic parent melt. The 40-25 Ma Cenozoic plutons ($\delta^{18}O$ = +7.0 to +9.7, $^{87}Sr/^{86}Sr_i$ = 0.707 to 0.717, εNd = -13.2 to -26.3) indicate melting of the continental basement, which may also be a secondary component in the Late Cretaceous suite. Unlike Jurassic granitoids, which show no obvious correlation between geography and $\delta^{18}O$, the 40-25 Ma Cenozoic plutons can be subdivided into a higher $\delta^{18}O$ (+8.6 to +9.7) southern group and a lower $\delta^{18}O$ (+7.0 to +8.2) northern group across a well-defined Crustal Age Boundary (CAB) that extends roughly eastward from Elko, Nevada; this CAB coincides with WRIGHT and

WOODEN (1991)'s Upper Array - Lower Array isotope boundary, as well as with the approximate southern limit of exposure of Archean basement. The low $\delta^{18}O$ values and depleted lead isotope compositions of the Lower Array (northern) samples indicate that Archean age basement is present beneath a large area of the most northeasterly part of the Great Basin. Based on the high $\delta^{18}O$ of some Jurassic plutons compared to the Late Cretaceous suite, we speculate that the $\delta^{18}O$ of the metasedimentary section in this area may have dropped by 2–3 per mil as a result of fluid-rock interaction sometime between the Jurassic and Late Cretaceous magmatic episodes.

5.1. Introduction

5.1.1. Aim of Study

The goal of the present study is to measure whole-rock oxygen-isotope variations in Mesozoic and Cenozoic granitoid plutons from the northeastern Great Basin in order to examine the possible correlations between $\delta^{18}O$, intrusion ages, radiogenic isotope compositions, and apparent magmatic sources determined on many of the same samples by WRIGHT and WOODEN (1991). The study area lies between the Roberts Mountains Thrust and the Sevier Thrust Belt (Fig. 5.1.). The new oxygen-isotope data provide a much denser and more systematic sampling of the three main episodes of granitoid magmatism in this region than has been heretofore available, thereby allowing a finer discrimination between temporal and geographic controls on magmatic processes.

5.1.2. Geologic Setting

In the northeastern Great Basin the crustal section is dominated by the thick (> 10 km) Proterozoic to Paleozoic Cordilleran Miogeocline, composed of a lower portion rich

in continentally derived siliciclastic rocks and an upper, carbonate-rich section. North of about 41° N, the underlying basement appears to contain Archean-age rocks, whereas farther south early Proterozoic basement may be dominant (BENNETT and DEPAOLO, 1987).

Over the past 200 Ma, three major episodes of granitic magmatism have been documented in this area (Fig. 5.1). These discrete events (Late Jurassic, 170 - 150 Ma; Late Cretaceous, 90 - 70 Ma; and middle Cenozoic, 40 - 25 Ma) are separated by substantial intervals during which magmatism was sparse or absent (BARTON et al., 1988; ELISON, 1995). Late Jurassic granitoids are generally metaluminous to slightly alkalic, and were intruded at a range of depths (MILLER and HOISCH, 1995); compositions include monzodiorite, monzonite, quartz monzonite, granodiorite, and monzogranite, as well as true (two-mica) granite. The Late Cretaceous suite, mainly peraluminous two-mica granite, is commonly exposed in metamorphic core-complexes such as in the Ruby Mountains and Southern Snake Range (BARTON, 1990), mostly south of the latitude of Elko, Nevada (Figs. 5.1 and 5.2). The Cenozoic plutons are dominantly monzogranite, granite, and quartz diorite (WRIGHT and WOODEN, 1991).

5.1.3. Previous Work

Early regional isotopic investigations of Mesozoic and Cenozoic plutonism in the Great Basin found correlations between geography and isotopic composition (FARMER and DEPAOLO, 1983; LEE et al., 1981a; SOLOMON and TAYLOR, 1989; ZARTMAN, 1974). The latter two studies were particularly concerned with determining the composition and regional extent of the crustal protoliths of these granitoid magmas. FARMER and DEPAOLO (1983) used Sr and Nd isotope data to delineate the possible source rocks: from

west to east (Fig. 5.1), they identified the eugeocline (EG), a transition zone (TZ), the

miogeocline and its underlying Rb-undepleted basement (MG), and the Rb-depleted

craton (CG). They further divided miogeoclinal granitoids into peraluminous (MG_p) and

metaluminous (MG_m) subsets, which is effectively an age separation as well, in that the

MG granite samples of Late Cretaceous age belong to the MG_p suite, whereas the

Jurassic and Cenozoic granitoid samples are classified as MG_m. The EG - TZ boundary

closely corresponds to the $^{87}Sr/^{86}Sr_i$ = 0.706 line of KISTLER and PETERMAN (1973).

SOLOMON and TAYLOR (1989), utilizing combined radiogenic and oxygen isotope data,

and including many of the same samples analyzed by FARMER and DEPAOLO (1983),

defined four essentially analogous magmatic source zones, as indicated in Figure 5.1.

More recent studies (BARTON, 1990; ELISON, 1995; ELISON et al., 1990; WRIGHT

and WOODEN, 1991) have extended early local studies of LEE et al. (1982), and LEE and

CHRISTIANSEN (1983) in focusing on the time evolution of Great Basin magmatic

sources. Significantly, BARTON (1990) and WRIGHT and WOODEN (1991) found that the

"geographic" isotope zones of earlier studies overlap in the plutons of eastern Nevada

and western Utah, with apparently mantle-derived or primitive granitoids interspersed

among highly aluminous granitoids derived from evolved crustal sources. Thus, rather

than being strongly correlated with geographic location, the chemical and isotopic

compositions of plutons in the northeastern Great Basin appear to correlate most strongly

with the age of intrusion. For examples, the metaluminous Jurassic plutons differ from

the dominantly peraluminous Late Cretaceous suite in having lower $^{87}Sr/^{86}Sr_i$ (0.705 -

0.711 vs. 0.711 - 0.740) and distinctly higher εNd (0 to -7 vs. -15 to -24). There are few

(if any) granitoids that are isotopically intermediate between the characteristic Jurassic

plutons and the Late Cretaceous plutons, nor are there any intermediate-age granitoids emplaced between ~145 Ma and 90 Ma in the northeastern Great Basin; this age interval roughly corresponds to the onset of Sevier thrusting. These data suggest that there was less involvement of continental or continentally derived crustal material during the Jurassic episode. WRIGHT and WOODEN (1991) argue that the sharply increased crustal isotopic signature that appears in the Late Cretaceous suite, following a magmatic hiatus of about 50 million years, implies that this younger suite of plutons formed by anatectic melting of thickened crust.

Mid-Cenozoic plutons in this region display a distinctive isotopic signature: the low εNd (-13 to -30), moderate $^{87}Sr/^{86}Sr_i$ (0.707 to 0.718), and relatively unradiogenic lead isotope values all indicate a major source component of deep, high-grade, ancient continental crystalline basement. Isotopically, Cenozoic plutons north of about 40' 40' differ from plutons of the same age farther south. An Upper Array-Lower Array lead isotope boundary was defined by WRIGHT and WOODEN (1991) based on these differences , with the more northerly Cenozoic granitoids of the Lower Array containing distinctly less radiogenic lead than those of the Upper Array, as well as having lower $^{87}Sr/^{86}Sr_i$ and εNd. The geographic expression of this boundary, here termed the Crustal Age Boundary (CAB), separates our samples into a northern and a southern subgroup (Figs. 5.1 and 5.2). The CAB geographic boundary passes near the Ruby - East Humboldt Range junction a few kilometers south of Secret Pass, lying somewhere between the Egan and Deep Creek Ranges on the south and the Toana, Pilot, and Grouse Creek Ranges to the north. In the western part of the study area, the CAB coincides well with the southern limit of exposure of Archean basement rocks; however, to the east these two features

appear to diverge, as the CAB trends southeastwards, whereas the limit of Archean exposure trends northeast.

5.1.4. Sources of Isotopic Data

Mesozoic and Tertiary granitoid samples within the study area that were previously analyzed by WRIGHT and WOODEN (1991), FARMER and DEPAOLO (1983),LEE et al. (1982), and LEE and CHRISTIANSEN (1983) are also incorporated into our data set. These include samples from six Jurassic, two Late Cretaceous, and three Cenozoic plutons in addition to those analyzed in the present study, as well as a number of overlapping samples. For plotting purposes, some simplifications of these additional data have been necessary; for example, LEE and CHRISTIANSEN (1983) found a range of $\delta^{18}O$ values for the Snake Creek - Williams Canyon pluton, but for present purposes a single "parent magma" value of +11.0 is used. We have not plotted Ruby Mountain samples RM 47-66 and RM 17-66 (FARMER and DEPAOLO, 1983) because of their uncertain ages (HUDEC, 1992), and sample NV-CC- I (FARMER and DEPAOLO, 1983), from the Oligocene Cherry Creek Stock in the Egan Range, which SOLOMON (1989) concluded was probably hydrothermally altered.

GRUNDER and WICKHAM (1991) and GRUNDER (1992) have reported $\delta^{18}O$, $^{87}Sr/^{86}Sr_i$, ϵNd, and Pb-isotope data for a number of mid-Tertiary volcanic rocks in the southern part of the study area. The isotopic and compositional patterns are similar to nearby intrusive rocks of the same age, spanning a somewhat larger range in $\delta^{18}O$ and wt. % SiO,. These are not formally included in our data set but are considered in the discussion.

5.2. Analytical Methods

Whole-rock $^{18}O/^{16}O$ was measured using conventional extraction techniques, using F_2 as a reagent. After conversion to CO_2 the $\delta^{18}O$ of each sample was determined using a Finnigan MAT 252 gas-source mass spectrometer, and the $\delta^{18}O$ was corrected to Standard Mean Ocean Water (i.e., SMOW) using simultaneously analyzed aliquots the Caltech Rose Quartz #I and #V standards; the $\delta^{18}O$ of these standards, +8.45 and +8.19 respectively, correspond to NBS-28 = +9.60. The expected error on these conventional analyses is ±0.2‰; nine of eleven duplicate measurements of whole-rock powders reported here were within 0.3‰ of the first measurement, the largest difference was 0.53‰, and the mean difference was 0.18‰.

Because of their altered appearances and/or descriptions of nearby hydrothermal activity, quartz and feldspar separates from three samples (Secret Peak, Toano Springs, and the Miner's Spring Granite) were measured to check for possible oxygen isotope effects resulting from subsolidus alteration (e.g., as a result of a post-emplacement meteoric-hydrothermal episode). The Secret Peak and Toano Springs samples do indeed display large (> 3 per mil) quartz-feldspar fractionations, suggesting that the feldspar has preferentially exchanged with a low-$\delta^{18}O$ fluid. In the case of the Toano Springs pluton, the magmatic whole-rock $\delta^{18}O$ is estimated to be ~+9.3 by subtracting 1.2 per mil from the measured quartz $\delta^{18}O$ of +10.5. The $\delta^{18}O$ of quartz in the Secret Peak granite is so low (+6) that it appears likely that even the quartz was affected by open-system subsolidus exchange, and we do not attempt to calculate a magmatic whole-rock $\delta^{18}O$ for this sample. The Miner's Spring Granite has a small quartz-feldspar fractionation of ~0.5‰ suggesting that any open-system subsolidus exchange effects are minor.

Because the Secret Peak and Toano Springs samples show evidence of subsolidus oxygen exchange with low $\delta^{18}O$ fluids, it was decided to check for hydrothermal effects in less obviously altered samples. To this end, quartz (or hornblende) separates were analyzed from twelve additional samples (Contact, CI-72, CI-71, CI-65, RM-1, White Horse, RM-4, Lexington Creek, Red Butte, Uvada, Young Canyon, and Ibapah), with varying ages, bulk chemistries and whole-rock $\delta^{18}O$. Feldspar separates were also analyzed in six of these samples (Contact, CI-65, RM-1, White Horse, Red Butte, and Ibapah). Most of the quartz, amphibole, and feldspar mineral separates were measured using CO_2-laser microprobe extraction systems. All quartz-feldspar, feldspar-hornblende, quartz-WR, and WR-hornblende $^{18}O/^{16}O$ fractionations in these samples were positive and less than 2‰, as expected for simple closed-system cooling. We conclude that subsolidus alteration probably did not substantially change the measured $\delta^{18}O$ of any of these samples, and that it is not a major factor affecting whole-rock $\delta^{18}O$ systematics in the rest of the samples.

5.3. Results

5.3.1. Cenozoic Suite

Cenozoic plutons consistently have the lowest $^{18}O/^{16}O$ of any age group, with whole-rock $\delta^{18}O$ between +7.0 to +9.7 (Figs. 2 and 3). A sample of Ibapah monzogranite, from the Deep Creek Range, was analyzed as quartz and feldspar mineral separates. An approximate whole-rock $\delta^{18}O$ of +9.7 is assigned to this sample based on a quartz $\delta^{18}O$ of +10.9 and a measured quartz-feldspar fractionation of slightly less than 2‰.

Within the Cenozoic group, plutons within and north of the East Humboldt Range (at about 40° 30' north latitude) display a range of $\delta^{18}O$ from +7.0 to +8.2, distinctly lower than those in the Ruby Range and farther south, which range from +8.6 to +9.7. The division closely corresponds to the Upper Array-Lower Array radiogenic-isotope boundary (CAB) of WRIGHT and WOODEN (1991). Also, the CAB approximately coincides (Fig. 5.1) with portions of the less well-defined EZ/CZ-S oxygen isotope boundary of SOLOMON and TAYLOR (1989), as well as with a bight in the Area Ib/Area II Pb-isotope boundary of ZARTMAN (1974).

5.3.2. Late Cretaceous Suite

High $^{18}O/^{16}O$ is observed in all samples from Late Cretaceous plutons; whole-rock $\delta^{18}O$ values range from +9.3 to + 12.1 (Figs. 5.2 and 5.3). All but one of these plutons are granites lying south of the CAB. The single sample collected north of this boundary, from the Toano Springs intrusion TR-82, displays a large quartz-feldspar $^{18}O/^{16}O$ fractionation of 5.3‰, clearly indicating some type of open-system, subsolidus exchange with a low-$\delta^{18}O$ fluid (meteoric-hydrothermal?). Therefore, we have adjusted the measured whole-rock $\delta^{18}O$ of +7.1 in this sample of the Toano Springs pluton upwards to its probable original magmatic value of +9.3, based on the measured $\delta^{18}O_{quartz}$ of +10.5. Inasmuch as the quartz $\delta^{18}O$ also may have been slightly lowered by hydrothermal exchange, the calculated value should be taken as only an approximate lower bound. Note that LEE et al. (1981b) measured a whole-rock $\delta^{18}O$ value of +9.1 for another sample from the Toano Springs pluton.

5.3.3. Jurassic Suite

The late Jurassic plutons analyzed in this study show a surprisingly wide range of $\delta^{18}O$ from +7.2 to +14.8 (Figs. 5.2 and 5.3), with many samples spread across the interval from $\delta^{18}O$ = +8.5 to + 12. Although all of the lowest $\delta^{18}O$ (< +9.0) samples were collected north of the CAB (Fig. 5.2), the $^{18}O/^{16}O$ variation in the Jurassic suite is not otherwise strongly correlated with geography. Virtually the entire range (+7.2 to +11.6) of $\delta^{18}O$ in the Jurassic suite is observed within a small area north of the CAB, in the four samples from two intrusions in the Crater Island Mountains, northwestern Utah. The very heterogenous oxygen-isotope compositions of the Jurassic granitoids sharply contrast with the restricted range of Sr- and Nd-isotope compositions in these samples.

5.4. Systematics of $\delta^{18}O$ Variation

5.4.1. Radiogenic Isotopes

On a $\delta^{18}O$ vs. $^{87}Sr/^{86}Sr_i$ plot (Fig. 5.4a), the granitoids separate into three distinct age groups and, for Cenozoic samples only, north and south geographic groups (relative to the CAB). Jurassic data form a band at low $^{87}Sr/^{86}Sr_i$, with $^{87}Sr/^{86}Sr_i$ increasing modestly with increasing $\delta^{18}O$ (from 0.705 - 0.707 at $\delta^{18}O$ = +7.2 to +9 to 0.709 - 0.711 at $\delta^{18}O$ = +12 to +13). By contrast, Late Cretaceous samples have higher and more variable $^{87}Sr/^{86}Sr_i$, up to 0.734, along a much steeper slope than the Jurassic suite. Cenozoic samples fall into two roughly equant groupings (Fig. 5.4a), with those south of the CAB overlapping the low-$\delta^{18}O$ end of the Late Cretaceous envelope, whereas the more northerly samples are distinct from all other groups in having low $\delta^{18}O$ (+7.0 to +8.2) combined with moderate $^{87}Sr/^{86}Sr_i$ (up to 0.715). Strontium (ppm) abundances

decrease with increasing $\delta^{18}O$ and $^{87}Sr/^{86}Sr_i$ in each age group, varying quite smoothly in the Jurassic suite (Fig. 5.4a).

Taken together, the northeastern Great Basin granitoids span most of the range of isotopic compositions observed throughout the entire Cordilleran belt of the western U.S.A.. The three age groups each resemble a different geographic-isotopic zone of SOLOMON and TAYLOR (1989). The Jurassic suite resembles their CZ-V field from western Nevada, the Late Cretaceous and southern Cenozoic data almost exactly overlap their CZ-S field (from eastern Nevada and western Utah), and the Cenozoic data as a whole straddle both sides of their EZ field at the same range of $^{87}Sr/^{86}Sr_i$, with the north Cenozoic samples generally having somewhat lower $\delta^{18}O$, and the south Cenozoic samples merging into the CZ-S field at higher $\delta^{18}O$.

On a $\delta^{18}O$ vs. εNd plot (Fig. 5.4b), each of the three age groups resembles the same geographic-isotopic zone of SOLOMON and TAYLOR (1989) that it does on the plot of $^{87}Sr/^{86}Sr_i$ vs. $\delta^{18}O$ (Fig. 5.4a). The Jurassic suite forms a flat, elongate array with high and relatively uniform εNd (-5.5 ± 3). Late Cretaceous and Cenozoic samples form bands at much lower εNd values. The Cenozoic samples again form two distinct envelopes, with samples south of the CAB partly overlapping the low-$\delta^{18}O$ end of the Late Cretaceous array, and the more northerly samples forming a separate grouping which extends to much lower εNd. Neodymium and samarium abundances decrease with increasing $\delta^{18}O$ for the Jurassic suite and, in a less pronounced fashion, for each of the subgroups of the Cenozoic suite; no trend is discernible in the Late Cretaceous samples.

In Figure 5.5, oxygen and lead isotope ratios are plotted, and the data separate into two distinct groups. The first group comprises the Jurassic, Late Cretaceous, and

southern Cenozoic samples, with the Jurassic samples plotting at the high-[208]Pb and high-[206]Pb part of the grouping. The second group is composed solely of the northern Cenozoic samples, which range to much less radiogenic (more depleted) Pb-isotopic compositions than the other group. Lead isotope compositions of all of the Jurassic samples as well as the more radiogenic Late Cretaceous and southern Cenozoic samples overlap with compositions observed in nearby sediments (VIKRE, 2000), suggesting that the lead in these granitoids is derived from the local upper crust. The remaining granitoids appear to contain a component of more deeply derived lead. The northern Cenozoic suite clearly has a component of lead derived from an ancient, low (U,Th)/Pb source (WRIGHT and WOODEN, 1991). The low $\delta^{18}O$ of these samples suggests that the depleted lead is derived directly from a crystalline basement source, rather than from a sedimentary section that has inherited an ancient Pb signature.

Cenozoic granitoids north and south of the CAB are compositionally distinct, with the northern samples having distinctly lower $\delta^{18}O$ and generally lower ϵNd, [208]Pb, [206]Pb, $^{87}Sr/^{86}Sr_i$, and Rb/Sr values, as well as slightly higher Sm/Nd. This systematic north/south variation is not apparent in the Jurassic granitoids. TR-82 is the only Late Cretaceous granite sampled north of the CAB, but it is consistent with the Cenozoic north/south pattern of variation in the sense that it also has low ϵNd and (tentatively) low $\delta^{18}O$ compared to the other Late Cretaceous samples.

5.4.2. Major and Trace elements

There is a positive correlation between $\delta^{18}O$, wt. % SiO2, and A/CNK for the wide range of Jurassic granitoid compositions, suggesting variable contributions from a high-$\delta^{18}O$ aluminous (~pelitic) sedimentary component. Correlations between major-

element compositions and $\delta^{18}O$ within the Late Cretaceous and middle-Tertiary

magmatic suites are not as clear-cut. There may be a rough positive correlation between

$\delta^{18}O$ and A/CNK in the Late Cretaceous suite. The few mafic mid-Tertiary samples (3

quartz diorites and a granodiorite) have relatively light oxygen ($\delta^{18}O$ = +7.0 to +7.6)

compared to more silicic monzogranites of the same age ($\delta^{18}O$ = +7.3 to +9.7).

A significant difference in the magmatic evolution of the Jurassic and Late

Cretaceous suites is apparent in a 1/Sr vs. $^{87}Sr/^{86}Sr_i$ plot (Figure 5.6). In terms of

strontium systematics, Fig. 5.6 shows that both suites have end members that are

relatively unradiogenic and Sr-rich (lower left of diagram), and in both suites there is a

discernible trend towards more evolved samples, extending toward lower strontium

abundances and higher $^{87}Sr/^{86}Sr_i$. The key difference is that the Jurassic suite forms a

steep array—with ppm Sr decreasing strongly but $^{87}Sr/^{86}Sr_i$ increasing only

moderately—while Late Cretaceous granites follow a much shallower trend. Taking a

high 86Sr/87Sr model component that is similar to Ruby Mountains miogeoclinal pelites

(KISTLER et al., 1981), as represented by nine mica- and quartzofeldspathic schist

samples (SPI-C, RM-19-67, SP-2, RM-27-66, RM-12-68, RM-7A-67, and RM-27F-67),

the orientation of the Jurassic array (mostly defined by four low-ppm Sr, moderate

$^{87}Sr/^{86}Sr_i$ samples: PR-79, RM-1, Notch Peak, and White Horse) is most consistent with

either assimilation/fractional-crystallization or heterogeneous assimilation, with Sr acting

as a compatible element. In contrast, $^{87}Sr/^{86}Sr_i$ increases markedly as ppm Sr decreases in

the Late Cretaceous samples, and actually overlaps the field of miogeoclinal pelites from

the Ruby Mountains (KISTLER et al., 1981). This trend is consistent with simple mixing

between a low $^{87}Sr^{86}Sr$ melt and a high $^{87}Sr^{86}Sr$ melt with a Sr abundance similar to bulk

sediment. The uniformly low εNd in the Late Cretaceous granites requires that both contributing end-members in Fig. 5.5 must be dominantly derived from ancient, low Sm/Nd crustal material. Thus, the low $^{87}Sr^{86}Sr$ component of the Late Cretaceous suite likely represents ancient, felsic crystalline basement rather than a mantle or mafic lower-crustal source.

5.5. The Origin of Northeastern Great Basin Granitoids

In $^{18}O/^{16}O$, as with the radiogenic isotopes measured by WRIGHT and WOODEN (1991), the granitoid plutons of the northeastern Great Basin can be grouped systematically by age. This indicates that much of the variation in magmatic isotopic composition was brought about by shifts in the nature, depth, and style of melting, and that these effects were superimposed upon the kinds of regional geographic variations of the source rocks described in earlier studies. From the systematics displayed in Figure 5.4, it might be argued that each of the geographic "zone" sources, delineated by FARMER and DEPAOLO (1983) and SOLOMON and TAYLOR (1989), is acting as the dominant source material during one of the three distinct magmatic episodes that occurred in this region between 170 Ma and 25 Ma. The simplest explanation is that the source rocks characteristic of each of these "zones" were in fact present at depth in northeastern Nevada and northwestern Utah, and that the observed progression of plutonic compositions resulted from selectively melting different source rocks at different times during the 150 million-year history of episodic plutonism in this area.

The major differences in εNd and $^{87}Sr^{86}Sr_i$ in the Late Cretaceous and Jurassic suites contrast sharply with their similar ^{18}O enrichments and highly radiogenic lead isotopic compositions (Figs. 5.4 and 5.5). This is a significant result, because the

oxygen-isotope data are indicating that many of the Jurassic plutons incorporated large amounts of sedimentary material even though the Sr- and Nd-isotope systematics and major-element compositions suggest that they are among the most primitive granitoids in the region.

5.5.1. Jurassic Suite

The relatively high whole-rock $\delta^{18}O$ values of many Jurassic plutons clearly point to a significant and ubiquitous crustal component. Using a simple model in which a fractionated, trace element-rich mantle melt ($\delta^{18}O \approx +6.5$) mixes with a typical fine-grained pelitic sediment ($\delta^{18}O \approx +16$ to $+19$; BURT, 1993; ESLINGER and SAVIN, 1973; PETERS and WICKHAM, 1995), the amount of such crustal material included in the Jurassic suite would range from 10% (CI-72) to 70% (Willard Creek), with many granitoids having 20% to 40% crustal material. Pelitic sedimentary rocks characteristically have $\delta^{18}O$ values that are as high or higher than any other likely crustal component, so these are lower-bound estimates. In detail, the Sr- and Nd- isotope systematics are not consistent with simple mixing, suggesting instead that assimilation/fractional crystallization processes were important. Nevertheless, the basic conclusion or the simple mixing model stands: a large component of crustal oxygen (and lead) is present in the Jurassic granitoids, and this must be reconciled with their relatively unevolved Sr- and Nd- isotope compositions.

We suggest that these plutons are mixtures of old (Proterozoic provenance), high-$\delta^{18}O$, high-$^{87}Sr/^{86}Sr_i$ continentally derived sediment which has been assimilated into low-$\delta^{18}O$, low-$^{87}Sr/^{86}Sr_i$ mantle melts (e.g, BARTON, 1990). An alternative hypothesis is that their isotopic signatures are primarily derived from the same sources inferred for the

CZ-V Cretaceous plutons in western Nevada (SOLOMON and TAYLOR, 1989), and that these Jurassic plutons were then physically separated from their underlying sources by major eastward thrusting (WRIGHT and WOODEN, 1991). We consider this alternative less likely, because the very radiogenic Pb characteristic of the Jurassic suite is not consistent with a relatively young volcanic-sedimentary source, and Cretaceous and younger plutons west of our study area do not contain the same extreme Pb-isotope compositions. Local, continentally derived sediments of the miogeocline, as well as some Late Cretaceous and (southern) Cenozoic plutons in our study area, do have the characteristic highly radiogenic Pb, suggesting that this is indeed a signature derived from the local upper crust (VIKRE, 2000; WOODEN et al., 1998).

The wide range of $^{18}O/^{16}O$ and broadly positive correlation between $^{87}Sr/^{86}Sr_i$ and $\delta^{18}O$, and the negative correlation of both of these isotopic signatures with Sr (ppm) are all compatible with an assimilation/fractional crystallization model. In this model, the mafic end member (hereafter called Component 1, or C1 for short) has moderate $\delta^{18}O$ (= +6.5), low $^{87}Sr^{86}Sr$ (= 0.705), and high ppm Sr ($\approx$ 1000), whereas the sedimentary component (Component 2, or C2 for short) has a higher $^{87}Sr^{86}Sr$, high $\delta^{18}O$ (at least +13 to +15), and typically less Sr ($\approx$ 200 ppm). Variable contamination with sediment led to a wide range of $\delta^{18}O$, but the high ppm Sr in the C1 component effectively buffered $^{87}Sr^{86}Sr$ in the liquid. Liquid compositions roughly matching the observed Jurassic trends in Figs. 5.4a and 5.6 are obtained with the following AFC model parameters: $\delta^{18}O_{C1}$ = +6.5, CC1(Sr) = 1000 ppm, $^{87}Sr^{86}Sr_{C1}$ = 0.705; $\delta^{18}O_{C2}$ = +17, C_{C2}(Sr) = 180 pprn, $^{87}Sr^{86}Sr_{C2}$ = 0.726; D_{Sr} = 1.5, r = 0.3. A C2 endmember with higher $\delta^{18}O$ ($\approx$ +19) is necessary to match the Miner's Spring Granite (PR-79) datum. Sr-isotopic characteristics

of the C2 end-member are based on Ruby Mountains quartzofeldspathic schist, mica-shist, and quartzite data from KISTLER et al. (1981); the nine samples from that study have mean Sr = 180 ppm and abundance-weighted mean $^{87}Sr^{86}Sr$ (150 Ma) = 0.726. The oxygen-isotope composition of C2 is chosen somewhat arbitrarily, but it roughly matches typical compositions of relatively unaltered pelitic sediments as measured by BURT (1993) $\delta^{18}O$ = +14 to +17, ESLINGER and SAVIN (1973), $\delta^{18}O$ = +15 to +19, one shale/phyllite sample from the Deep Creek Range (WICKHAM et al., 1991) $\delta^{18}O$ = +16.2, and three pelites from the lowest-grade part of the East Humboldt Range (PETERS and WICKHAM, 1995), $\delta^{18}O$ = +19. The high $\delta^{18}O$ of the C2 end-member suggested by PR-79 is also within this observed range. Although D_{Sr}, and r are not independently constrained by the oxygen-strontium systematics of the Jurassic data, reasonable results may be obtained so long as $1 > r \geq 0.25$ and $(D_{Sr} - r) \geq 1$. In these feldspar-rich lithologies it is certainly reasonable to expect that $D_{Sr} > 1$ (i.e., strontium is compatible), and small r values are consistent with assimilation of relatively cold sedimentary rocks.

The assimilation/fractional-crystallization model is also consistent with observed oxygen-neodymium systematics, with the C1 end member having high εNd ($\approx$ -3) and high ppm Nd ($\approx$ 100). As with Sr, high relative Nd abundance in C1 buffers the Nd-isotopic composition of the melt during crustal contamination, and εNd barely decreases over a range of $\delta^{18}O$. The Nd-isotope composition of C2 is chosen to match the abundance-weighted mean composition (45 ppm Nd, εNd = −13.9 at 150 Ma) of ten shale, phyllite, and schist samples from the Northeastern Great Basin (FARMER and BALL, 1997). These samples have inferred provenance ages ranging from mid-Proterozoic to

Archean (FARMER and BALL, 1997). AFC models with these parameters, r = 0.3, and

DNd ≈ 1- 1.5 are in fair agreement with the observed trend in Fig. 5.4b. A better match is

obtained if the C2 component has a higher εNd (-10.2 at 150 Ma), corresponding to the

weighted-mean composition of the four stratigraphically lowest samples in the FARMER

and BALL (1997) study. These samples are inferred to have Proterozoic provenance ages.

The proposed C1 component is not simply a basalt derived from depleted mantle,

which would be expected to have $^{87}Sr^{86}Sr$ C1 < 0.704 and εNd > 0. C1 may instead

represent a melt of depleted mantle which has already undergone fractionation and been

contaminated by crustal material. Alternatively, it may be derived from an ancient

continental lithosphere source similar to the enriched source inferred for some Tertiary

and Quaternary basalts in the Great Basin (REID and GRAHAM, 1996).

The FARMER and DEPAOLO (1983, 1984) model for the formation of

transition-zone (TZ) granitoids is qualitatively similar to our model for the Jurassic suite.

A significant difference is their preference for a relatively Nd- and Sr-poor mafic end

member derived directly from a depleted mantle source. In the Farmer and DePaolo

model, variations in ppm Sr within the EG plutons result from substantial variations in

D_{Sr} (from < 0. 1 to > 1) during AFC processing in the crust. We argue that the variation

in Sr abundance within the Jurassic suite is probably not the result of variations in the

effective D_{Sr}, during an AFC process, because ppm Sr correlates with the abundances of

other trace elements (LREE, Ba, Zr), as well as with wt.% CaO, P_2O_5, and TiO_2 (MILLER

and HOISCH, 1995). It is unlikely that such a diverse group of elements were all

incompatible in some granitoids and all compatible in others, always behaving as a

group. It is more likely that they are all behaving "compatibly," in the sense of being

diluted by the same processes of crustal assimilation and fractionation, and that the granitoids richest in these components are the most primitive.

The assimilation process outlined above is consistent with the metamorphic and tectonic history of this region, suggesting the intrusion of deeply derived magmas into a relatively cool and previously unaltered sedimentary section. Mafic dikes are associated with Jurassic intrusions in the Crater Islands (MILLER and HOISCH, 1995), demonstrating the presence of mantle-derived melts at this time.

5.5.2. Late Cretaceous Suite

$^{18}O/^{16}O$ and other isotopic ratios in the Late Cretaceous plutonic suite are in excellent agreement with the measurements of SOLOMON and TAYLOR (1989) in the same region, which placed the Ruby and Southern Snake Ranges, from which most of our samples were taken, within their high-$\delta^{18}O$ CZ-S zone. The high $\delta^{18}O$ values of these plutons clearly point to a major sedimentary component, and in combination with the high $^{87}Sr/^{86}Sr_i$ and low ϵNd of these samples, it is evident that a major source of melt in the Late Cretaceous was sediment derived from ancient continental crust (FARMER and DEPAOLO, 1983; SOLOMON and TAYLOR, 1989). At least 30% to 60% sedimentary oxygen is implied for this suite if it is a mixture of mantle-derived melt ($\delta^{18}O \approx +6$) and crustal sediments ($\delta^{18}O \approx +16$ to $+19$). The uniformly low ϵNd, high wt.% SiO_2 and A/CNK of the Late Cretaceous granites, however, suggest that the low-$\delta^{18}O$, low-$^{87}Sr^{86}Sr$ end-member is also ancient crust—the isotopic systematics of nearby mid-Cenozoic intrusions suggest that it represents a basement component. The observed overlap of the Late Cretaceous array with the envelope of miogeoclinal pelites (KISTLER et al., 1981) in Fig. 5.6 is consistent with simple mixing between these crustal sources.

Another possible explanation for the difference in the $\delta^{18}O$ systematics of Jurassic and Late Cretaceous plutons is that the high $\delta^{18}O$ component of the Late Cretaceous granites had a lower $\delta^{18}O$ than the equivalent component in Jurassic plutons due to post-Jurassic regional hydrothermal resetting of the sedimentary/metamorphic pile. Oxygen isotope studies in the Ruby Mountains and near the Idaho Batholith show that the highest-grade metasedimentary rocks in both areas underwent substantial lowering of $\delta^{18}O$ during metamorphism, probably as a result of fluid infiltration events sometime between the latest Jurassic and the Cenozoic (CRISS and FLECK, 1990; FLECK and CRISS, 1986; KISTLER et al., 1981; WICKHAM et al., 1991). The metasedimentary rocks that make up the Late Cretaceous "C2" component (and possible metasedimentary components in the Cenozoic plutons) may have thus had lower $\delta^{18}O$ than the Jurassic C2 component (Fig. 5.7). Measured $\delta^{18}O$ in the high-grade metapelites and metaquartzites from the Ruby Mountains and vicinity ($\delta^{18}O \approx +8$ to $+13$) (KISTLER et al., 1981; WICKHAM et al., 1991), and the likelihood that the low-$\delta^{18}O$ end-member is felsic crystalline basement ($\delta^{18}O \approx +7$ to $+9$), are both consistent with a larger metasedimentary contribution to the late Cretaceous granites, of or 60%–100% (Fig. 5.7).

We argue that this simple mixing trend is an expected result of the anatectic melting that followed Sevier-related compression. Sevier thrusting may have begun as early as the Late Jurassic (REF), and thrusting along the Sevier front was certainly underway by Aptian time (~115 Ma) (HELLER et al., 1986; HELLER and PAOLA, 1989), at least 30 million years prior to the Late Cretaceous magmatic event. PATINO-DOUCE et al. (1990) have shown theoretically that compression of the miogeocline and underlying basement was likely to lead to anatectic melting of the crustal section in this region on

roughly a 30 million year timescale. In the Patiño-Douce model melting is most likely to occur in the bottom part of the sedimentary pile and in the uppermost (felsic) part of the underlying basement—and as we have argued, these are the source rocks that are most consistent with the isotopic and bulk compositions of the Late Cretaceous granites.

5.5.3. Cenozoic Suite

The intermediate, restricted range of $\delta^{18}O$ of the Cenozoic granitoids, coupled with their low εNd, moderate $^{87}Sr/^{86}Sr_i$, and heterogeneous and depleted lead isotope compositions, is consistent with an ancient, depleted, high-grade or crystalline continental basement source, particularly for the northern group of Cenozoic samples. The inferred basement source, must extend westward well into northeastern Nevada, at least to the Roberts Mountains Thrust, in agreement with the conclusions of WRIGHT and WOODEN (1991), WRIGHT and SNOKE (1993), and FARMER and DePAOLO (1983). There is no transition toward higher $\delta^{18}O$ or higher εNd in the westernmost Cenozoic granitoids, as might be expected in the crystalline basement thinned greatly and either oceanic basement or relatively undepleted sediments of the miogeocline made a larger relative contribution.

Because of the great similarities between the southern Cenozoic and the Late Cretaceous samples in most isotopic parameters, the higher values of $\delta^{18}O$ and $^{87}Sr/^{86}Sr_i$ of the Cenozoic samples south of the CAB might be interpreted to indicate that the depleted basement there *is* thinned or actually absent, at any rate it appears to be a less prominent component than in the northern samples. This model is qualitatively compatible with the suggestion of SOLOMON and TAYLOR (1989) that the craton may have been rifted apart in this area along a westward continuation of the thick Proterozoic sedimentary wedge that crops out in the Uinta Basin in Utah. In studying related

Cenozoic volcanic rocks in the vicinity of the Egan Range, GRUNDER and WICKHAM

(1991) found evidence for a relatively low $\delta^{18}O$ metasedimentary source, with continued

lowering of $\delta^{18}O$ over the duration of volcanism. Such a process might help to explain the

moderate $\delta^{18}O$ observed in the relatively silicic, high $^{87}Sr/^{86}Sr_i$ southern Cenozoic

plutons. However, observed isopachs of thickness of the lower, siliclastic portion of the

miogeocline (STEWART and POOLE, 1974) cut the CAB at a high angle and actually

indicate a thicker sedimentary section (and a thinner basement?) north of the CAB than

south. Furthermore, southern Cenozoic plutons are generally less aluminous than the Late

Cretaceous granites, suggesting a significant basement component.

More than any other age group, the Cenozoic suite is consistent with a model in

which the crust was heated from below, either by the thinning of the subcontinental

lithosphere or by intrusion and/or pooling of mantle-derived melts near the base of the

crust. (BARTON, 1990) has suggested a very similar mechanism, and analogous models

have been proposed by FARMER and DEPAOLO (1983) and by ELISON et al. (1990) for

earlier episodes of magmatism in the Great Basin. From its Sr- and Pb-isotope

composition and inferred age of formation, the characteristic source rock for the northern

Cenozoic granitoids appears to have been significantly depleted, and we would not

expect it to melt easily. This is a marked contrast to both older magmatic suites, which

show evidence of having preferentially incorporated less-depleted (and presumably less

refractory) crustal components. Close juxtaposition of a large mafic melt body, or

asthenospheric mantle, is a relatively simple way to explain melting of a depleted lower-

crustal source.

5.6. Conclusions

Measurement and compilation of the oxygen-isotope compositions of Jurassic, Late Cretaceous, and Cenozoic granitoids in the northeastern Great Basin verifies and modifies existing hypotheses of their formation, demonstrating conclusively that different source rocks were involved in the generation of each of these plutonic suites. The wide range of $^{18}O/^{16}O$ in Jurassic granitoids strongly suggests moderate to extensive (typically 20% - 40%) assimilation of continentally derived, miogeoclinal sedimentary rocks into a Sr- and Nd-rich melt generated in the mafic lower crust or upper mantle.

The low $^{18}O/^{16}O$ of Cenozoic granitoids requires an origin largely within high-grade basement with at most a modest assimilation of sediments, particularly for those Cenozoic plutons north of the CAB. The tight groupings and robust geographic distinctions within the Cenozoic suite (low $^{18}O/^{16}O$ in the north and higher $^{18}O/^{16}O$ to the south) suggest a magmatic source in ancient felsic or mafic continental basement, marked by an important ESE-trending boundary at depth that is coincident with the CAB. The CAB thus appears to be a tangible province boundary for the Cenozoic suite. An alternative mechanism based on southward-increasing assimilation of high $^{18}O/^{16}O$ sedimentary material of the miogeocline cannot be excluded, but appears less likely. Mixing models indicate that it is possible to generate both the Jurassic and Cretaceous magmatic suites from basically the same kind of high-^{87}Sr, low εNd, upper crustal end member, but this is most readily done if we assume that the bulk $\delta^{18}O$ values in this end member were lowered by roughly 2–3 ‰ following the Jurassic magmatic event. Thus, we can explain the Late Cretaceous isotopic systematics by utilizing the model of FLECK and CRISS (1986) for similar upper crustal metasedimentary rocks in the northern Idaho

batholith, and also by utilizing the observations of WICKHAM et al. (1991) that metasedimentary rocks in the Ruby Mountains metamorphic core complex have in fact undergone just this kind of bulk $\delta^{18}O$ lowering, as a result of metamorphic hydrothermal fluid-rock interactions. With this scenario, the Late Cretaceous granites could be almost entirely continental-crustal in character. Basement similar to the Cenozoic source conceivably could be a dominant low $^{18}O/^{16}O$ end member for the Cretaceous suite, but not much of this component is required if the proposed hydrothermal $\delta^{18}O$ lowering actually took place.

5.7. Bibliography

Barton M. D. (1990) Cretaceous magmatism, metamorphism, and metallogeny in the east-central Great Basin. In *The nature and origin of Cordilleran magmatism, GSA Memoir*, Vol. 174 (ed. J. L. Anderson), pp. 283-302. GSA.

Barton M. D., Battles D. A., Bebout G. E., Capo R. C., Christensen J. N., Davis S. R., Hanson R. B., Michelsen C. J., and Trim H. E. (1988) Mesozoic contact metamorphism in the western United States. In *Metamorphism and crustal evolution of the western United States* (ed. W. G. Ernst), pp. 110-178. Prentice-Hall.

Bennett V. C. and DePaolo D. J. (1987) Proterozoic crustal history of the western United States as determined by neodymium crustal mapping. *GSA Bulletin* **99**, 674-685.

Best M. G., Armstrong R. L., Graustein W. C., Embree G. F., and Ahlborn R. C. (1974) Mica granites of the Kern Mountains Pluton, eastern White Pine

Country, Nevada: remobilized basement of the cordilleran miogeosyncline? *GSA Bulletin* **85**, 1277-1286.

Burt E. A. (1993) Oxygen isotope studies of some sedimentary and metasedimentary rocks of the central and northern Appalachain mountains, the Colorado plateau, and the Ouachita mountains. Ph. D., Caltech.

Compton R. R., Todd V. S., Zartman R. E., and Naeser C. W. (1977) Oligocene and Miocene metamorphism, folding, and low-angle faulting in nortwestern Utah. *GSA Bulletin* **88**, 1237-1250.

Criss R. E. and Fleck R. J. (1990) Oxygen isotope map of the giant metamorphic-hydrothermal system around the northern part of the Idaho batholith, USA. *Applied Geochemistry* **5**, 641-655.

Elison M. W. (1995) Causes and consequences of Jurassic magmatism in the northern Great Basin: implications for tectonic development. In *Jurassic magmatism and tectonics of the North American cordillera, GSA Special Paper*, Vol. 299 (ed. D. M. Miller and C. Busby), pp. 249-265. GSA.

Elison M. W., Speed R. C., and Kistler R. W. (1990) Geologic and isotopic constraints on the crustal structure of the northern Great Basin. *GSA Bulletin* **102**, 1077-1092.

Eslinger E. V. and Savin S. M. (1973) Oxygen isotope geothermometry of the burial metamorphic rocks of the Precambrian Belt Supergroup, Glacier National Park, Montana. *GSA Bulletin* **84**(8), 2549-2560.

Farmer G. L. and Ball T. T. (1997) Sources of middle Proterozoic to early Cambrian siliciclastic sedimentary rocks in the Great Basin: a Nd isotope study. *GSA Bulletin* **109**, 1193-1205.

Farmer G. L. and DePaolo D. J. (1983) Origin of Mesozoic and Tertiary granite in the western United States and implications for pre-Mesozoic crustal structure: 1. Nd and Sr isotopic studies in the geocline of the northern Great Basin. *J. Geophys. Res.* **88**, 3379-3401.

Farmer G. L. and DePaolo D. J. (1984) Origin of Mesozoic and Tertiary granite in the western United States and implications for pre-Mesozoic crustal structure: 2. Nd and Sr isotopic studies of unmineralized and Cu- and Mo-mineralized granite in the Precambrian craton. *J. Geophys. Res.* **89**, 10141-10160.

Fleck R. J. and Criss R. E. (1986) Strontium and oxygen isotopic variations in Mesozoic and Tertiary plutons of central Idaho. *Contributions to Mineralogy and Petrology* **90**, 291-308.

Grunder A. L. (1992) 2-stage contamination during crustal assimilation - isotopic evidence from volcanic-rocks in eastern Nevada. *Contributions to Mineralogy and Petrology* **112**, 219-229.

Grunder A. L. and Wickham S. M. (1991) Homogenization and lowering of O-18/O-16 in midcrustal rocks during extension-related magmatism in eastern Nevada. *EPSL* **107**, 416-431.

Heller P. L., Bowdler S. S., Chambers H. P., Coogan J. C., Hagen E. S., Shuster M. W., Winslow N. S., and Lawton T. F. (1986) Time of initial thrusting

in the Sevier orogenic belt, Idaho, Wyoming and Utah. *Geology* **14**(5),
388-391.

Heller P. L. and Paola C. (1989) The paradox of lower Cretaceous gravels and
the initiation of thrusting in the Sevier orogenic belt, United States
western interior. *GSA Bulletin* **101**, 864-875.

Hudec M. R. (1992) Mesozoic structural and metamorphic history of the central
Ruby Mountains metamorphic core complex, Nevada. *GSA Bulletin* **104**,
1086-1100.

Kistler R. W., Ghent E. D., and O'Neil J. R. (1981) Petrogenesis of garnet two-
mica granites in the Ruby Mountains, Nevada. *J. Geophys. Res.* **86**,
10591-10606.

Kistler R. W. and Peterman Z. E. (1973) Variations in Sr, Rb, K, Na, and initial
$^{87}Sr/^{86}Sr$ in Mesozoic granitic rocks and intruded wall rocks in central
California. *GSA Bulletin* **84**, 3489-3512.

Lee D. E. (1984) Analytical data for a suite of granitoid rocks from the Basin
and Range province. *U. S. Geol. Survey Bull.* **1602**.

Lee D. E. and Christiansen E. H. (1983) The granite problem as exposed in the
Southern Snake Range, Nevada. *Contributions to Mineralogy and
Petrology* **83**, 99-116.

Lee D. E., Friedman I., and Gleason J. D. (1981a) Map showing oxygen isotope
composition of granitoid rocks of the Basin-Range province. *U. S. Geol.
Survey Miscellaneous Field Studies Map* **MF-1305**.

Lee D. E., Friedman I., and Gleason J. D. (1982) The oxygen isotope composition of granitoid and sedimentary rocks of the Southern Snake Range, Nevada. *Contributions to Mineralogy and Petrology* **79**, 150-158.

Lee D. E., Kistler R. W., Friedman I., and Van Loenen R. E. (1981b) Two-mica granites of northeastern Nevada. *J. Geophys. Res.* **86**, 10607-10616.

Lee D. E., Stacey J. S., and Fischer L. (1983) Radiometric ages of two-mica granites of northeastern Nevada. *U. S. Geol. Survey Professional Paper* **P 1375**.

Miller D. M., Hillhouse W. C., Zartman R. E., and Lanphere M. A. (1987) Geochronology of intrusive and metamorphic rocks in the Pilot Range, Utah and Nevada, and comparison with regional patterns. *GSA Bulletin* **99**, 866-879.

Miller D. M. and Hoisch T. D. (1995) Jurassic tectonics of northeastern Nevada and northwestern Utah from the perspective of barometric studies. In *Jurassic magmatism and tectonics of the North American cordillera, GSA Special Paper*, Vol. 299 (ed. D. M. Miller and C. Busby), pp. 267-294. GSA.

Miller D. M., Nakata J. K., and Glick L. L. (1990) K-Ar ages of Jurassic to Tertiary plutonic and metamorphic rocks, northwestern Utah and northeastern Nevada. *U. S. Geol. Survey Bull.* **1907**, 1-17.

Miller E. L., Gans P. B., Wright J. E., and Sutter J. F. (1988) Metamorphic history of the east-central Basin and Range province: tectonic setting and

relationship to magmatism. In *Metamorphism and crustal evolution of the western United States* (ed. W. G. Ernst), pp. 649-682. Prentice-Hall.

Muffler L. J. P. (1964) Geology of the Frenchie Creek quadrangle, north-central Nevada. *U. S. Geol. Survey Bull.* **1179**.

Patino-Douce A. E., Humphreys E. D., and Johnston A. D. (1990) Anatexis and metamorphism in tectonically thickened continental crust exemplified by the Sevier hinterland, western North America. *EPSL* **97**(3-4), 290-315.

Peters M. T. and Wickham S. M. (1995) On the causes of O-18 depletion and O-18/O-16 homogenization during regional metamorphism - the East Humboldt Range core complex, Nevada. *Contributions to Mineralogy and Petrology* **119**, 68-82.

Reid M. R. and Graham D. W. (1996) Resolving lithospheric and sub-lithospheric contributions to helium isotope variations in basalts from the southwestern U.S. *EPSL* **144**(1-2), 213-222.

Solomon G. C. (1989) An $^{18}O/^{16}O$ study of Mesozoic and early Tertiary granitic batholiths of the soutwestern North American cordillera. Ph. D., Caltech.

Solomon G. C. and Taylor H. P., Jr. (1989) Isotopic evidence for the origin of Mesozoic and Cenozoic granitic plutons in the northern Great Basin. *Geology* **17**, 591-594.

Stewart J. H. and Poole F. G. (1974) Lower Paleozoic and uppermost Precambrian cordilleran miogeocline, Great Basin, United States. In *Tectonics and sedimentation, Soc. Econom. Paleont. Mineral. Spec. Pub.*, Vol. 22 (ed. W. R. Dickinson), pp. 28-57.

Vikre P. (2000) Subjacent crustal sources of sulfur and lead in eastern Great Basin metal deposits. *GSA Bulletin* **112**(5), 764-782.

Wickham S. M., Taylor H. P., Jr., Snoke A. W., and O'Neil J. R. (1991) An oxygen and hydrogen isotope study of high-grade metamorphism and anatexis in the Ruby-Mountains-East-Humboldt Range core complex, Nevada. In *Stable isotope geochemistry: a tribute to Samuel Epstein, Geochem. Soc. Special Pub.*, Vol. 3 (ed. H. P. Taylor, Jr., J. R. O'Neil, and I. Kaplan), pp. 373-390. Geochem. Soc.

Wooden J. L., Kistler R. W., and Tosdal R. M. (1998) Pb isotopic mapping of crustal structure in the northern Great Basin and relationships to Au deposit trends. *U. S. Geol. Survey Open-File Rep.* **98-338**, 20-33.

Wright J. E. and Snoke A. W. (1993) Tertiary magmatism and mylonitization in the Ruby-East Humboldt metamorphic core complex, northeastern Nevada: U-Pb geochronology and Sr, Nd, and Pb isotope geochemistry. *GSA Bulletin* **105**, 935-952.

Wright J. E. and Wooden J. L. (1991) New Sr, Nd, and Pb isotopic data from plutons in the northern Great Basin: implications for crustal structure and granite petrogenesis in the hinterland of the Sevier thrust belt. *Geology* **19**, 457-460.

Zamudio J. A. and Atkinson W. W., Jr. (1995) Mesozoic structures of the Dolly Varden Mountains and Currie Hills, Elko County, Nevada. In *Jurassic magmatism and tectonics of the North American cordillera, GSA Special Paper*, Vol. 299 (ed. D. M. Miller and C. Busby), pp. 295-311. GSA.

Zartman R. E. (1974) Lead isotopic provinces in the cordillera of the western United States and their geologic significance. *Economic Geology* **69**(792-805).

Table 5.1. Whole-rock oxygen, strontium, and neodymium isotopic compositions, and feldspar lead isotopic compositions of granitoids from the NE Great Basin. Most $^{18}O/^{16}O$ data were measured in the present study on the same samples used for radiogenic isotope measurements; however, underlined $^{18}O/^{16}O$ data are from LEE and CHRISTIANSEN (1983), LEE et al. (1983), LEE et al. (1982), or SOLOMON (1989), and although from the same pluton, are in general from different samples than those used for radiogenic isotope measurements. Strontium, neodymium, and lead isotope data are a subset of the analyses reported by WRIGHT and WOODEN (1991), FARMER and DEPAOLO (1983), KISTLER et al. (1981), LEE and CHRISTIANSEN (1983), and LEE et al. (1982).

Sample	Location	[a]Contact Rock	$\delta^{18}O$	Age Ma	$\frac{^{87}Sr}{^{86}Sr_i}$	ϵ_{Nd}	$\frac{^{206}Pb}{^{204}Pb}$	$\frac{^{207}Pb}{^{204}Pb}$	$\frac{^{208}Pb}{^{204}Pb}$	[b]Rec. Ref.	[c]Lee GR #
Jurassic North											
(HD-55) Contact, granodiorite	Granite Range	Penn - Per	+8.5, +8.6	160	0.70535	-3.1	19.779	15.746	39.709	MH	57, 58
(NF-192) Newfoundland, monzogranite	Newfoundland Mts.	Cam - Ord	+9.1	160	0.70514	-4.6	19.602	15.804	40.116	MNG	
(CI-72) Crater Island, monzodiorite	Silver Island Mts.	Penn - Per	+7.2	160	0.70567	-4.5				MNG	
(CI-71) Crater Island, qtz. monzonite	Silver Island Mts.	Penn - Per	+8.5	160	0.70618	-4.9				MNG	
(CI-65) Crater Island, granodiorite	Silver Island Mts.	Ordovician	+9.7	160	0.70563	-4.9	19.603	15.773	40.119	MNG	
(CI-14) Crater Island, monzogranite	Silver Island Mts.	Ordovician	+11.6	160	0.70600	-6.0	19.636	15.793	40.165	MNG	
(PR-79) Miners Spring, 2-mica granite	Pilot Range	PC - Camb	[d]+14.8	160	0.71043	-6.4	19.712	15.814	39.865	MHZL	
Silver Zone Pass Pluton, granodiorite	Silver Zone Pass	Cambrian	[e]+8.8	162	0.7054	-2.5	19.960	15.763	39.962	ST-FD	
Jurassic South											
(RM-1) Dawley Canyon, 2-mica granite	Ruby Mtns.	PC? - Camb	+11.8	153	0.71108	-5.7	19.792	15.773	39.373	MH	
(WH-21) White Horse, granodiorite	Goshute Range	Devonian	+9.6, +10.4	160	0.70718	-5.5	19.584	15.760	39.720	MH	123, 124
Notch Peak, monzonite	House Range	Cambrian	+9.3, +9.3	170	0.70694	-6.3	19.061	15.772	39.640	LSF	3, 4
(M5P-8) Melrose Pluton, monzonite	Dolly Varden Mts.	Permian	+8.8, +9.1	170	0.70663	-5.3	19.802	15.804	40.404	ZA	125, 126
Cottonwood Canyon, pyx gabbro[f]	Cortez Mts.	[f]Penn - Per	+9.0	160	0.70603	-2.9	19.832	15.711	39.330	M	
Osceola, granodiorite	So. Snake Range	PC - Camb	+9.8	160	0.7075					LC	
Snake Creek-Williams Canyon, zoned tonalite-granodiorite-granite	So. Snake Range	PC - Camb	+10.2 to +12.2	155	0.7071					LC	
Willard Creek, two-mica granite	So. Snake Range	PC - Camb	+13.2	160	0.7086					LC	
(UT GH-2) South stock, monzogranite	Gold Hills	Miss - Penn	+9.0	152	0.7097	-8.6	19.601	15.815	40.184	ST-FD	
Late Cretaceous North											
(TR-82) Toano Springs, 2-mica granite	Toana Range	Cambrian	[e]+9.3, [d]+9.1	75	0.72508	-23.2	19.556	15.903	40.900	MNG	25, 26

Late Cretaceous South

Sample	Location	Country rock	δ18O	Age	87Sr/86Sr	εNd	206Pb/204Pb	207Pb/204Pb	208Pb/204Pb	Pluton	Ref.
(RM-4) two-mica leucogranite	Ruby Mts.	PC? - Camb	+12.1	80	0.72609	-15.1	19.586	15.793	39.758	WS	
Lexington Creek, two-mica granite	So. Snake Range	Ordovician	+9.9, +10.6	86	0.71094	-12.9	18.802	15.652	39.188	LC	47, 48
Pole Canyon, two-mica granite	So. Snake Range	Cambrian	+10.9, +10.9	80	0.71656	-16.7	18.600	15.647	39.377	LC	
Deadman, two-mica granite	No. Snake Range	Cambrian	+10.4	83	0.71152	-17.4	18.602	15.654	38.782		
Smith Creek, muscovite granite	No. Snake Range	Cambrian	+10.8	83	0.73355	-17.0	19.581	15.788	39.369		
(NV 77-10) Tungstonia, 2-mica granite	Kern Mtns.	Miss	+9.6	58	0.7212	-19.1				ST-FD	

Cenozoic North

Sample	Location		δ18O	Age	87Sr/86Sr	εNd	206Pb/204Pb	207Pb/204Pb	208Pb/204Pb	Pluton	Ref.
(4134-15) Angel Lake, monzogranite	E. Humboldt Rng.		+7.3	29	0.71382	-24.4	18.228	15.762	39.038	WS	
(RM-13) qtz. diorite	E. Humboldt Rng.		+7.0	38	0.71042	-16.5	18.208[g]	15.755[g]	39.731[g]	WS	
(RM-19) qtz. diorite gneiss	E. Humboldt Rng.		+7.6	38	0.71240	-22.2	17.816[g]	15.627[g]	39.012[g]	WS	
(PR-82) Bettridge Canyon, granodiorite	Pilot Range		+7.2	39	0.71104	-17.3	18.451	15.764	38.343	MHZL	
McGinty, monzogranite	Pilot Range		+7.9, +7.9	36	0.70717	-13.3	17.736	15.563	37.949	MHZL	23, 24
Red Butte, two-mica monzogranite	Grouse Creek Mts.		+8.0	25	0.71559	-26.3	17.507	15.649	38.379	CTZN	
(TEP-1) Immigrant Pass, monzogranite	Grouse Creek Mts.		+7.4	38	0.71022	-22.1	17.749[g]	15.643[g]	38.057[g]	CTZN	21, 22?
(TEP-3) Immigrant Pass, monzogranite	Grouse Creek Mts.		+8.2	38	0.70973	-18.4	17.023	15.540	37.822[g]	CTZN	21, 22?
(TEP-2) Immigrant Pass, qtz. diorite	Grouse Creek Mts.		+7.7	38	0.70908	-16.6	16.893[g]	15.474[g]	37.562[g]	CTZN	21, 22?

Cenozoic South

Sample	Location		δ18O	Age	87Sr/86Sr	εNd	206Pb/204Pb	207Pb/204Pb	208Pb/204Pb	Pluton	Ref.
Uvada, monzogranite	Kern Mts.		+9.2	35	0.71447	-18.2	19.463[g]	15.759[g]	39.729[g]	B	
(KM-23) Skinner Canyon, monzogranite	Kern Mts.		+8.6	35	0.71141	-16.9	18.561	15.651	39.563	B	
(HM-1b) Heusser Mtn., monzogranite	Egan Range		+9.4	35	0.71339	-15.9	19.064	15.714	39.672	MGWS	
(PBG-107) Cleveland Rnch.,monzogranite	Schell Ck. Range		+9.4	35	0.71332	-16.4	19.064	15.715	39.679	MGWS	
Young Canyon, monzogranite	So. Snake Range		+9.5, +8.7 to +10.0	36	0.71287	-15.3	18.228	15.664	39.286	LC	
Ibapah, monzogranite	Deep Ck. Range		[e]+9.7, +9.6	39	0.71659	-16.8	19.108	15.778	39.986	MGWS	91, 92
(HP-2) Harrison Pass, monzogranite	Ruby Mtns.		+9.5	36	0.7110	-13.2				ST-FD	
(NV CC-1) Cherry Ck., monzogranite	Egan Range		[d]+5.8	32	0.7137	-16.9				ST-FD	
(UT GH-1) N. Stock, monzogranite	Gold Hills		+8.4	38	0.7157	-18.7				ST-FD	

a - Youngest stratigraphic age of the country rocks along the contact of each Jurassic and Late Cretaceous pluton.

b - References for the isotope data, dating, and/or geology for each sample or pluton: B - (BEST et al., 1974), CTZN - (COMPTON et al., 1977), LC - (LEE and CHRISTIANSEN, 1983), LSF - (LEE et al., 1983), M - (MUFFLER, 1964), MGWS -

(MILLER et al., 1988), MHZL - (MILLER et al., 1987), MH - (MILLER and HOISCH, 1995), MNG - (MILLER et al., 1990), ST-FD - (SOLOMON and TAYLOR, 1989) and (FARMER and DEPAOLO, 1983), WS - (WRIGHT and SNOKE, 1993), ZA - (ZAMUDIO and ATKINSON, 1995).

^{c} - Index number for Great Basin granitoid samples from the same pluton collected and tabulated by LEE (1984), and analyzed by LEE et al. (1981a).

^{d} - Whole-rock $\delta^{18}O$ measurement which is considered likely to have been altered from its magmatic value.

^{e} - Whole-rock $\delta^{18}O$ calculated by subtracting 1.2 per mil from the $\delta^{18}O$ of a quartz separate.

^{f} - The Cottonwood Canyon intrusion is almost entirely a pyroxene-granodiorite with around 62 wt.% SiO_2 and a color index of 25 or less (MUFFLER, 1964), which is intruded into allocthonous eugeoclinal rocks rather than the miogeocline.

^{g} – Whole-rock Pb data.

Figure 5.1. Schematic map of the Great Basin and surrounding regions showing relevant geologic and geochemical zones and boundaries. The thick, gray CAB corresponds to the boundary between the Upper and Lower Arrays of WRIGHT and WOODEN (1991). Samples in this study are from the light-gray shaded rectangle at the center of the map (this area is shown in more detail in Fig. 5.2). For clarity, the zonal boundaries of FARMER and DEPAOLO (1983) are not shown separately; however, their EG covers almost all of Nevada west of the 0.706 line, their transition zone (TZ) lies between the 0.706 line and the RMT, their MG zone extends from the RMT to somewhat east of the Utah-Nevada border, and the CG is farther east, covering most of Utah.

Fig. 5.1.
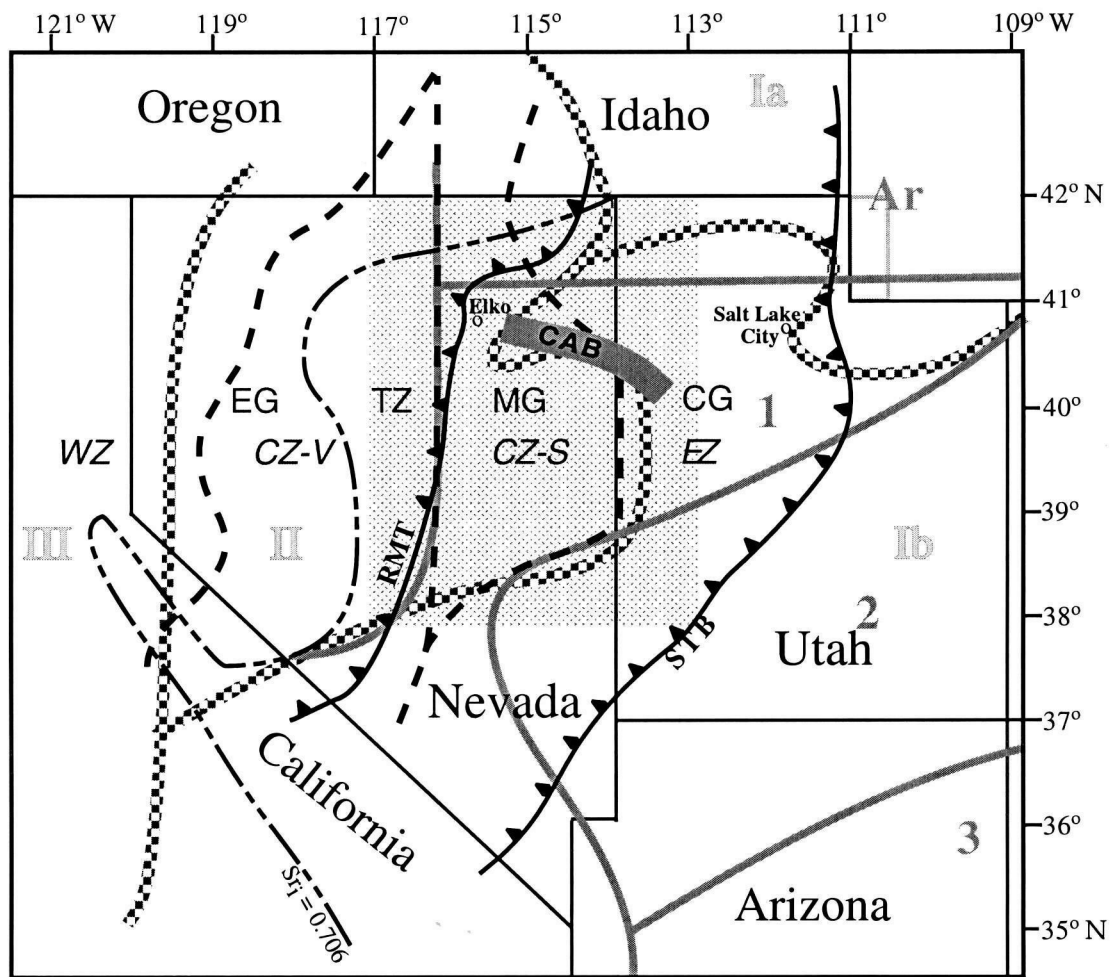
GLOSSARY OF ZONES AND ABBREVIATIONS:

RMT	- Roberts Mountains Thrust (approx.)		
STB	- Sevier Thrust Belt (approx.)		

Kistler and Peterman (1973) $^{87}Sr/^{86}Sr_i = 0.706$ line

Zartman (1974)

Bennett and DePaolo (1987)
Ar	T_{DM} > 2.7 Ga age province
1	T_{DM} = 2.0 - 2.3 Ga age province
2	T_{DM} = 1.8 - 2.0 Ga age province
3	T_{DM} = 1.7 - 1.8 Ga age province

Wright and Wooden (1991)
CAB	Crustal Age Boundary, Archaean source north Proterozoic south

Ia	Archaean (depleted) lead province
Ib	Proterozoic (depleted) lead province
II	Sedimentary (radiogenic) lead province
III	Oceanic/Mantle (radiogenic) lead province
EZ	Eastern Zone, $\delta^{18}O$ < 10 cratonal source
CZ-S	Central Zone Sedimentary, $\delta^{18}O$ > 10 miogeoclinal source
CZ-V	Central Zone Volcanic, $\delta^{18}O$ > 9 eugeoclinal source
WZ	Western Zone, $\delta^{18}O$ < 8.5 source

Solomon and Taylor (1989)

Figure 5.2. Schematic map of the northeastern Great Basin (shaded area from Fig. 5.1) showing sample locations. Jurassic samples are represented by triangles, late Cretaceous samples by circles, Cenozoic samples by squares; sample numbers are keyed to Table 5.1. Sample markers are shaded according to $^{18}O/^{16}O$; for clarity multiple samples from composite plutons are staggered, and the numerous Cenozoic samples with $\delta^{18}O < +8.5$ are shown by much smaller black squares. The CAB boundary, the CZ-V, CZ-S, and EZ zones from SOLOMON and TAYLOR (1989), the Sevier Thrust Belt (STB), and the approximate easternmost position of the Roberts Mountain Thrust (RMT) are shown as in Fig. 5.1.

Fig. 5.2.

$\delta^{18}O$
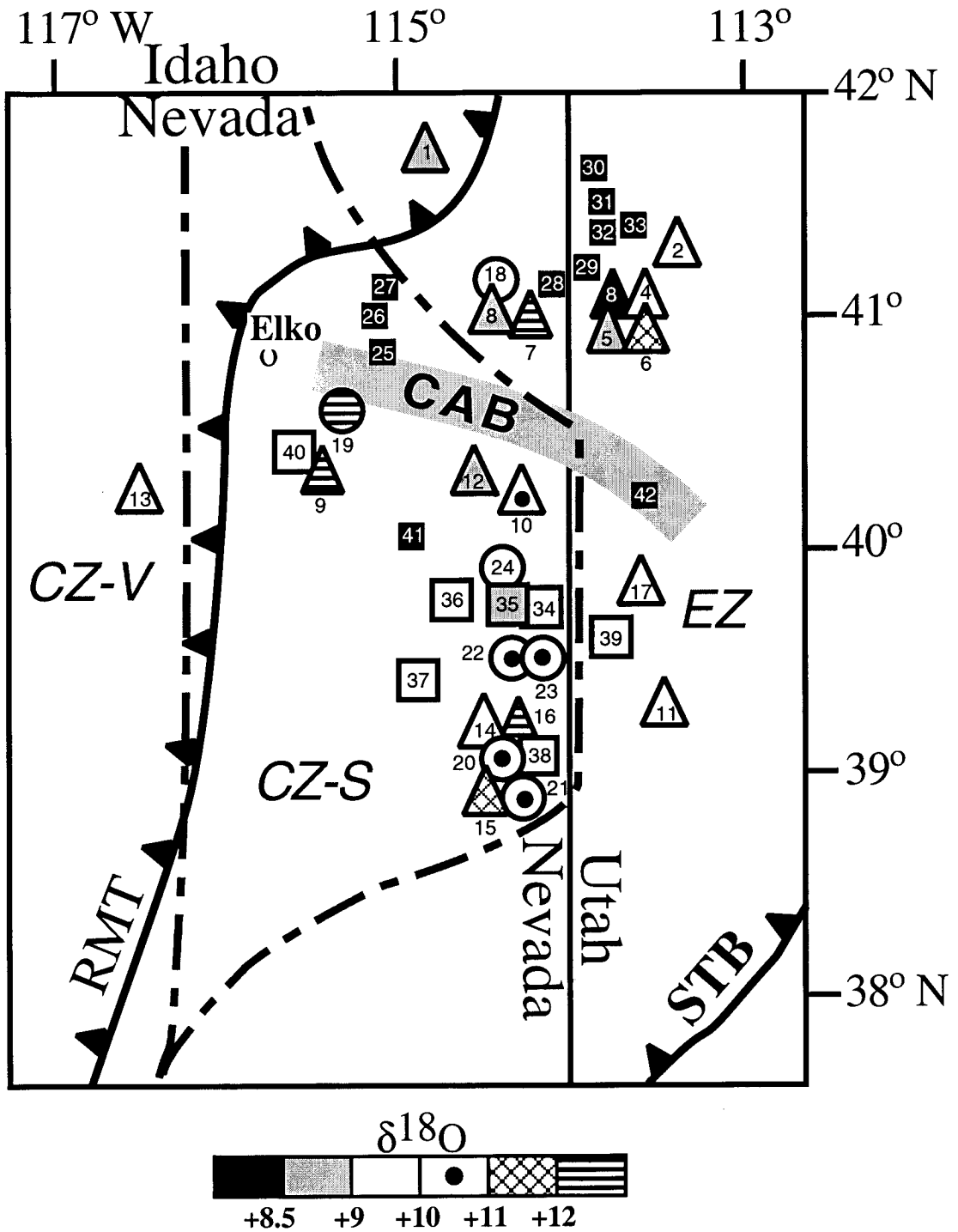
Figure 5.3 Whole-rock $\delta^{18}O$ values of Mesozoic and Cenozoic granitoids from the northeastern Great Basin, including samples measured in this study and by SOLOMON and TAYLOR (1989), LEE and CHRISTIANSEN (1983), LEE et al. (1983), and LEE et al. (1982), grouped into Jurassic, Late Cretaceous, and Cenozoic suites. Vertical separations within each age group are for clarity, and do not indicate relative ages. Filled symbols are from intrusions north of the CAB, whereas empty symbols are from the south; the gray triangle represents the Cottonwood Canyon pluton, which intrudes eugeoclinal country rocks, and the ruled symbol represents the Cenozoic Gold Hill pluton, whose location relative to the CAB is ambiguous. Typical ranges for the mantle (+5.5 to +6.5) and siliciclastic sediments (> +14) are indicated by two vertical shaded bands. For the Jurassic suite, the thin gray line at about +9.0 separates relatively low-^{18}O, shallowly intruded granitoids (including Silver Zone Pass pluton) from the high-$\delta^{18}O$ Jurassic intrusions that were emplaced more deeply in the miogeocline.

Fig. 5.3.

177

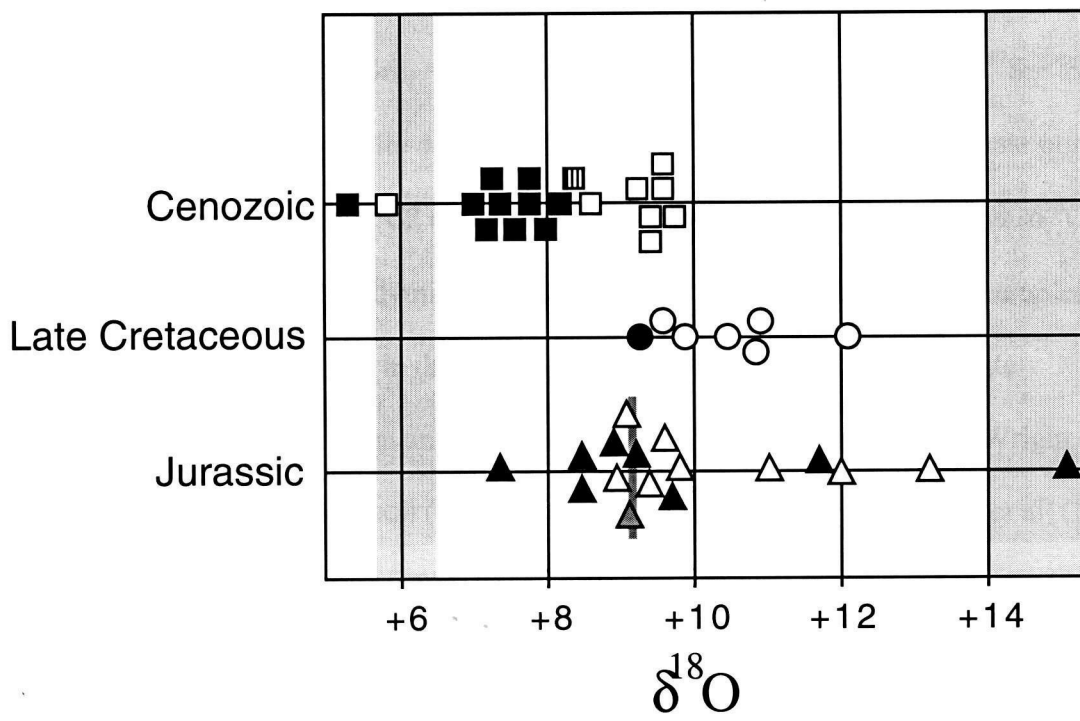Figure 5.4. a) $^{87}Sr/^{86}Sr_i$ vs. $\delta^{18}O$ for northeastern Great Basin granitoids. For clarity the

Jurassic envelope excludes sample UT-GH-2. EZ, CZ-V, and CZ-S envelopes of

SOLOMON and TAYLOR (1989) are shown in gray. The dashed gray and solid black curved

lines are contours of ppm strontium abundance for Cenozoic and Jurassic samples,

respectively. Late Cretaceous samples have strontium abundances labelled point by point.

Thick gray arrow shows the model evolution of a mantle melt (C1) assimilating average

Ruby Mtns. pelitic crust (C2) as calculated with an AFC model with $\delta^{18}O_{C1}$ = +6.5,

$C_{C1}(Sr)$ = 1000 ppm, $^{87}Sr/^{86}Sr_{C1}$ = 0.705; $\delta^{18}O_{C2}$ = +17, $C_{C2}(Sr)$ = 180 ppm, $^{87}Sr/^{86}Sr_{C2}$ =

0.726; D_{Sr} = 1.5, r = 0.3 (Pelite data from Kistler et al., 1981). The approximate positions

of these hypothetical C1 and C2 components are shown on Fig. 5.7. b) ϵNd vs. $\delta^{18}O$ for

the same samples. Ppm Neodymium abundances are contoured for Jurassic samples in

black, for Cenozoic samples in dashed gray, and are labelled next to each Late

Cretaceous sample. Strontium and Neodymium abundance data are from J. Wright (pers.

commun.), MILLER and HOISCH (1995), FARMER and DEPAOLO (1983), LEE et al. (1982),

and LEE and CHRISTIANSEN (1983). Sample PR-79 plots well to the right of the diagram,

as indicated by the small labeled arrow. Thick gray arrows show evolution of mantle melt

(C1) assimilating average Precambrian-early Paleozoic miogeocline pelitic crust (C2) as

above, with $\epsilon Nd(C1)$ = –3, $C_{C1}(Nd)$ = 100 ppm, $\epsilon Nd(C2)$ = –13.9 (lower arrow) or –10.2

(upper arrow), $C_{C2}(Nd)$ = 42 ppm, and D_{Nd} = 1.5. Pelite Nd data from FARMER and BALL,

(1997).

Fig. 5.4.
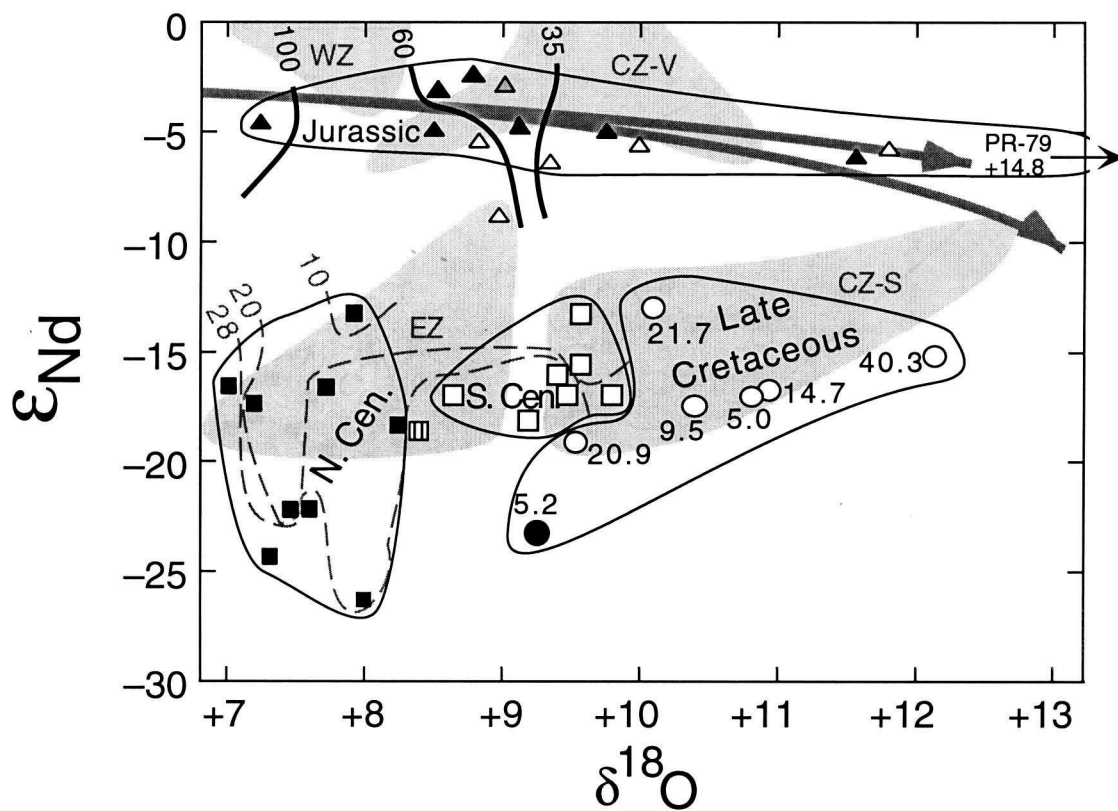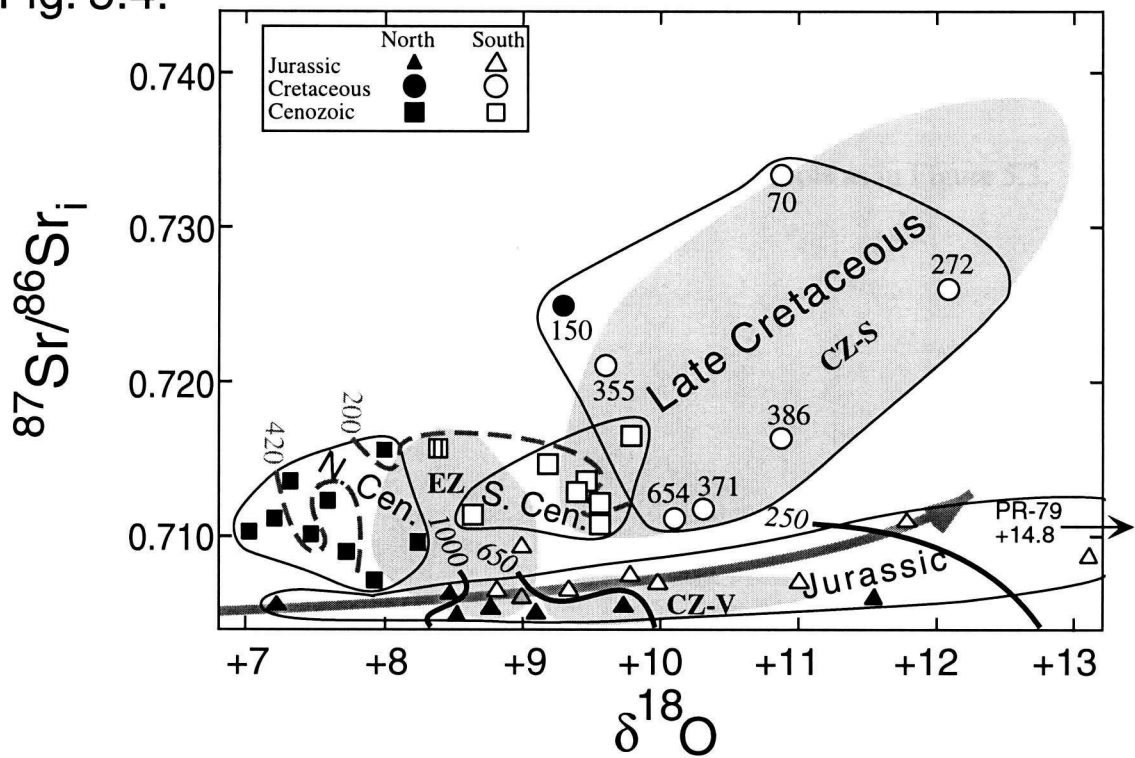
Figure 5.5. (a) Plot of $\delta^{18}O$ vs. $^{206}Pb/^{204}Pb$ for granitoids of the northeastern Great Basin, using lead isotope data of WRIGHT and WOODEN (1991), and MILLER and HOISCH (1995).

b) Plot of $\delta^{18}O$ versus $^{208}Pb/^{204}Pb$ for the same samples. Symbols as in Figure 5.3.
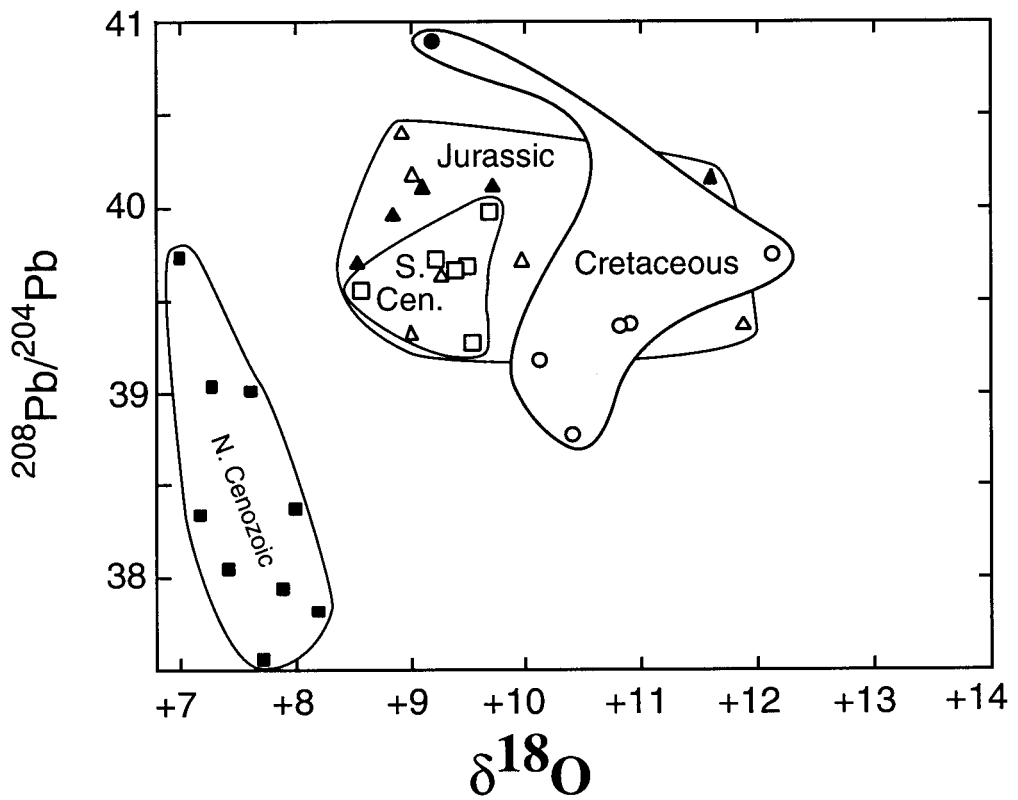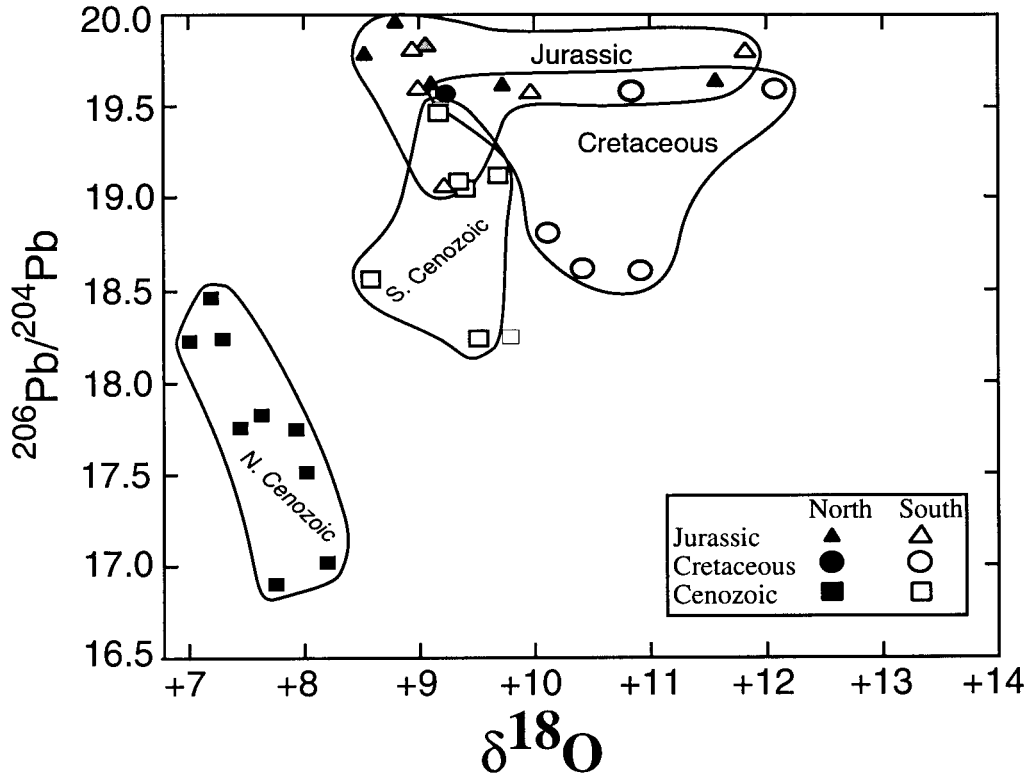
Fig. 5.5.

Figure 5.6 Strontium mixing plot (1/Sr vs. ^{87}Sr/^{86}Sr$_i$). Miogeocline Pelite field (gray area) is based on measurements of micaceous and quartzofeldspathic schists from the Ruby Mountains (KISTLER et al., 1981) projected back to 100 Ma. Data envelopes are shown for Jurassic and Late Cretaceous fields only. Thick gray arrow indicates evolution of mantle melt (C1) assimilating average Ruby Mtns. pelitic crust (composition indicated by "X"), AFC parameters are the same as in Fig. 5.4.
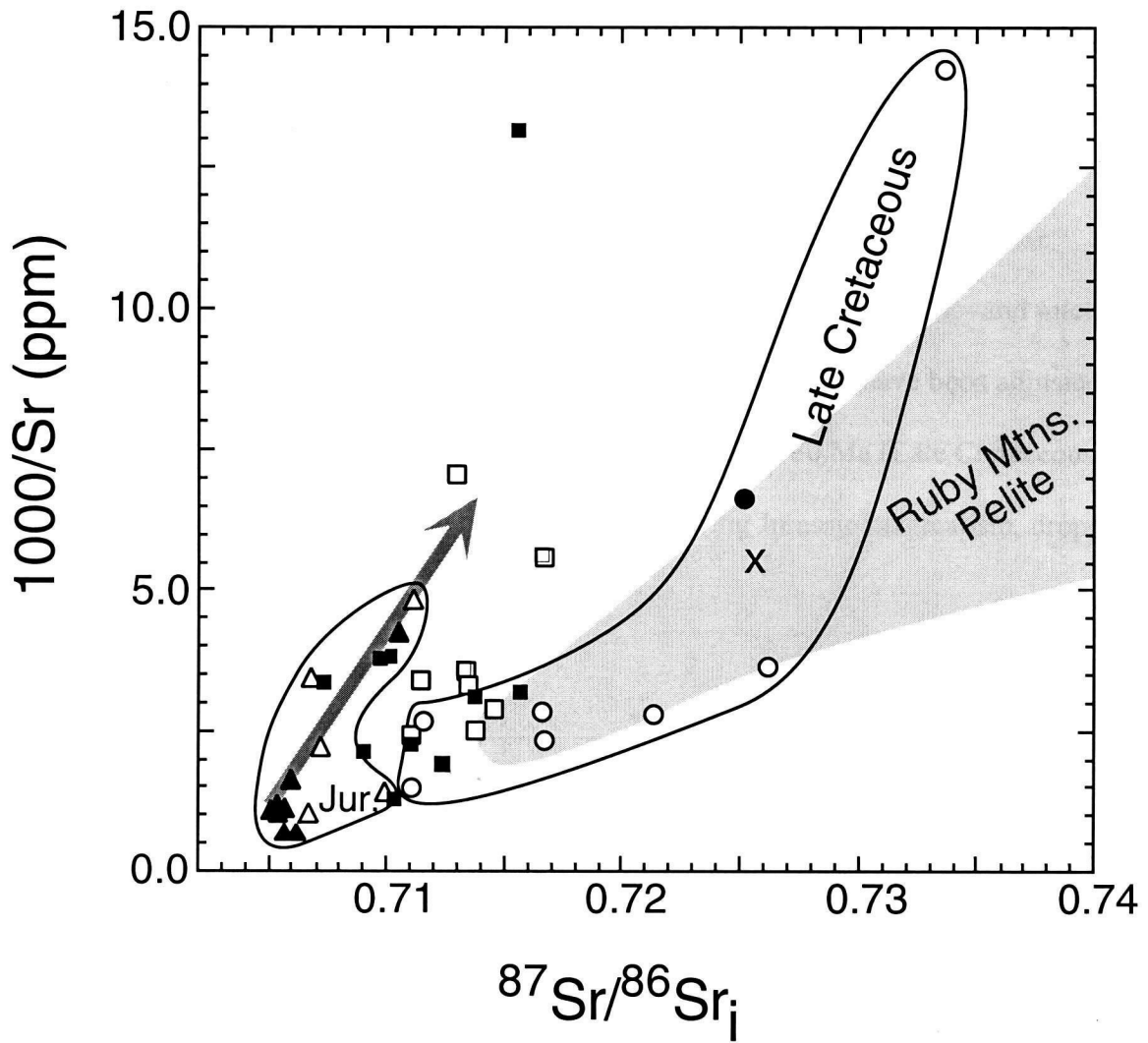
Fig. 5.6.

Figure 5.7 Simplified plots of $^{87}Sr/^{86}Sr$ vs. $\delta^{18}O$ and ϵNd vs. $\delta^{18}O$ (compare with Fig. 5.4), showing a range of model mixing curves (gray shaded regions) and proposed end members during magmatism in the Late Jurassic (left side) and Late Cretaceous (right side). The lower-$\delta^{18}O$ Jurassic end member is represented by the small black square labeld C1 ($\delta^{18}O = +6.5$, $^{87}Sr/^{86}Sr = 0.705$, 1500 ppm Sr, $\epsilon Nd = -3$, 120 ppm Nd), while the late Cretaceous lower-$\delta^{18}O$ end member is assumed to include material similar to that which formed Cenozoic granitoids in this study. The high-^{18}O (C2) end member is assumed to be pelitic miogeoclinal sedimentary rock, and is modeled using the Sr isotopic and abundance data of KISTLER et al. (1981) on quartzofeldspathic- and mica-shists from the Ruby Mountains. Pelite ^{87}Sr and ^{143}Nd abundances have been adjusted to account for radiogenic ingrowth since 150 Ma (Jurassic) and 80 Ma (Late Cretaceous). Pelite $\delta^{18}O$ is assumed to be in the range +15 - +16 during Jurassic magmatism, dropping to +12 to +13 by the Late Cretaceous.

Fig. 5.7
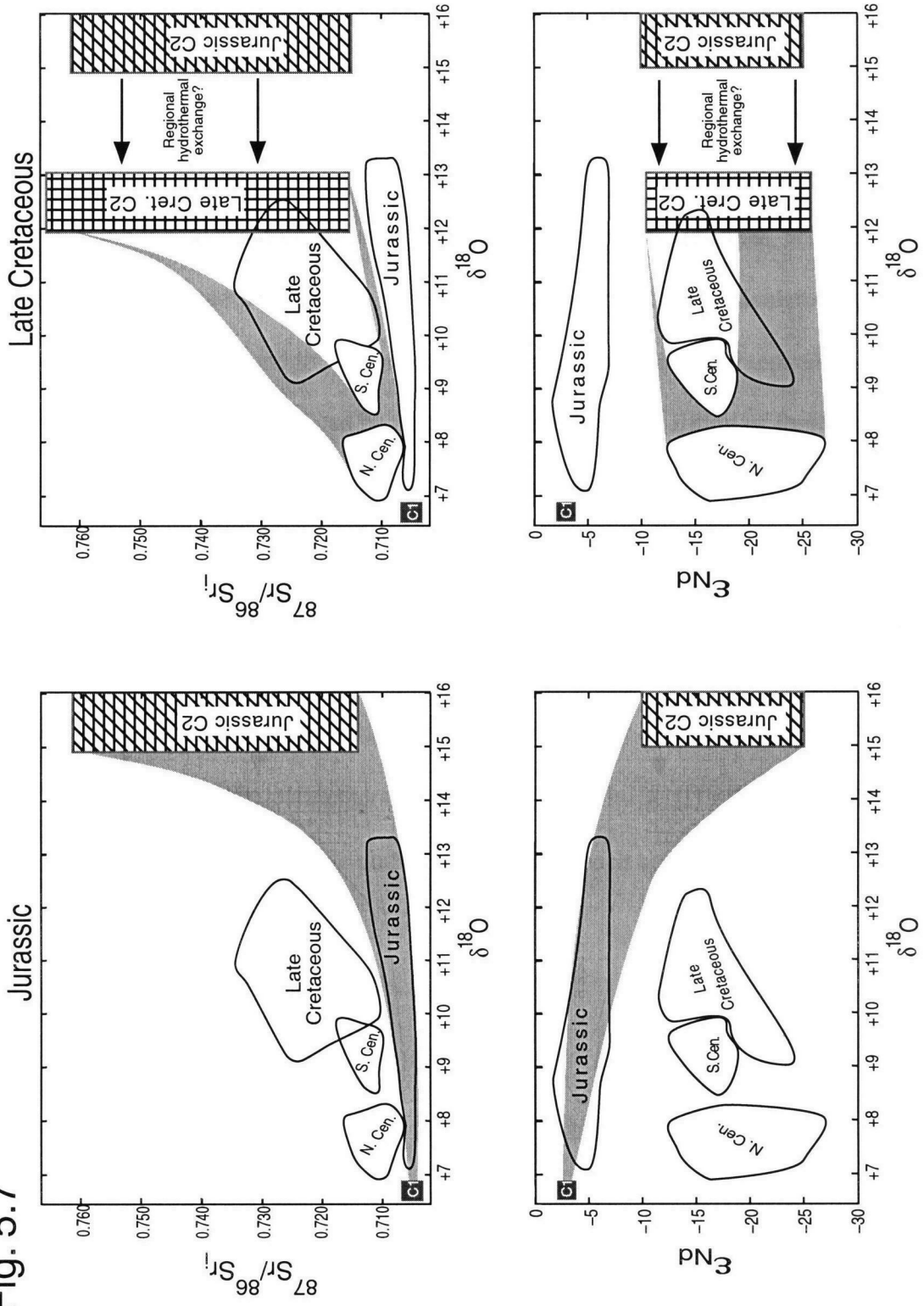
Appendix. Matlab Codes

Theoretical calculations of equilibrium isotope fractionations were carried out using Matlab scripts. Two representative scripts are included here. The first script (MUBFF_XY4.m) is used to calculate vibrational frequencies for tetrahedral (XY4) molecule and complexes using the Modified Urey Bradley Force Field (Nakamoto, 1997). Input includes atomic masses, measured vibrational frequencies, and force constants. Calculated frequencies, sum-of-squares errors between calculated and measured frequencies, and the ratios of vibrational frequencies in isotopically substituted species are output. The code can be modified to automate the fitting of force-field parameters. A simple way to do this is to create nested loops that vary each of the three parameters, calculating misfits for each set. The second script calculates reduced partition function ratios for isotopic exchange. Both scripts are presented with input parameters appropriate for the $[CrO_4]^{2-}$ ion, very similar to those used in the preceding chapter. The only significant difference is the slightly higher frequency of the ν_4 vibration (378 cm^{-1} vs. 368 cm^{-1}). Using the parameters given below, $1000 \cdot \ln(\beta_{53-52}) = 13.6‰$ at 273.15 K and 11.7‰ at 298.15 K. Sample output is given after each script.

```
%% MUBFF_XY4.m
%%    Matlab script to calculate vibrational frequencies
%%    and frequency ratios for tetrahedral (XY4)
%%    molecules using the Modified Urey Bradley Force
%%    Field.
%%
%%    General FF parameters are tabulated in App. VII of
%%    Nakamoto (1997) Infrared and raman spectra of
%%      inorganic and coordination compounds, Pt. A.


%% Top section sets variables specific to molecule,
%%  here [CrO4](2-) is being modeled.
     % Masses (all in a.m.u.)
mCr = 51.996;     % atomic mass of Cr
mO =  15.9994;    % atomic mass of O
m52 = 51.940511;  % atomic mass of Cr-52
m53 = 52.940652;  % atomic mass of Cr-53
mX=1/mCr; mY=1/mO; mXlight=1/m52; mXheavy=1/m53;


     % Measured frequencies for the isotopically normal
     %  species (in 1/cm) (From Nakamoto, pg. 199)
A1m = 846;        % A1 mode
Em = 349;         % E  mode
F2m = [378; 890]; % F2 modes (lowest 1st)


     % Spring constants (all in millidyne/angstrom)
K = 4.940;       % Cr-O stretch
H = 0.226;        % O-Cr-O bend
F = 0.448;        % O-O repulsion



%% Remaining code is general for XY4 molecules in
%% which the X-atom is substituted.

n=1302.83;          % conversion factor: sqrt(mdyn/ang/amu)
                    %          --> 1/cm


     % Calculate frequencies of normal species
A1 = n*sqrt(mY*(K+4*F))     % Totally symmetric stretch
E = n*sqrt(3*mY*(H+0.4*F))  % Bend
GF2 = [mY+4/3*mX -8/3*mX; -8/3*mX 16/3*mX+2*mY];
FF2 = [K+1.2*F 0.6*F; 0.6*F H+0.4*F];
F2 = n*sqrt(sort(eig(GF2*FF2)))  % IR-active modes

     % Calculate sum-of-squares misfit w/measurement
leastsq =  (A1-A1m)^2 + (E-Em)^2 + sum((F2-F2m).^2)

     % Calculate ratio of frequencies in heavy,
     %  light bearing species
mX = mXlight;
GF2 = [mY+4/3*mX -8/3*mX; -8/3*mX 16/3*mX+2*mY];
F2light = n*sqrt(sort(eig(GF2*FF2)));
mX = mXheavy;
GF2 = [mY+4/3*mX -8/3*mX; -8/3*mX 16/3*mX+2*mY];
F2heavy = n*sqrt(sort(eig(GF2*FF2)));
ratio = [F2'; (F2heavy./F2light)']
```

Output from: MUBFF_XY4.m

oldpet% matlab -nojvm

< M A T L A B >
Copyright 1984-2001 The MathWorks, Inc.
Version 6.1.0.450 Release 12.1
May 18 2001

  To get started, type one of these: helpwin, helpdesk, or demo.
  For product information, visit www.mathworks.com.

>> MUBFF_XY4

A1 =

  845.0997

E =

  359.1131

F2 =

  368.6659
  890.6955

leastsq =

  190.6950

ratio =

  368.6659   890.6955
    0.9975   0.9973

>>

```
%% ThousandLogBeta.m
%%    Matlab script to calculate reduced partition
%%    function ratios for isotope exchange reactions
%%    from vibrational spectra.
%%
%%    The form of the Urey Equation used here is
%%    from Criss (1991) Temperature dependence of
%%    isotopic fractionation factors. In:
%%    Taylor et al. (eds.) Stable isotope
%%    geochemistry, a tribute to Samuel Epstein
%%    Geochem. Soc. Spec. Pub. 3, pp. 11-16

%% Top section sets variables specific to the
%%    substance of interest (here [CrO4]-2),
%%    exchanging Cr-53 for Cr-52.

    % Frequencies (in 1/cm) - it is necessary
    % to include degenerate modes.

wlight = [378 378 378 890 890 890]; % w/Cr-52

    % freqs w/ Cr_53 use ratios from MUBFF_XY4.m
wheavy = wlight.*[0.99746 0.99746 0.99746 ...
                 0.99731 0.99731 0.99731];

    % Number of atoms substituted
nsub = 1;            % 1 Cr-atom is substituted

    % Temperatures (K) for calculations
T=[273.15 298.15];   % 0C and 25C

%% Remaining code is general for any harmonic
%% molecule.

h = 6.6260755 * 10^-34;  % Planck const.   J*sec
k = 1.380658  * 10^-23;  % Boltzmann const. J/K
c = 2.99792458* 10^10;   % Speed of light cm/sec

% Calculate beta-factor
% w/Criss equations 3b, 4a, and 4b.

U1= wlight*c*h/k;
U2= wheavy*c*h/k;

t=1./T;
beta = ones(1,size(T,2));

for j = 1:size(T,2)
 for i = 1:size(wlight,2)
   beta(1,j) = beta(1,j)*(U2(i)/U1(i))*exp((U1(i)-U2(i))*t(j)/2)* ...
       (1-exp(-U1(i)*t(j)))/(1-exp(-U2(i)*t(j)));
 end
end

% Output reduced partition funtion ratios
thousandlnbeta = 1000/nsub*log(beta);
[T' thousandlnbeta']
```

189

Output from: ThousandLogBeta.m

>> ThousandLogBeta

ans =

```
  273.1500    13.5512
  298.1500    11.7328
```

>>